

Interannual Variation of Cold Frontal Activities in the Eurasian Continent

A Dissertation Submitted to
the Graduate School of Life and Environmental Sciences,
the University of Tsukuba
in Partial Fulfillment of the Requirements
for the Degree of Doctor of Philosophy in Science

Masamitsu HAYASAKI

Abstract

Interannual variation of cold frontal activities (CFA) are examined over the Eurasian continent using the European Centre for Medium-Range Weather Forecasts reanalysis (ERA-40) data for 45 years from September 1957 to August 2002. The CFA is evaluated by area-integrated frequency of “cooling days” determined by a rapid decrease in daily mean surface air temperature exceeding 5 K a day.

The geographical distribution in the frequency of cooling day averaged for each season shows that the most frequent area over Eurasia is eastern Mongolia with the highest frequency of cooling days in spring. A large number of cooling days in springtime Mongolia represent recurrent passages of cold frontal systems that is formed at a leading edge of a cold air during cold surge period.

The interannual variations of CFA in eastern Mongolia show apparent reduction since the mid 1980s particularly in May. To determine the main cause(s) of the differences in the CFA, monthly composite analyses are conducted for 8 years with the highest CFA (active years) and 8 years with the lowest CFA (inactive years) for the period 1972–2002.

From the spatial distribution of the cooling day frequency between the active and inactive years, there are no apparent differences in eastern Mongolia with regard to geographical route of cold air. The total number of cooling events and mean cooling period in eastern Mongolia are approximately same between the two composites. In contrast, the cooling intensity in the inactive years is clearly less than that in the active years. It is clear that the reduction of CFA substantially depends on the decreases of cooling intensity which correspond to a horizontal temperature difference across a cold front.

The relationships between the reduction of CFA and meteorological conditions are also examined based on the composite analyses using several meteorological variables (e.g., temperature, snow cover extent, and cyclone activity). The difference fields between two composites are represented by subtracting the active years from the inactive years. The temperature fields show that significant warm differences in the middle and lower

troposphere extend southeastward from the West Siberian Plain to eastern Mongolia and to northeastern China. The areas of the warm differences are good agreement with the area not only of the largest warming trend over Eurasia in recent two decades but also of the primary pathway of cold air originated from Siberia.

Mean snow cover extent for the inactive years exhibits 16% decreases ($-0.87 \times 10^6 \text{ km}^2$) to the climatology over eastern Eurasia in mid-May. Cyclone intensity for the inactive years is evidently less than that for the active years in eastern Mongolia and northeastern China, where the traveling cold frontal systems generate lee-cyclones in the downstream of Altai–Sayan Mountains.

The results in this study suggest that the weakening of cold air intensity produces warm temperature anomalies along a route of cold air originated from West Siberian Plain to China. Consequently, an intensity of cold front is closely related to not only the local weather (day-to-day temperature variability) in eastern Mongolia but also the cyclone activities in the downstream areas.

keywords: cold front, climate change, cold air outbreak, cyclogenesis/cyclolysis, seasonal march, snow cover, dust storm

Contents

Abstract	i
List of figures	viii
List of tables	ix
1 Introduction	1
1.1 Prologue	1
1.2 Cold frontal activity in association with a climate change	2
1.3 General aspects of the activity of cyclones and fronts	3
1.4 Relationship between cold frontal activity and cold air outbreaks	6
1.5 Relationship between cold frontal activity and dust storms	7
1.6 Purpose of this study	8
2 Data and analysis method	27
2.1 Data	27
2.1.1 Surface observational data	27
2.1.2 Satellite data	27
2.1.3 Objective analysis data	28
2.1.4 Cyclone track data	29
2.1.5 Analysis period	29
2.2 Analysis method	30
2.3 Validation of cooling days	31

2.3.1	Case study: Strong cooling event in Mongolia during 6–7 April 2002	31
2.3.2	Relationship between cooling days and passages of cold fronts . . .	33
3	Climatological linkages between cold frontal activity and meteorological conditions	43
3.1	Horizontal distribution and seasonal march in frequencies of cooling days .	43
3.1.1	Seasonal mean climatology in frequencies of cooling days	43
3.1.2	Monthly mean climatology in frequencies of cooling days	45
3.2	Monthly climatologies of meteorological conditions in spring	47
3.2.1	Temperature and humidity	47
3.2.2	Upper-air circulation and cyclone activity	48
3.2.3	Snow and sea ice	50
3.3	Climatological relationships between cold frontal activity and meteorological conditions	51
4	Interannual variation of cold frontal activity in Mongolia	62
4.1	Seasonal mean analyses of cold frontal activity in Mongolia	62
4.1.1	Spatial pattern in frequencies of cooling days	63
4.1.2	Statistics of cold frontal activity	63
4.2	Monthly mean analyses of cold frontal activity in Mongolia in spring	65
4.2.1	Interannual variation of cold frontal activity	65
4.2.2	Spatial pattern in frequencies of cooling days	66
4.2.3	Statistics of cold frontal activity	67
5	Relationships between reduction of cold frontal activity and meteorological conditions	78
5.1	Differences in temperature fields	79
5.2	Differences in snow cover condition and upper-level circulation	79
5.2.1	Snow cover	79

5.2.2	Surface and upper level circulations	81
5.3	Differences in the activity of synoptic eddies	82
5.3.1	Synoptic-scale eddy activity at 500-hPa level	82
5.3.2	Cyclone activity	82
5.4	Summary of the changes of meteorological conditions in association with the reduction of cold frontal activity	83
6	Discussion	90
6.1	Robustness of spatial distributions of cooling day frequency in eastern Mon- golia	90
6.2	Considerations of physical processes in the weakening of cold frontal activity	90
6.2.1	Linkage between the reduction of cold frontal activity and the recent warming trend in Eurasia	90
6.2.2	Effect of the reduction of cold frontal activity in the downstream areas	92
6.3	Application of the definition of cooling day	93
7	Summary and conclusions	94
7.1	Assessment of cold frontal activity using “cooling day”	94
7.2	Interannual variation of cold frontal activity in Mongolia	95
7.3	Relationships between reduction of cold frontal activity and meteorological conditions	95
	Acknowledgments	97
	References	99

List of Figures

1.1	Annual anomalies of globally averaged surface temperature	10
1.2	Trends in seasonally averaged surface temperature for 1976–2000	11
1.3	Trends in diurnal temperature range	12
1.4	Schematic of observed variations of temperature indicators	13
1.5	Schematic of observed variations of hydrological indicators	14
1.6	Cyclone tracks in the Northern Hemisphere	15
1.7	Storm tracks in the Northern Hemisphere	16
1.8	Eigenvector of PC-1 for the Eurasian storm track	17
1.9	Number of cyclogenetic events in the East Asia	18
1.10	Number of cyclone counts in the East Asia	19
1.11	Topography in the East Asia	20
1.12	Example of the Mongolian cyclone	21
1.13	Trajectories of the surface anticyclones in the East Asia	22
1.14	Lag correlations between T_{sfc} and related meteorological variables during cold surge period	23
1.15	Tracks of the Siberian high	24
1.16	Spatial distribution in frequency of the dust episodes in Asia	25
1.17	Frequency of the dust episodes	25
1.18	Migration of a cold front during dust episode (14–16 April 1998)	26
2.1	Coverage of surface synoptic observations in 1966 and 1967	36

2.2	Topography over the Eurasian continent	37
2.3	Daily timeseries of meteorological variables at Erenhot, China	38
2.4	Spatial patterns of cooling area for 5–9 April 2002	39
2.5	Spatial patterns of θ_e and $ \nabla\theta_e $ at 700-hPa for 5–9 April 2002	40
2.6	Spatial patterns of clouds and dust storm events for 5–9 April 2002	41
2.7	Scatter diagram between ΔT_{2m} and $ \nabla\theta_e $	42
3.1	Spatial patterns in frequencies of cooling day	54
3.2	Annual cycle of monthly mean frequencies of cooling day in Mongolia	56
3.3	Mean timing of snow-disappearance over the Eurasia (1966–1990)	56
3.4	Monthly climatologies in frequencies of cooling day (1972–2002 spring)	57
3.5	Monthly climatologies of θ_e and $ \nabla\theta_e $ (1972–2002 spring)	58
3.6	Monthly climatologies of geopotential height and synoptic eddy activities at 500-hPa level (1972–2002 spring)	59
3.7	Monthly climatologies of cyclone activity (1972–2002 spring)	60
3.8	Monthly climatologies of snow cover and sea ice concentration in spring	61
4.1	Interannual variation in frequencies of cooling day over Mongolia	72
4.2	Spatial composites in frequencies of cooling day (MAM)	73
4.3	Interannual variation in frequencies of cooling day over Mongolia in spring months	74
4.4	Spatial composites in frequencies of cooling day in March	75
4.5	Spatial composites in frequencies of cooling day in April	76
4.6	Spatial composites in frequencies of cooling day in May	77
5.1	Composite differences of temperature fields between active and inactive years in May	84
5.2	Composite of NOAA snow cover in May	85
5.3	Composite timeseries of snow cover area in eastern Eurasia	86

5.4	Composite differences of Z500 and SLP fields between active and inactive years in May	87
5.5	Composite of Z500 RMS fields in May (active and inactive years)	88
5.6	Composite frequency of minimum SLP at cyclone center in Mongolia	89

List of Tables

2.1	List of data	35
4.1	List of years for composite analysis	69
4.2	Statistics for cooling activities over Mongolia	69
4.3	Monthly mean anomaly of CFA over Mongolia	70
4.4	List of years for monthly composite analyses	71
4.5	Statistics for CFA over Mongolia in each month	71

Chapter 1

Introduction

1.1 Prologue

A front in the atmosphere is defined by a boundary of two air masses which have different characteristics in temperature and humidity conditions. These differences provide a day-to-day change in temperature as a migration of a frontal system in mid- and high-latitudes. Precipitation is also provided by a cloud band along with a front. In general, an intensity of a front is evaluated by an absolute value of a horizontal gradient in temperature and humidity value across a front. Therefore, frontal activities (e.g., pathway, frequency, and intensity of frontal systems) have great impacts on a day-to-day weather change and climatic conditions in mid- and high-latitudes.

Before addressing the purposes of this study, it is first required to know fundamental knowledge of a frontal system. In this chapter we will describe the well-known characteristics of front, particularly in a cold frontal system in the Northern Hemisphere. The relationships between cold frontal activities and some meteorological and environmental issues are also documented in detail based on the earlier studies. In particular, we also focus on observed changes of day-to-day temperature variability associated with a global warming trend for the recent several decades.

1.2 Cold frontal activity in association with a climate change

Climate change is one of the most important issues in atmospheric sciences. The Intergovernmental Panel on Climate Change (IPCC) plays an important role to discuss the recent climate change. The IPCC reported that globally averaged surface air temperature rapidly increased after the late 1970s (Fig. 1.1). The warming trend was, however, not homogeneous in space and time. The significant warming trend of surface air temperatures was found over continental area between mid- and high-latitudes particularly in winter and spring (Fig. 1.2). In addition, mean annual diurnal temperature range (DTR) also showed significant decreasing trend over continental areas (Fig. 1.3). As noted by Karl et al. (1993, 1995), the decrease of DTR mainly depended on the larger increase of daily minimum temperature than that of daily maximum temperature. They also reported that the decrease of DTR is dominant over continental area in winter and spring.

As mentioned above, long-term trend of seasonal mean temperature anomaly was documented well in the previous studies. In recent years, many researchers are interested in the long-term trend of high-frequency variability such as a day-to-day temperature variation and an extreme weather event (e.g., heat wave and cold wave) (Karl and Easterling 1999). Hayasaki and Tanaka (2004) examined an abrupt change of surface air temperature in the Northern Hemisphere for the period 1948–2001. The abrupt temperature change (hereafter ATC) event was identified by the daily mean temperature rise (fall) exceeding 20 K in the subsequent three-day period. There were four areas in the frequency maxima of the ATC event during cold season (November–February) in the Northern Hemisphere, i.e., western Siberia, Alaska, northwestern Canada, and southeastern Canada. Their results showed that the frequency of the ATC event decreased ranging from 15% to 25% for the positive temperature anomalies in these areas.

Over the past decade, a considerable amount of research has focused on the observed

changes with several weather events and climate conditions in association with the warming trend (Houghton et al. 2001). The observed climate change has been reported in several meteorological conditions, for example in the surface and upper level temperatures, DTR, snow cover extent, sea ice extent and concentration, precipitation, cloud amount, and so on (Figs. 1.4 and 1.5). However, the reliability of these changes shows a wide variety in each meteorological condition. For example, as shown in Fig. 1.5, there were low reliability in concern with the long-term trend of the activity of extra-tropical cyclones in the Northern Hemisphere over twentieth century.

One of the observed climate change with high reliability is the earlier snow disappearance of continental snow cover in spring (Fig. 1.4), particularly in the Eurasia. According to Groisman et al. (1994b), snow cover extent in Eurasia showed a significant decreasing trend for the period 1972–1992. Bamzai (2003) calculated a day of snowmelt using satellite-derived snow cover during 1972–2000. Their results showed that the areas of earlier snow disappearance extensively covered over the east of 90°E in 48° – 60°N . As noted by Brown (2000), the warming trend of surface air temperatures in the Northern Hemisphere was closely related to the decrease of the snow cover extent.

1.3 General aspects of the activity of cyclones and fronts

Cyclones accompanying with frontal systems are one of the most important weather events in mid- and high-latitudes. For example, as shown in Hayasaki and Tanaka (1999), strong cyclones developing in the east of Japan form a large-scale circulation pattern (e.g., formation of blocking anticyclone) and cause a drastic temperature change in Alaska. After Blackmon (1976), a considerable amount of research has focused on cyclone activities in the Northern Hemisphere.

Whittaker and Horn (1984) illustrated the climatological tracks of cyclones in the Northern Hemisphere using surface weather maps derived from several sources for the

period 1958–1977 (Fig. 1.6). The primary cyclone tracks originate from an east coast of the major continental areas where the meridional temperature gradient is large such as the south or east of Japan and the east of North America. Most of cyclones move eastward or northeastward from the source regions and terminate to the semi-permanent subpolar low such as the Aleutian and Icelandic low in the Pacific and Atlantic Oceans, respectively. These results also documented by much amount of studies based on the variance of high-frequency fluctuations using a geopotential field at the 500-hPa level (e.g., Blackmon 1976; Lau 1988; Wallace et al. 1988). In consistent with the cyclone tracks, the largest axis of height variances extends from the east coast of continents to the northern part of mid-ocean areas (Fig. 1.7). In general, the principal cyclone paths are called as “storm tracks” in earlier studies.

As mentioned above, fundamental features of the storm tracks in the Northern Hemisphere are documented well in terms of the geographical locations (e.g., Blackmon 1976; Lau 1988; Wallace et al. 1988), relationships with typical teleconnection patterns (e.g., Lau 1988; Rogers 1997), and interannual–decadal variations (e.g., Limpasuvan and Hartmann 1999; Limpasuvan and Hartmann 2000). Although these vigorous efforts focused on a storm track activity provide vast amount of knowledge, there were two problems for discussing the linkage between storm track activity and recent climate change in the Northern Hemisphere.

One problem is based on a geographical deviation concerned with the previous studies. As shown in Fig. 1.7, the major storm tracks in the Northern Hemisphere are clearly identified over the oceanic areas in the northwest of the Pacific and Atlantic oceans. Therefore, most of studies focused on the Pacific and Atlantic storm tracks. On the other hand, there were little attention on a cyclone activity over continental area, particularly in the Eurasian continent. Lau (1988) shortly documented for the interannual fluctuations of the synoptic eddy activities in Eurasian sector (0° – 150° E) using a principal component analysis (PCA) based on the band-pass filtered height variations during 1963–1981 winter

(December, January, and February). The first dominant mode in PCA for the Eurasian storm track was characterized by a monopole pattern. This pattern indicates that the interannual variation of the Eurasian storm track was associated with the enhancement or reduction in its intensity along the climatological storm track axis (Fig. 1.8). In the East Asia, Chen et al. (1991) has analyzed a seasonal-mean cyclone activity using surface weather maps during 1958–1987 (Figs. 1.9 and 1.10). It is clear that the most frequent area of cyclogenesis over continental inland area observed in spring over eastern Mongolia and northeast China where the leeward side of the Altai-Sayan Mountains and the Great Xinganling Mountains (Fig. 1.9; see also Fig. 1.11). The cyclones generally form as secondary cyclones on the trailing cold fronts of occluded lows in western Siberia (Boyle and Chen 1987) and are called as “Mongolian cyclone” (Sun et al. 2001) or “Baikal cyclones” (Chen et al. 1991). Figure 1.12 is an example of such development. As noted by Whittaker and Horn (1984), the cyclones generated in the leeward area move northeastward to the Sea of Okhotsk and merge with the track with the oceanic cyclone tracks originated around Japan (Fig. 1.10).

The other problem is caused by a seasonal deviation. Most of the previous studies were analyzed in winter (e.g., Mullen 1987; Lau 1988; Hoskins and Valdes 1990; Wallace et al. 1993). These studies were mainly focused on the activity of storm tracks associated with a low-frequency variability of large-scale atmospheric circulations in the Northern Hemisphere. In general, the low-frequency variations are frequently observed in winter, i.e., Pacific–North American (PNA) pattern and North Atlantic Oscillation (NAO) (Wallace and Gutzler 1981). Few papers discussed in terms of the cyclone activity in other seasons, most of these studies described fundamental characteristics of cyclone activities, for example, climatological tracks of traveling cyclones (Whittaker and Horn 1984; Chen et al. 1991), mean seasonal evolutions in the geographical displacement of cyclone tracks (Whittaker and Horn 1984), dominant spatial patterns of the interannual variations (Lau 1988), and so on. As noted by Nakamura (1992), the seasonal march of

the storm track activity over the Pacific shows double peaks in early winter and late winter. The mid-winter suppression can not be seen in the seasonal cycle of Atlantic storm track. Based on the baroclinic instability theory, since an intensity of the jet stream over northwestern Pacific is the largest in mid-winter, the synoptic-scale eddies should also become largest in mid-winter. Recently, Nakamura and Sampe (2002) revealed the mechanisms of the mid-winter suppression of the Pacific storm track. They showed that synoptic-scale eddies tend to be trapped into the jet core ~ 1000 -km away from a surface baroclinic zone at 40°N . The meridional displacement between the upper-level eddies and the surface baroclinic zone provides “unfavorable” condition for the baroclinic growth. Therefore, there was no sufficient information to understand a storm track activity over the continental area, particularly in the transition seasons (i.e., autumn or spring).

Compared with a research concerned with a cyclone or storm track activity, a research of frontal activity is rarely discussed. Serreze et al. (2001) studied frontal activity in the Northern Hemisphere by using the National Centers for Environmental Prediction – National Center for Atmospheric Research (NCEP–NCAR) reanalysis data. Despite the coarse horizontal resolution, they provided a comprehensive description of frontal activities both in the spatial pattern and seasonal change. Unfortunately, frontal activities in elevated areas (e.g., the Mongolian Plateau) were masked in their study, because their definition of frontal activity was determined by the horizontal temperature gradient at the 850-hPa level. Therefore, fundamental information on a cyclone/frontal activity over mountainous areas is still insufficient compared with oceanic areas.

1.4 Relationship between cold frontal activity and cold air outbreaks

During the cold surge period, Siberian cold highs migrate southeastward to the East Asia from the high-latitude continental interior (Figs. 1.13, 1.14, and 1.15). The cold air outbreaks over East Asia are typically accompanied by the appearance of an intense

cyclone-anticyclone couplet over that region (Lau and Lau 1984). During a cold surge period, well-defined cold frontal system is formed at a leading edge of cold air outbreaks. Previous studies have shown that these cold air outbreaks are accompanied by dramatic decreases in temperature, increases in pressure, and intense northerly winds (Boyle and Chen 1987; Ding 1994; Zhang et al. 1997).

Observational analysis by Zhai et al. (1999) reported that the frequency of a strong cold surge event tends to decrease in China for the recent 40-years. Also noted in the future climate prediction by Kimoto (2005) suggests that the winter monsoonal flow tends to weaken in a future using several General Circulation Model (GCM) experiments based on the climate scenario distributed by IPCC.

Unfortunately, as discussed by Zhang et al. (1997) and Compo et al. (1999), an index to define cold air outbreaks is different in each study. Most of the definitions have been made by complex combinations of several meteorological variables based on specific surface observational data. Because of the complicated procedure and the difficulty of obtaining observational data, most of these pre-defined indices of cold air outbreaks were only used in each study. Consequently, long-term trend or interannual variation in the activity of cold air outbreaks have not been discussed yet.

Another problem with these varying definitions is that it is difficult to adapt them to gridded data, such as future climate predictions based on different scenarios in CO₂ emission. As Folland et al. (1999) pointed out, the key indices should be defined by both observational and simulated data examining the long-term variations of climate extremes.

1.5 Relationship between cold frontal activity and dust storms

As shown in Figs. 1.16 and 1.17, most dust storms are observed in spring, accompanied by a passage of a cold front in northern China and Mongolia (Sun et al. 2001; Kurosaki and Mikami 2003; Shao and Wang 2003). As eastward or southeastward propagation of a

cold front, suspended dust particles behind a cold front pass through over eastern China (Fig. 1.18). In some cases, suspended particles are transported further downstream of the source regions such as the Korean Peninsula and/or Japan (see Fig. 1.17d), and for a particular case, reached to the North America crossing over the Pacific Ocean (Husar et al. 2001). The suspended particles trouble human society: it obstructs traffic by creating bad visibility, and adversely affects human health. Recently, the record-breaking heavy dust storm events occurred in late March and early April 2002 (Park and In 2003; In and Park 2003; Sugimoto et al. 2003; Chung et al. 2003).

Based on the observational studies, the frequency of dust storms in East Asia is decreasing, particularly over the last 20 years (e.g., Qian et al. 2002; Sun et al. 2003). These studies suggest that the decreasing trend in dust storm frequency is related to recent climate change. However, the observational analyses conducted in these studies were based on visibility at surface meteorological observation sites, and, as discussed by Shao and Wang (2003), such surface weather report data may contain spatial or temporal inhomogeneities arising from different judgements by the observers.

Zhang et al. (2003) examined the long-term variations of dust emissions in the East Asia using numerical experiments for 1960–2000. Their results showed that the variations of dust emission is primarily controlled by the differences of meteorological conditions. The changes of land surface conditions have a secondary effect compared with the meteorological effect.

1.6 Purpose of this study

As noted in earlier sections, although cold frontal activity relate to the various climatological and environmental issues, the fundamental information is not enough to discuss long-term variations about it.

In the present study, we propose a simple index to the passage of cold fronts. To validate the definition, geographical distributions of passage of cold fronts and seasonal

evolutions of their frequency are examined. After the validation of the index, interannual fluctuations in cold frontal activity in Mongolia are analyzed. Emphasis of the interannual variations are placed on evaluating statistics of cold frontal activity (i.e., geographical route, temporal cycle, and intensity of a cold front). The relationships between cold frontal activity and related meteorological variables are also examined.

The outline of the paper is as follows. Chapter 2 presents the dataset used in this study and the analysis procedure to identify a cold front. Based on the synoptic weather analysis, the validity of the definition is also discussed by using surface observational data and high-resolution gridded data. Climatologies in frequencies of cooling days and related meteorological fields are summarized in Chapter 3. In Chapter 4, the interannual variations of seasonally and monthly averaged cold frontal activities in springtime Mongolia are documented. In Chapter 5, relationships between cold frontal activities and related meteorological conditions are examined. In particular, the analyses focus on snow cover extent and cyclone activity over Eurasia. Based on the results obtained from Chapter 3–5, the linkage between the change of cold frontal activity and the meteorological conditions are discussed in Chapter 6. Conclusions in this study are summarized in Chapter 7.

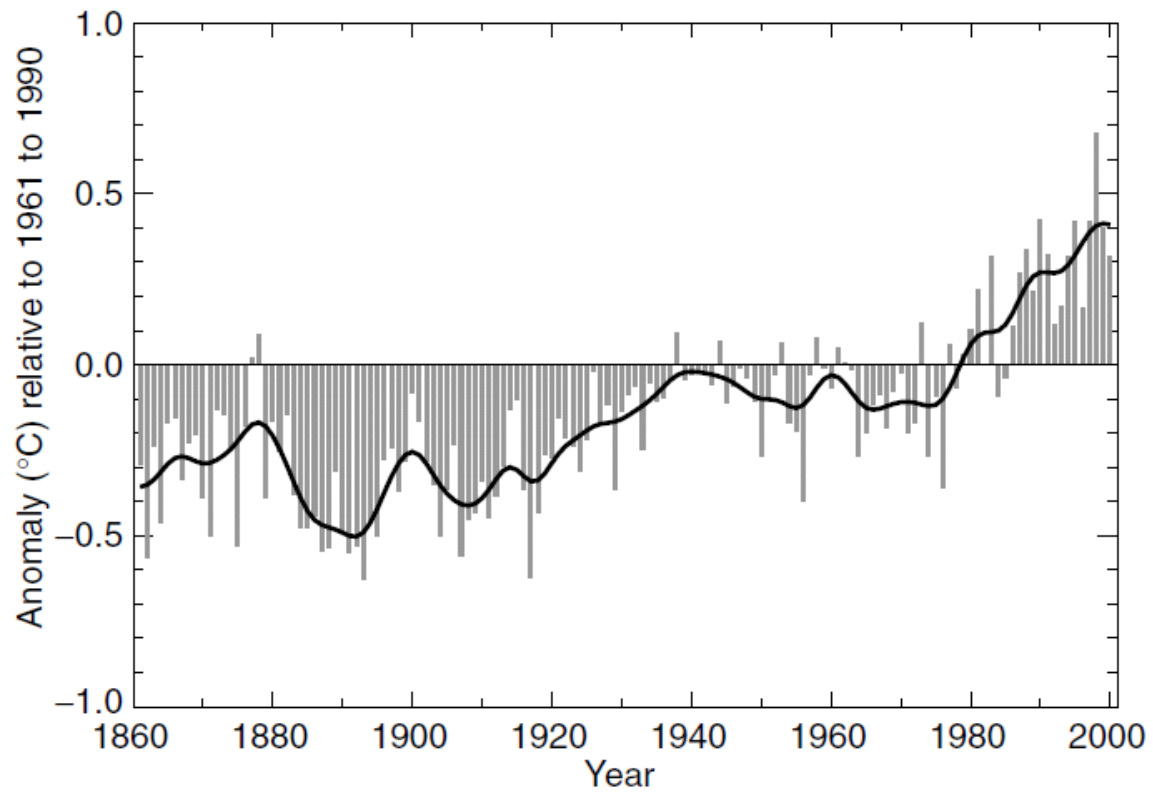


Fig. 1.1. Annual anomalies of global mean surface temperature, 1861–2000, relative to 1961–1990 values. Bars and solid curve are from the Climate Research Unit (CRU) (Jones et al. 2001). Values are the simple average of the anomalies for the two hemispheres. The smoothed curve was created using a 21-point binomial filter giving near decadal averages. (After Houghton et al. 2001, Fig. 2.1.)

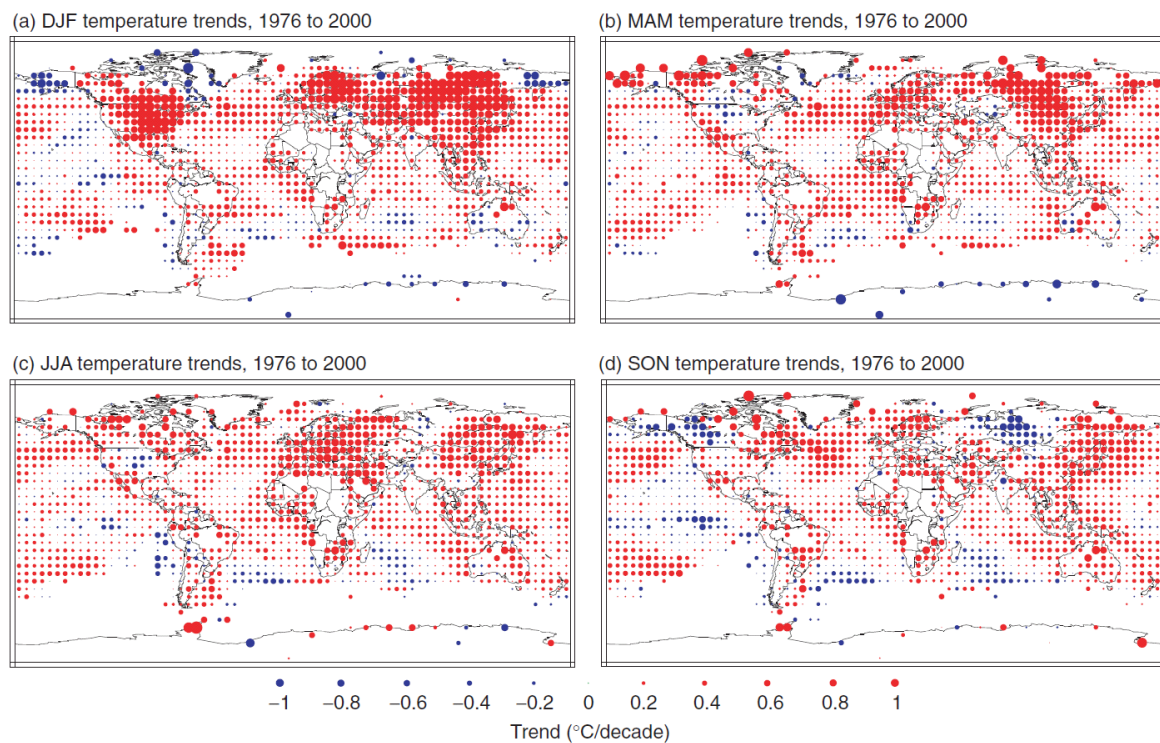


Fig. 1.2. Seasonal surface temperature trends for the period 1976 to 2000 ($^{\circ}\text{C}/\text{decade}$), calculated from combined land-surface air and sea surface temperatures. The red, blue and green circles indicate areas with positive trends, negative trends, and little or no trend, respectively. The size of each circle reflects the size of the trend that it represents. Trends were calculated from seasonally averaged gridded anomalies with the requirement that the calculation of seasonal anomalies should include all three months. Trends were calculated only for those grid boxes containing seasonal anomalies in at least 16 of the 24-years. (After Houghton et al. 2001, Fig. 2.10.)

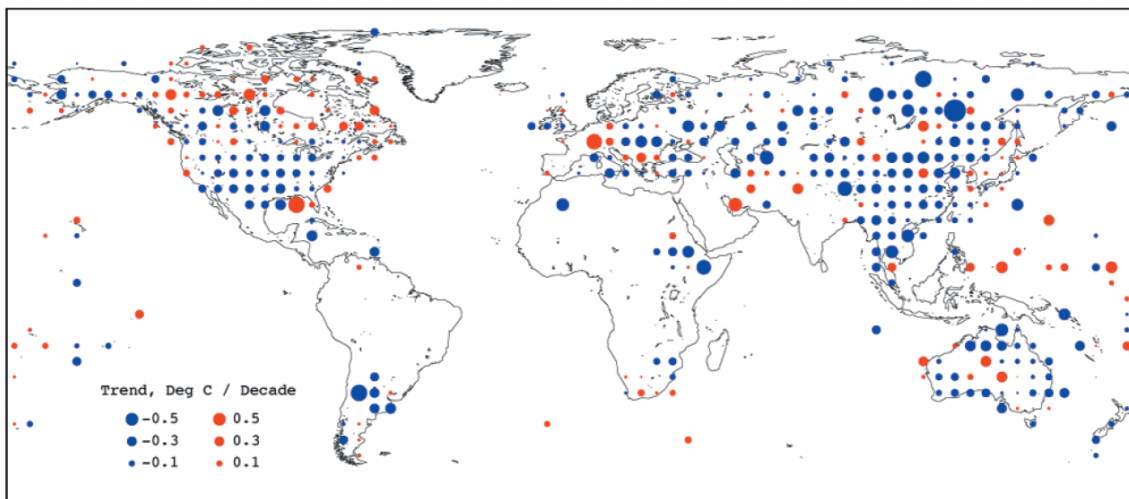
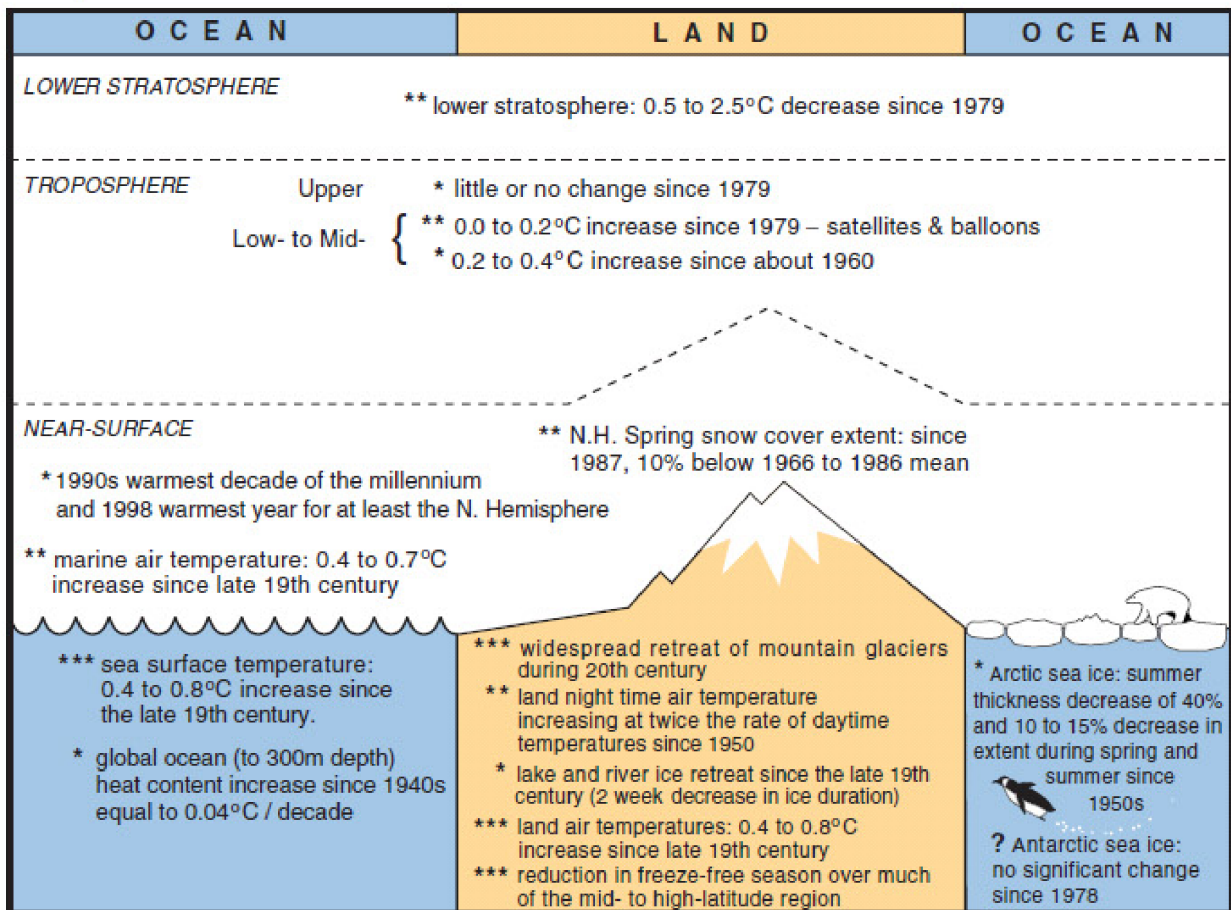


Fig. 1.3. Trends in annual diurnal temperature range (DTR, °C/decade), from 1950 to 1993, for non-urban stations only. Decreases are in blue and increases in red. (After Houghton et al. 2001, Fig. 2.2.)

Temperature Indicators

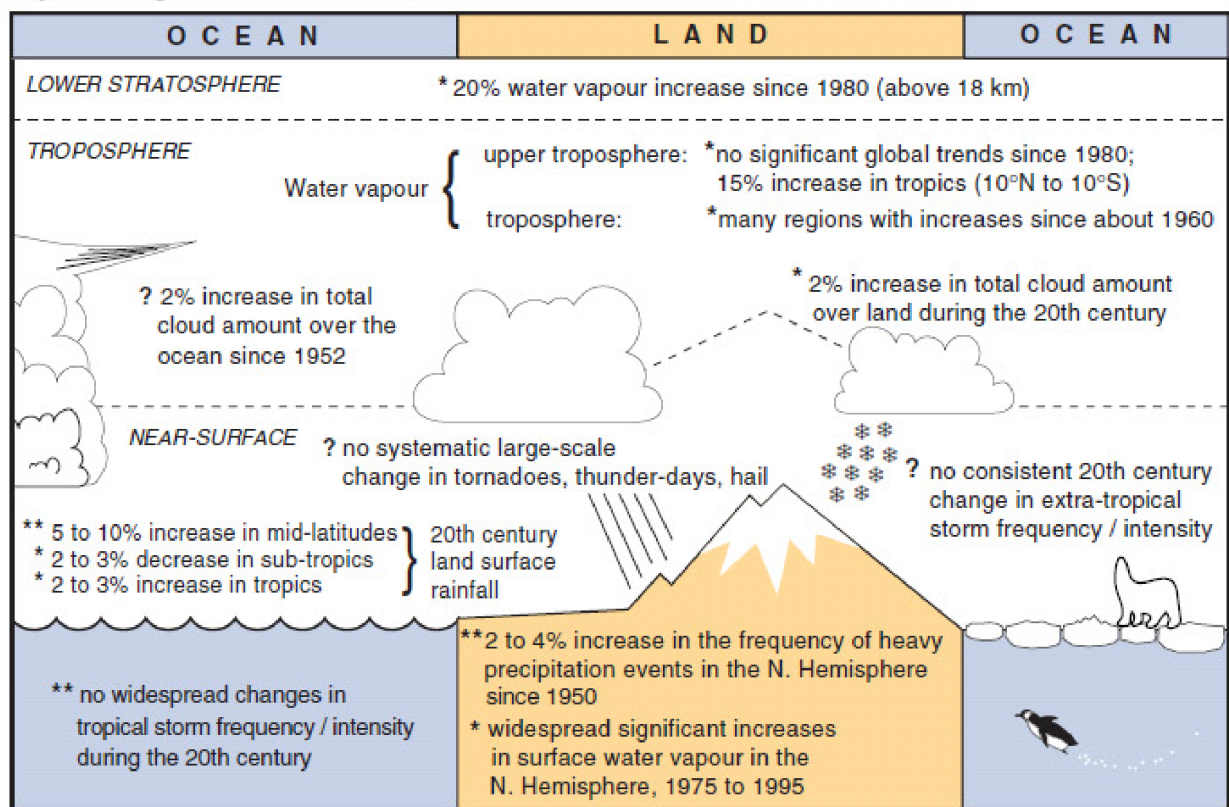


Likelihood: {

- *** Virtually certain (probability > 99%)
- ** Very likely (probability ≥ 90% but ≤ 99%)
- * Likely (probability > 66% but < 90%)
- ? Medium likelihood (probability > 33% but ≤ 66%)

Fig. 1.4. Schematic of observed variations of various temperature indicators. (After Houghton et al. 2001, Fig. 2.39a.)

Hydrological and Storm-Related Indicators



Likelihood: {

- *** Virtually certain (probability > 99%)
- ** Very likely (probability ≥ 90% but ≤ 99%)
- * Likely (probability > 66% but < 90%)
- ? Medium likelihood (probability > 33% but ≤ 66%)

Fig. 1.5. Schematic of observed variations of various hydrological and storm-related indicators. (After Houghton et al. 2001, Fig. 2.39b.)

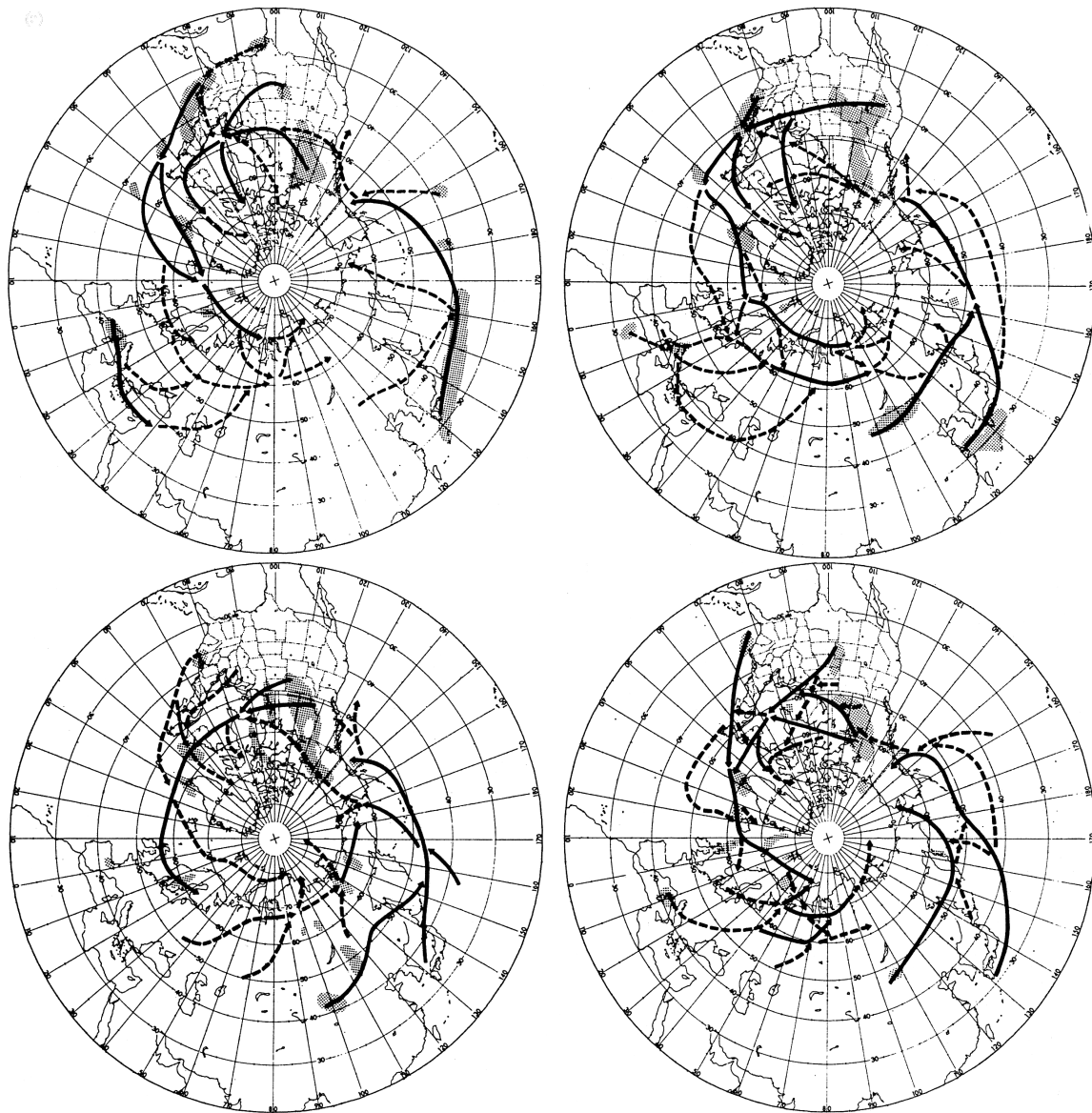


Fig. 1.6. Primary (solid) and secondary (dashed) cyclone tracks and areas of principal cyclogenesis (stippled) in January (upper left), April (upper right), July (lower left), and October (lower right). The data for these four months were compiled using surface weather maps derived from several sources for the period 1958–1977 (Adapted from Whittaker and Horn 1984).

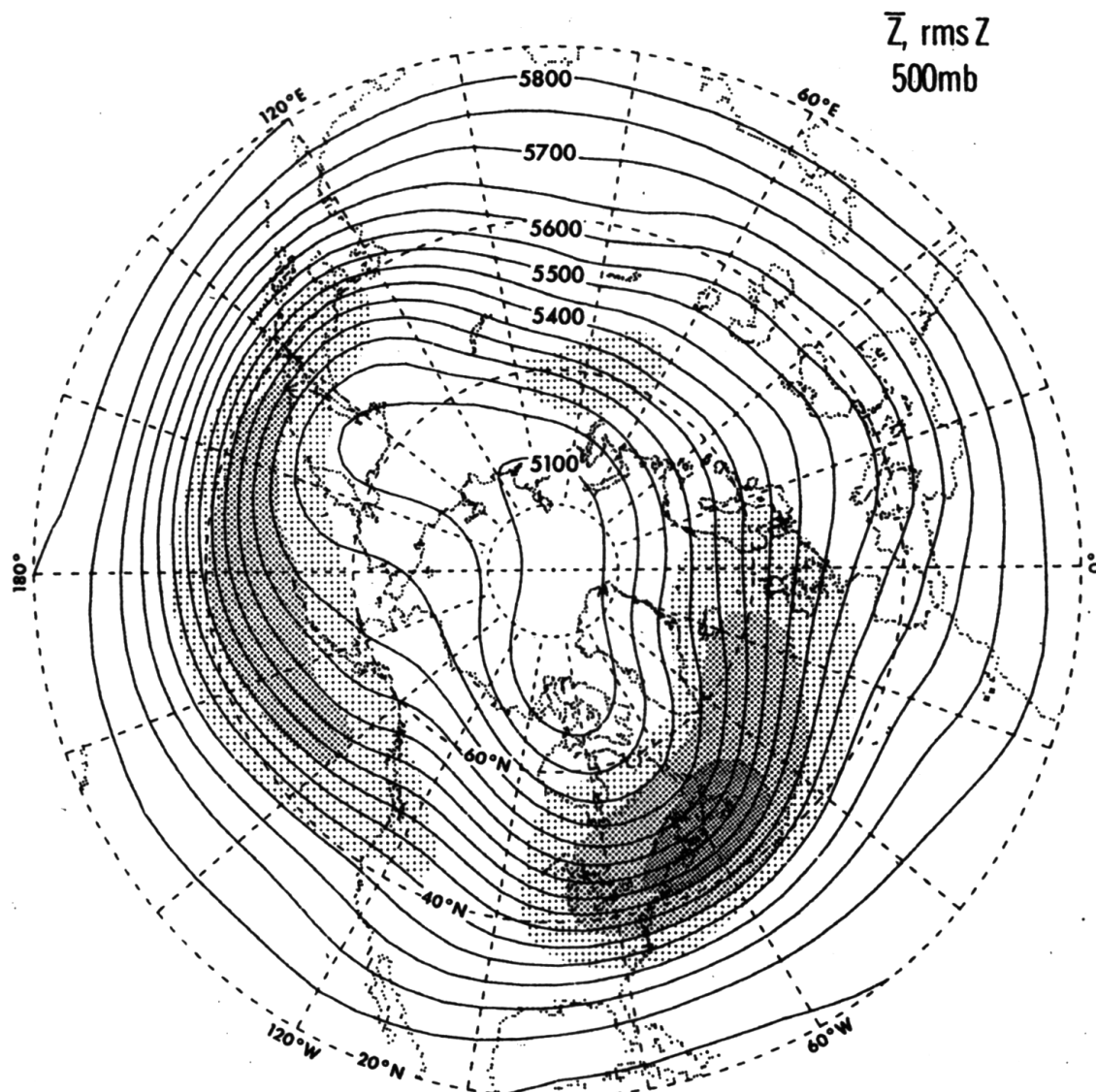


Fig. 1.7. Climatological distributions of wintertime (December, January, and February) 500-hPa height (contours) and root-mean-square (RMS) of bandpass filtered 500-hPa height (2.5–6 day period) (stippling) for the period 1963–1981. Contour interval for the time averaged height field is 50 m. The RMS values falling within the ranges of 50–60, 60–70, and > 70 m are indicated by light, medium and dense stippling, respectively. (After Lau 1988, Fig. 1.)

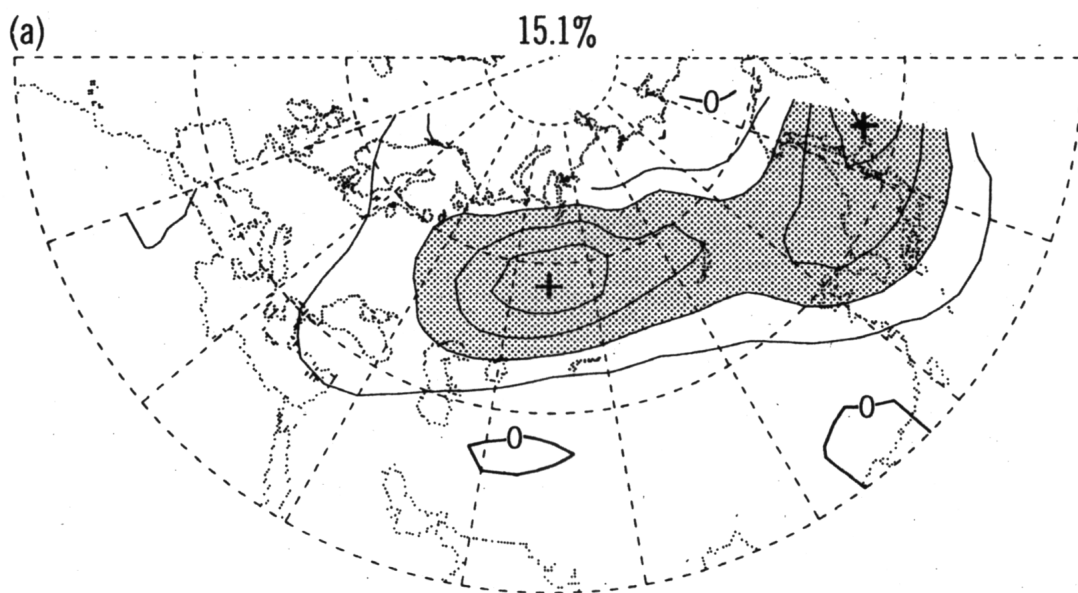


Fig. 1.8. Spatial distribution of the leading eigenvector of the RMS of the bandpass filtered 500-hPa height for the Eurasian sector (0° – 150° E). Extrema are highlighted by stippling. The percentage of variance explained is indicated at the top of the panel. Arbitrary units. (After Lau 1988, Fig. 8a.)

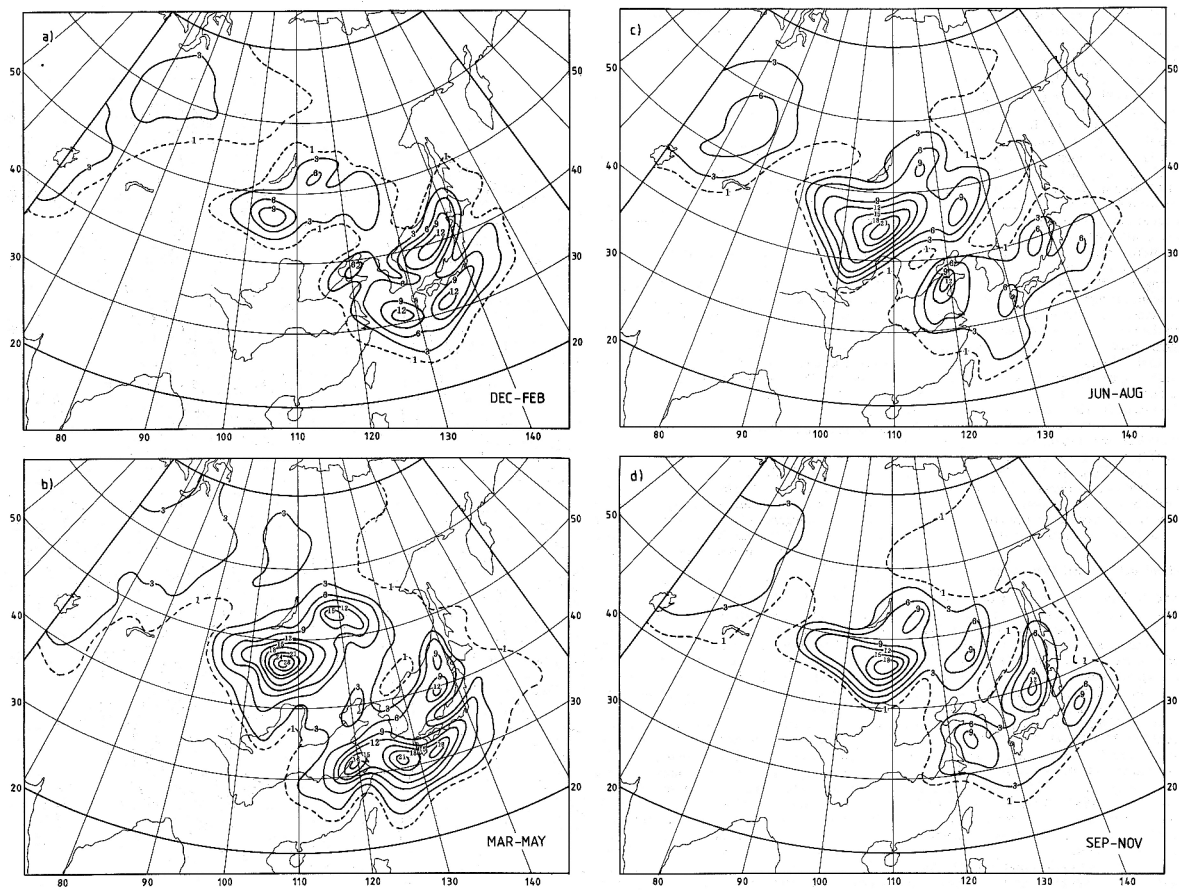


Fig. 1.9. Number of cyclogenetic events (10^{-2}) per 2.5° quadrangle per month for (a) winter, (b) spring, (c) summer, and (d) autumn for the period 1958–1987. (After Chen et al. 1991, Fig. 4.)

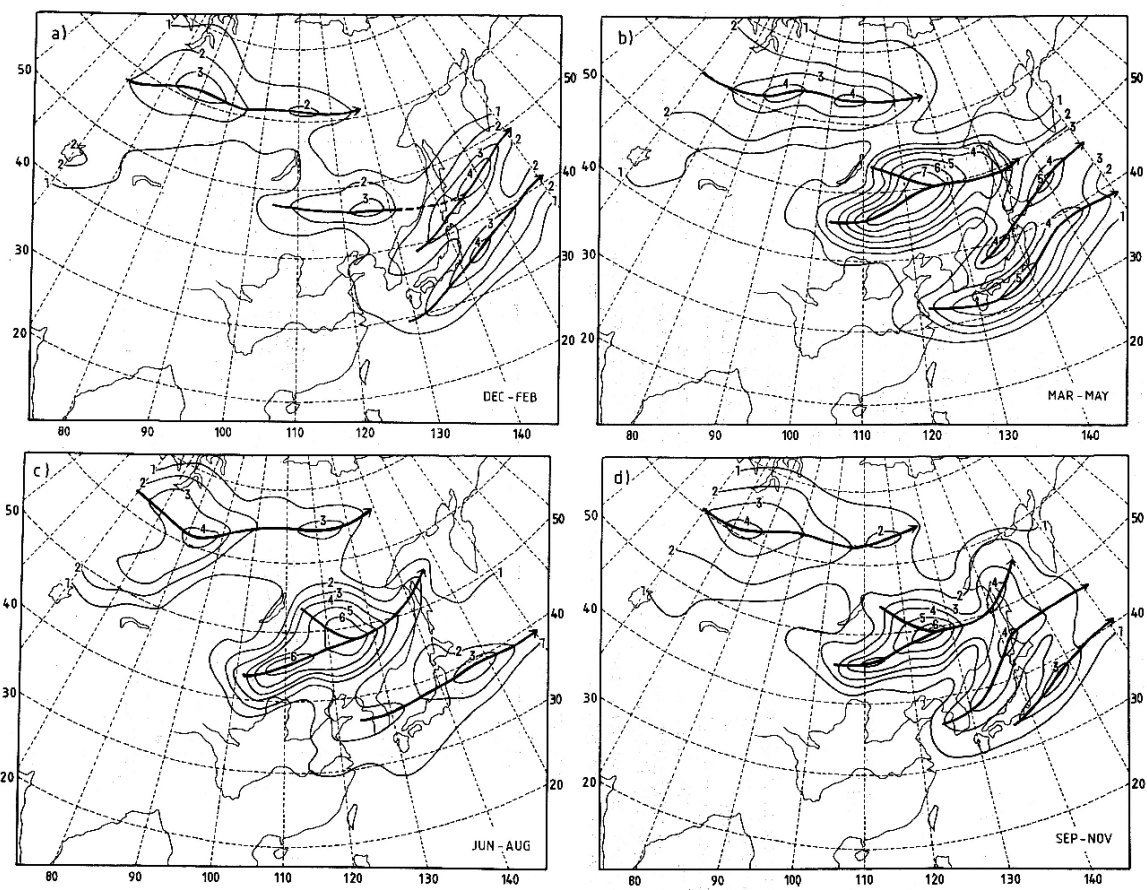


Fig. 1.10. Number of cyclone counts (10^{-2}) per 2.5° quadrangle per month for (a) winter, (b) spring, (c) summer, and (d) autumn for the period 1958–1987. (After Chen et al. 1991, Fig. 5.)

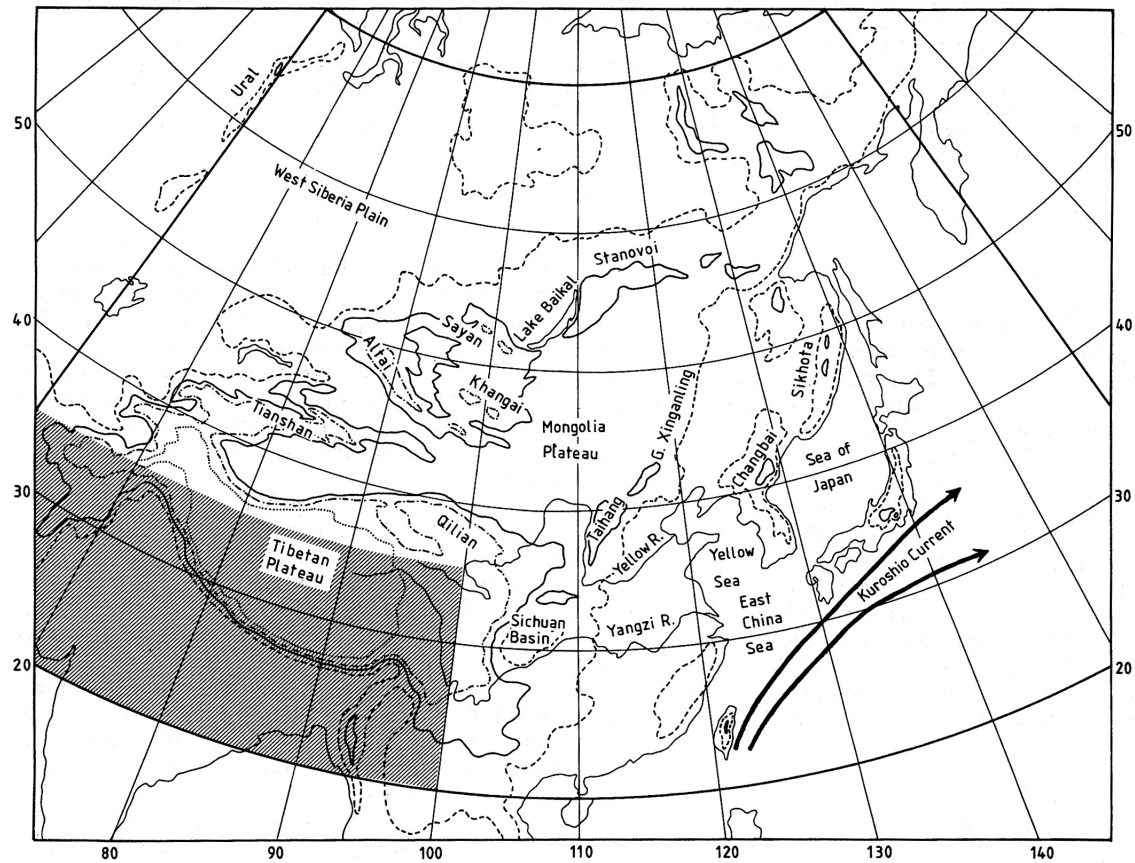


Fig. 1.11. Major geographical features over the East Asia. The terrain height contours are indicated as follows: dashed lines, 0.5 km; thin solid lines, 1.5 km; dash-dotted lines, 3 km; and dotted lines, 5 km. Thick arrows show the Kuroshio current schematically. The shaded area denotes the region where the cyclogenesis event was not counted in Chen et al. (1991). (After Chen et al. 1991, Fig. 1.)

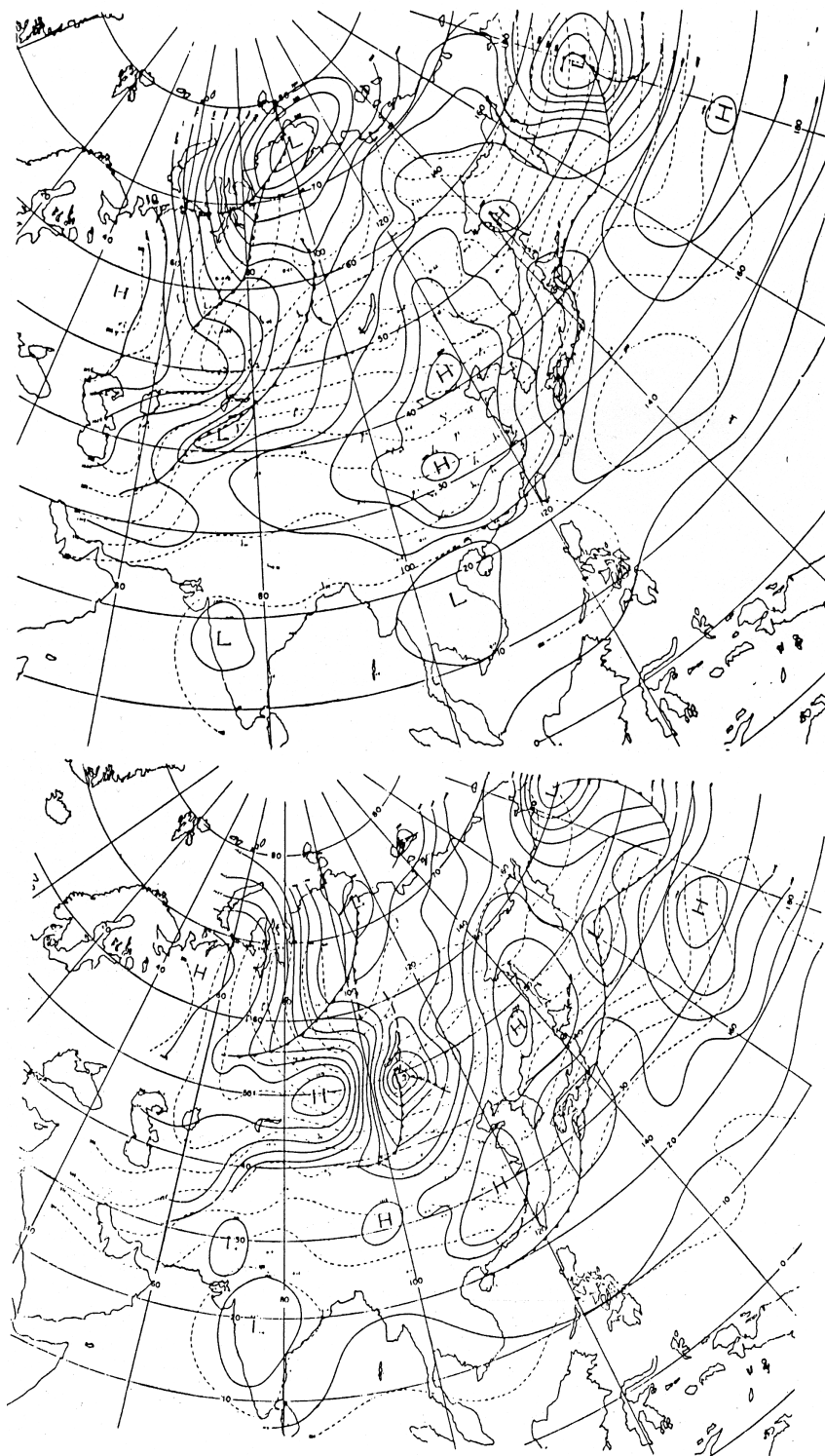


Fig. 1.12. Example of the Mongolian cyclone. Sea level pressure (solid lines) and 500-hPa heights (dashed lines) are shown. (upper) Chart for 1500 UTC 18 March 1957. An occluded front is moving into western Siberia from Europe. (lower) Chart for 1500 UTC 20 March 1957. A depression to the southeast of the Lake Baikal has formed, while the older occluded cyclone has filled rapidly. (After Boyle and Chen 1987, Fig. 5.15.)

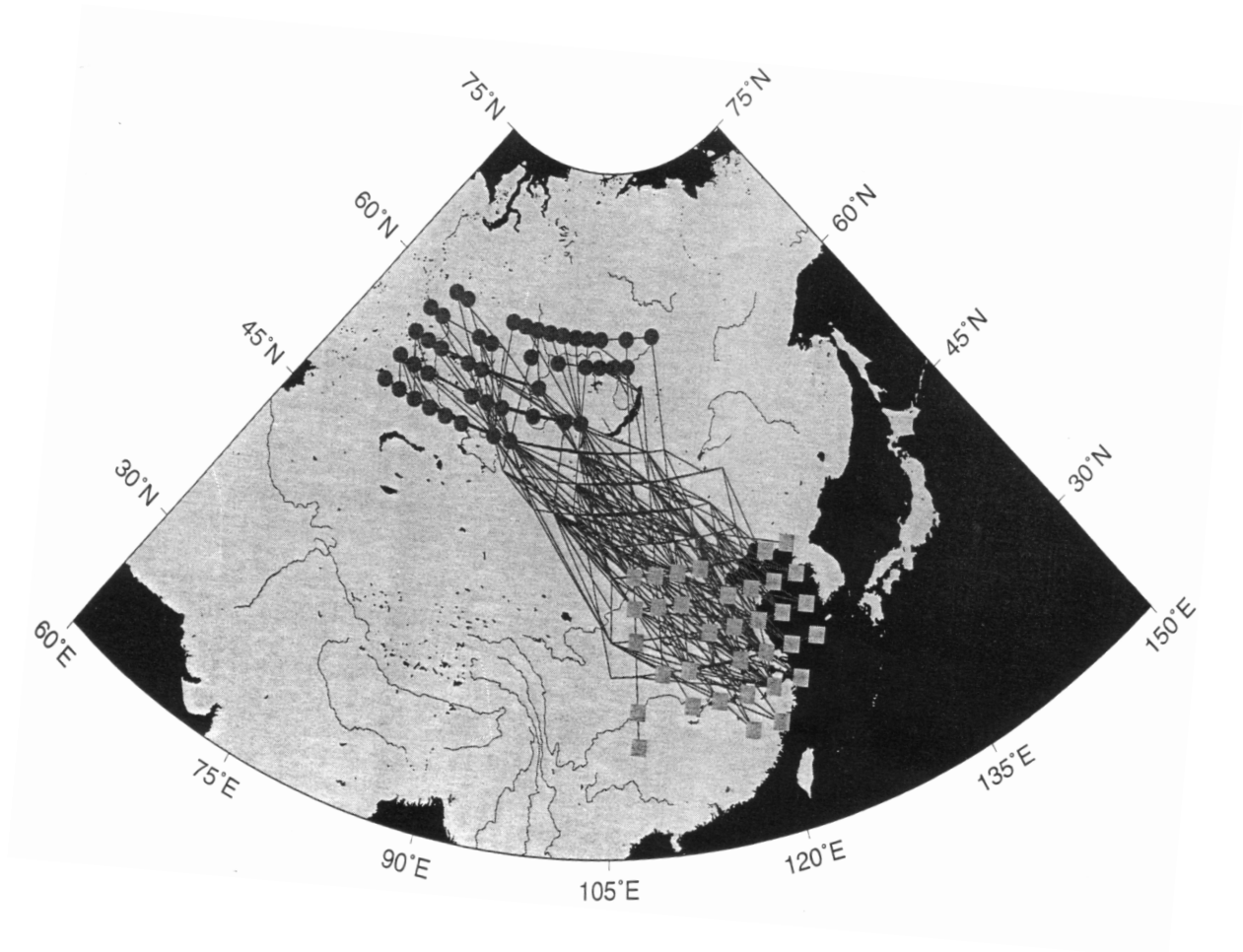


Fig. 1.13. Trajectories of the surface anticyclones associated with all cold surges for the period October–April of 1979/80–1994/95. The origin of the cold air and the ending of the surges are denoted in circles and squares, respectively. (After Zhang et al. 1997, Fig. 6.)

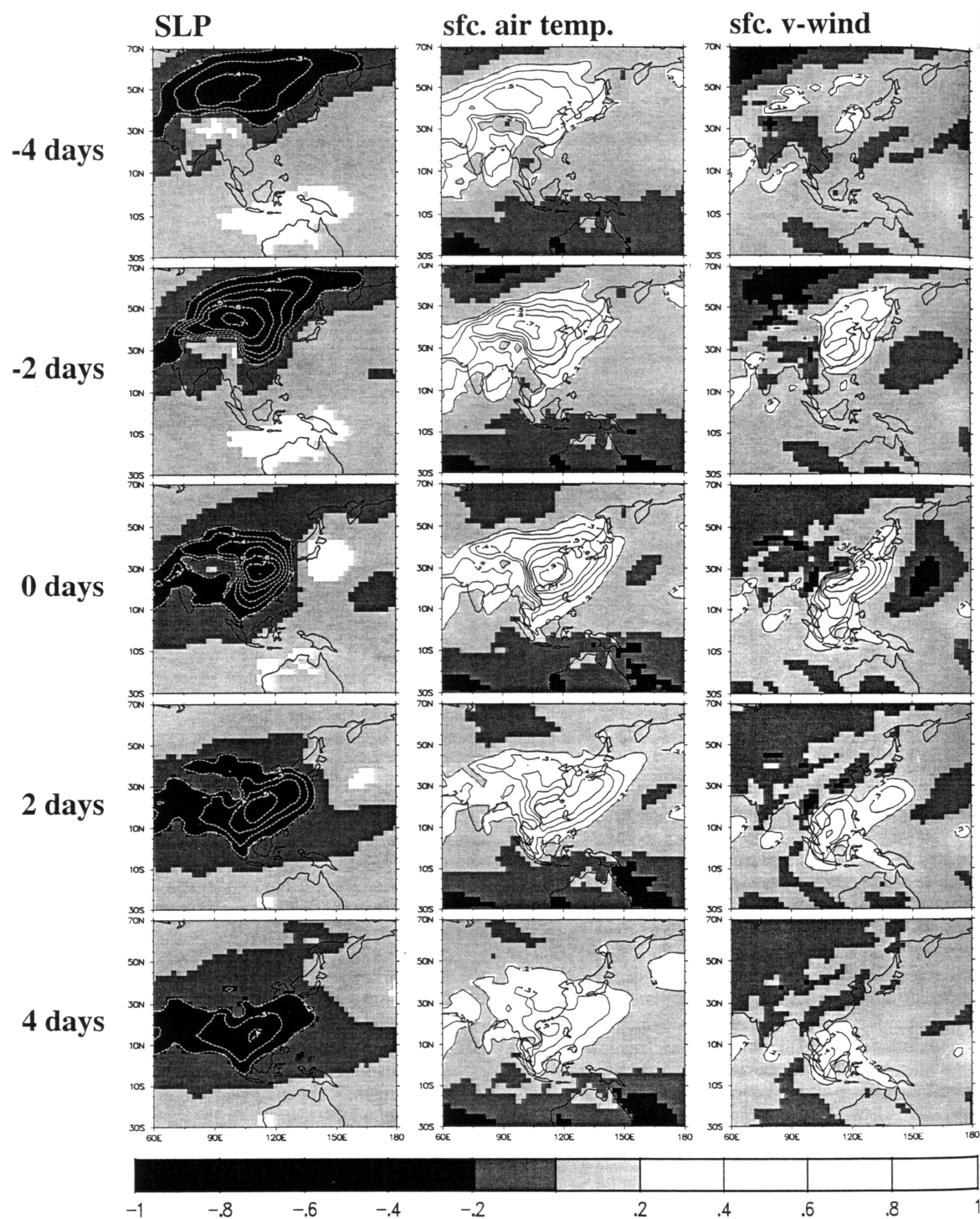


Fig. 1.14. Average lag correlations of area-averaged T_{sfc} with sea level pressure, surface air temperature, and meridional wind during the period mid-November through mid-March for 1979/80–1994/1995. Positive (negative) correlations larger (smaller) than 0.2 (-0.2) are white (shaded). For sea level pressure, negative correlations are plotted for $r < -0.2$ at an interval of 0.1. For surface air temperature and meridional wind, positive correlations are plotted for $r > 0.2$ at an interval of 0.1. (After Zhang et al. 1997, Fig. 7.)

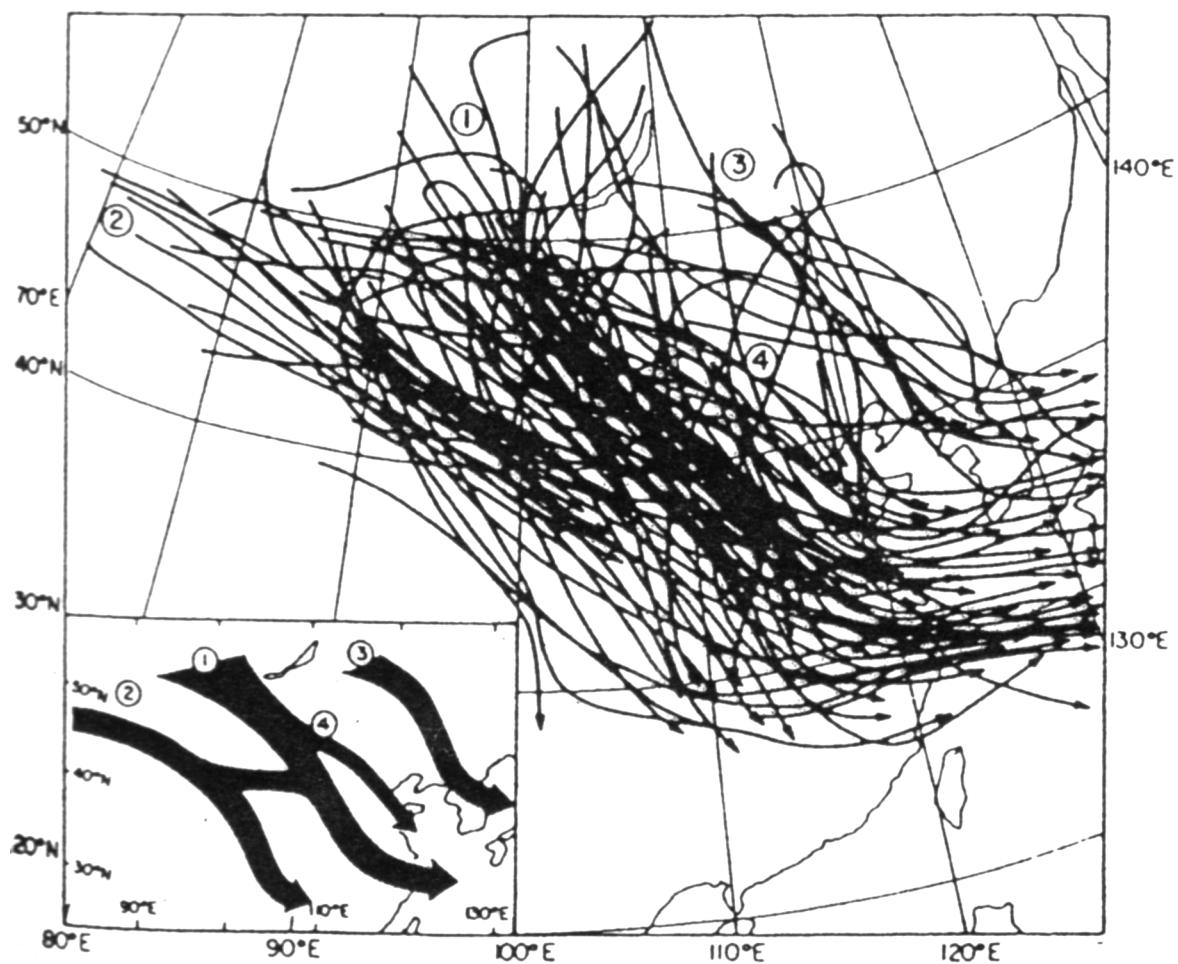


Fig. 1.15. Tracks of Siberian highs which crossed into China for the five winters (December–February) of 1980–1984. A schematic map of the tracks of the Siberian highs is inserted in the left bottom. (After Ding and Krishnamurti 1987, Fig. 1.)

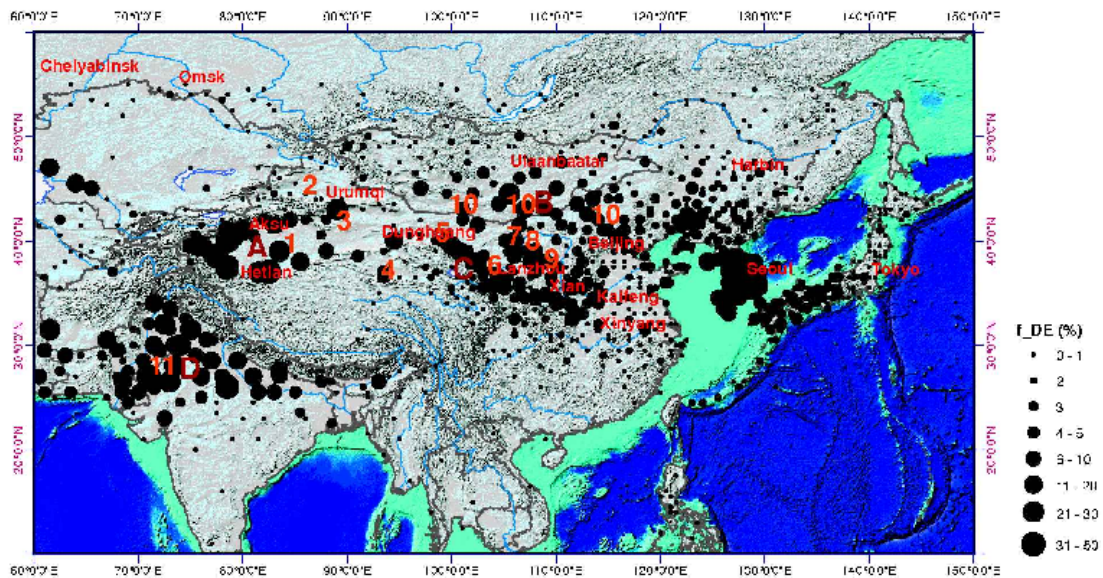


Fig. 1.16. Distribution of dust-episode frequency (f_{DE}) derived from the three hourly surface meteorological records for March, April, and May of 2000, 2001, and 2002. (After Shao and Wang 2003, Fig. 1.)

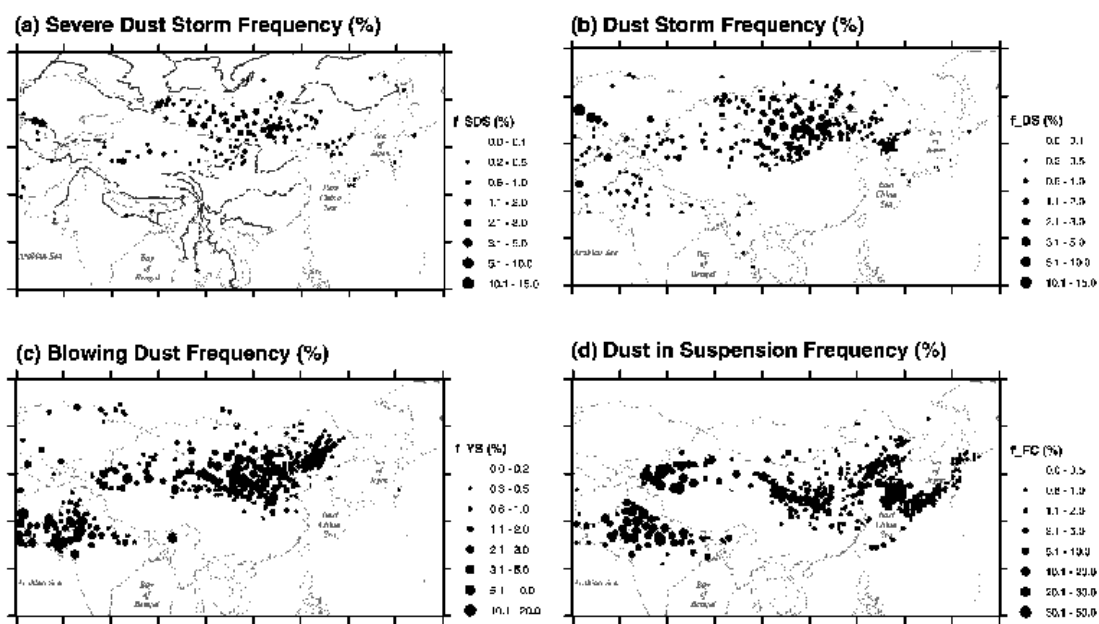


Fig. 1.17. Frequencies of (a) severe dust storms, (b) dust storms, (c) blowing dust, and (d) dust in suspension. (After Shao and Wang 2003, Fig. 2.)

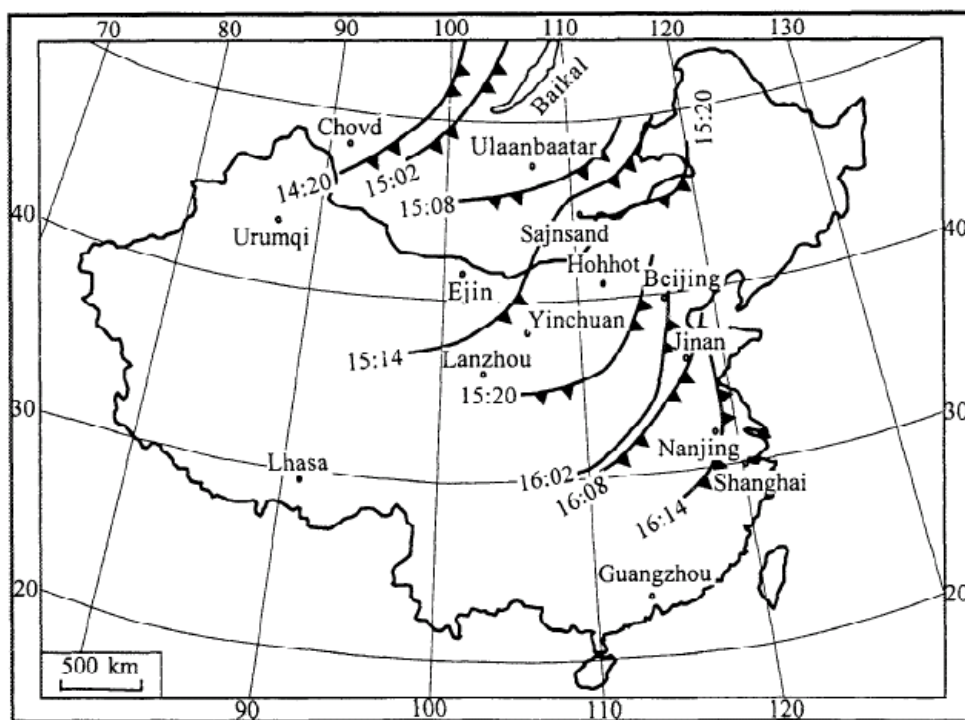


Fig. 1.18. Geographical position of traveling cold frontal system of 14–16 April 1998, which was accompanied with heavy dust storm event. (After Sun et al. 2000, Fig. 4.)

Chapter 2

Data and analysis method

2.1 Data

2.1.1 Surface observational data

The world surface data, which is based on SYNOP bulletins submitted by members of the World Meteorological Organization (WMO) through Global Telecommunication System (GTS), are obtained from the Japan Meteorological Agency (JMA) during 1999–2002. The data contain various meteorological variables such as air temperature, air pressure, vapor pressure, precipitation amount, wind component, visibility, and types of present/past weather event based on four observation times a day. The types of present weather event is used for examining a dust weather at the surface (see Section 2.3.1).

2.1.2 Satellite data

The weekly snow cover data consists of digitized maps distributed by the National Oceanic and Atmospheric Administration (NOAA) for the period 1971–2002. The snow cover extent prepared from visible imagery from NOAA polar-orbiting satellites supplemented with Geostationary Operational Environmental Satellite (GOES) and Meteosat satellite imagery. The data have an 89×89 polar stereographic grid in the Northern Hemisphere with cell size ranging from 16,000 to 42,000 km². Each grid cell contains one bit of

information for every week, the absence (0) or presence (1) of snow cover.

Hourly images of cloud patterns from the equivalent blackbody temperature (Tbb) data obtained from the fifth Geostationary Meteorological Satellite (GMS-5) by infrared channel-1 (IR1) were used in this study (available online at <http://weather.is.kochi-u.ac.jp/>). The GMS-5 is located 42,168 km from the center of the Earth and positioned above the equator above 140°E. The spatial coverage of this data ranges from 20°S to 70°N in latitude and from 70°E to 160°E in longitude with $0.05^\circ \times 0.05^\circ$ resolution.

The NOAA optimum interpolation (OI) sea surface temperature (SST) version two (OISSTv2) data are distributed by the NOAA Climate Diagnostics Center (CDC), Boulder, Colorado, USA (available online at <ftp://ftp.cdc.noaa.gov/Datasets/noaa.oisst.v2>). The data consist of weekly SST and sea ice concentration (SIC) with $1.0^\circ \times 1.0^\circ$ resolution during November 1982 through August 2002. More details of the analysis procedures of this data are described by Reynolds et al. (2002) or Rayner et al. (2003).

2.1.3 Objective analysis data

We used the 6-hourly 2-m temperature (hereafter surface temperature) from the European Centre for Medium-Range Weather Forecasts (ECMWF) reanalysis (ERA-40) data for 45 years from September 1957 to August 2002. The data have a horizontal resolution of $1.125^\circ \times 1.125^\circ$ at surface level and $2.5^\circ \times 2.5^\circ$ at the mandatory pressure level. Daily mean temperatures were obtained by averaging four times daily values.

In general, horizontal scale across cold front is only 100 km or less (Bluestein 1993). According to Conaty et al. (2001), horizontal temperature gradient calculated by using objectively analyzed data (cf. ERA-40) tends to be smaller values. To validate the detected cold front, we also use the ECMWF operational dataset which have horizontal resolution of $0.5^\circ \times 0.5^\circ$. Unfortunately, this operational data are geographically limited in 10°–60°N, 100°–160°E for the period 1992–2004.

2.1.4 Cyclone track data

The cyclone track data were obtained by passing the 6-hourly reanalysis sea level pressure (SLP) fields based on the dataset of NCEP–NCAR reanalysis for the period 1958–2002 through a modified version of the cyclone detection and tracking algorithm described by Serreze (1995) and Serreze et al. (1997). Cyclone detection relies on the identification of gridpoint SLP values surrounded by gridpoint values at least 1-hPa higher than the central point being tested. Cyclones were tracked by comparing system positions on subsequent 6-hourly charts using a nearest neighbor algorithm. For this study, only cyclones that existed for four or more consecutive observation periods (i.e., at least one day) were used. Application to the reanalysis output required that the reanalysis latitude/longitude grid to be first interpolated to a 250 km version of the National Snow and Ice Data Center (NSIDC) – Equal-Area Scalable Earth Grid (EASE-Grid).

2.1.5 Analysis period

The datasets used in this study are summarized in Table 2.1. As pointed out by Simmons et al. (2004), the surface temperature data includes a gap between 1966 and 1967 that is mainly caused by the lack of surface observations, particularly in East and South Asia (Fig. 2.1). In addition, the satellite-derived snow cover data are available after 1972. As pointed out by Clark et al. (1999), snow cover over land have close linkages with atmospheric conditions such as temperature, sea level pressure, and cyclone tracks. To investigate a relationships between cold frontal activity and meteorological conditions, it is important to examine the snow cover extent based on the observational data. For these reasons, although an activity of cold frontal systems are calculated for the entire period of ERA-40 (1957–2002), main analysis in this study focus on the period 1972–2002.

2.2 Analysis method

It is well known that a front is defined by the boundary between two air-masses which have different features of meteorological variables such as temperature and/or water vapor (Bluestein 1993). Hence, a traveling cold frontal system brings characteristic temporal changes in meteorological variables as follows: (1) rapid decrease of temperature, (2) intense precipitation associated with convective clouds along the cold front, and (3) abrupt changes in wind direction and/or wind speed. These features were also used to detect a cold air outbreak in several previous studies (Joung and Hitchman 1982; Boyle and Chen 1987; Chen et al. 2004).

One of the definition to determine frontal systems is the thermal front parameter (TFP) (Serreze et al. 2001; Tsumura and Yamazaki 2005):

$$\text{TFP} = -\nabla|\nabla\tau| \cdot (\nabla\tau/|\nabla\tau|) \quad (2.1)$$

where τ is a thermodynamic variable such as temperature (potential temperature), equivalent potential temperature. To avoid daily cycle due to surface heating, these thermodynamic variables are chosen from an isobaric surface in the lower troposphere such as 850-hPa level. Based on this definition, the TFP is proportional to the second derivative of thermodynamic variables. In a cold front, for example, the largest TFP areas are observed along a little to the warmer side of the axes of cold front.

As noted by Serreze et al. (2001), however, the TFP is not adopted over a high elevation area such as the Tibetan Plateau and Mongolian Plateau. Over the Eurasia, most of arid or semi-arid regions in Mongolia or northern China locate elevated areas ranging from 1000-m to 2000-m above sea level (see Fig. 2.2). To analyze frontal activities in continental-scale, it is better to define a new criterion that is not defined in horizontal gradient of meteorological variable at a specified isobaric level but is available in continental-scale as possible.

In this study, a passage of a cold front is simply identified by the differences in daily

mean temperature at a selected point: $\Delta T(t) = T(t) - T(t-1)$, where $T(t)$ represents the daily mean surface air temperature on the t -th day. When $\Delta T(t)$ exceeds the threshold value $\Delta T_r = -5$ K, we refer to the t -th day as a “cooling day”. In general, representative value of temperature cooling associated with a cold frontal passage varies by season and geographical location. However, to detect a cold frontal passage as simple as possible, we use the constant threshold value which is empirically determined and referred to previous studies (e.g., Joung and Hitchman 1982; Lau and Lau 1984). Since these studies were interested in cold air outbreaks in winter, the threshold value $\Delta T_r = -5$ K may be slightly severe to detect a traveling cold frontal system throughout a year. Consequently, we consider a frequency of cooling days as an indicator of the activity of strong cold frontal systems and use that to determine primary frontal zones over the Eurasia in the following sections.

2.3 Validation of cooling days

To compare the definition of the cooling day mentioned above with the passage of cold front, we first examine synoptic analyses using typical episode over Mongolia based on the high-resolution gridded data and surface observational data.

2.3.1 Case study: Strong cooling event in Mongolia during 6–7 April 2002

Figure 2.3 shows a timeseries of daily mean temperature, daily precipitation, and daily maximum wind speed at Erenhot (43.65°N, 112.00°E, 966-m) during March–May 2002. The daily mean temperatures are determined by three-hourly observations a day. This observation site locates the most frequent area of dust episode, as represented in Fig. 1.16.

Needless to say, daily mean temperatures should increase with season evolved, rapid drops of temperature can be seen during this period. The largest temperature decreases occurred in 6 April, the daily temperature dropped nearly 15 K a day. This rapid cooling

was not a local phenomena around this station. Horizontal distribution of daily temperature change (ΔT_{2m}) and the stations where strong wind speed was observed over Eurasia are depicted in Fig. 2.4 during 5–9 April 2002. The daily temperature changes are derived from ERA-40 data. The strong wind speed data are obtained from daily maximum values based on the Global Surface Summary of Day data. To clarify the figures, warming areas and weak wind speed stations are omitted.

On 5 April, strong cooling area can be seen in northwestern part of Mongolia centered around 50°N , 105°E (Fig. 2.4a). The cooling area advanced southeastward on 6 April (Fig. 2.4b), the maximum cooling exceeds -9 K. Associated with the southeastward movement of the cooling area, stations with strong wind speed (larger than 15 ms^{-1}) were also observed over Mongolia and northern China corresponding to the cooling area.

During the next three days the cooling area advances southward and southeastward and forms an arch-shaped spatial patterns from Japanese islands to southern China (Figs. 2.4c–e). After the passages of the cooling area, stations observed strong wind speed over Mongolia (see Figs. 2.4d, e). The track of cooling area is quite similar to the pathways of cold air and/or anticyclones associated with cold air outbreaks (Ding and Krishnamurti 1987; Zhang et al. 1997)

Figure 2.5 shows horizontal wind ($V_h = (u, v)$, vector), equivalent potential temperature (θ_e , contour), and absolute value of horizontal gradient of θ_e ($|\theta_e|$, shaded) at the 700-hPa level. Horizontal gradient of θ_e at each grid is computed from center differentiation using adjacent grid points. To depict frontal zones associated with this cold air outbreak, large values of $|\theta_e|$ ($|\theta_e| > 4 \text{ K (100 km)}^{-1}$) were only plotted.

At 0000 UTC 5 April 2002 (Fig. 2.5a), two cold frontal zones can be identified over East Asia. One can be seen over southern China extending southwestward from near Beijing to east of Tibetan Plateau (labeled CF1); the other one is located near the Lake Baikal (labeled CF2). Strong warm frontal zone (labeled WF1) is also identified, extending from Bohai to East China Sea.

On 6 April (Fig. 2.5b), the CF2 propagated southeastward and temperature gradient was strongly intensified from 5 April. The cyclone associated with CF1 and WF1 positioned on north of Korean Peninsula. The CF2 roughly extends southward from north of the Lake Baikal to the northwest of Beijing and the frontal zone curved to westward from that point. Consistent with the timeseries of daily mean temperature changes (Fig. 2.4), the air mass at Erenhot corresponds to the cold sector behind the cold front. Wind field around CF2 shows strong northerly, or northwesterly winds ($|V_h| > 20 \text{ ms}^{-1}$) were dominated behind CF2, and weak southerly or southwesterly winds ($|V_h|$ smaller than 10 ms^{-1}) were observed in the east of CF2.

On 7 April (Fig. 2.5c), the CF2 propagated eastward and the axes of frontal zone extends from northern Korean Peninsula through Shantung Peninsula toward east of Tibetan Plateau. Strong westerly or northwesterly flow was also dominant behind cold front. After 8 April, the CF2 slowly move eastward over the Korean Peninsula (8 April) and over Japan (9 April) (Fig. 2.5d, e).

Corresponding to the strong wind area behind CF2, dust outbreaks were broadly observed in the cold sector of CF2 (Fig. 2.6). These figures represent cloud images derived from equivalent black body temperature (T_{bb}) obtained by IR-1 channel on the GMS-5. The weather events of dust storm and suspended dust were obtained from the world surface data. Following Kurosaki and Mikami (2003), the dust outbreaks were identified by the code number of present weather ($\text{ww} = 07, 08, 09, 30\text{--}35, 98$). Suspended dust was represented in $\text{ww} = 06$. Comparing Figs. 2.5 and 2.6, dust storm area was intensively observed behind the cold front during the period 6–8 April (Figs. 2.6b–d). Hence, strong cooling day during 5–6 April 2002 can easily identify the traveling cold frontal system.

2.3.2 Relationship between cooling days and passages of cold fronts

As shown in Fig. 2.3, the strong cooling day was accompanied by the passages of cold front. To confirm general relationship between cooling days determined by rapid decrease

of surface temperature and the passages of cold front systems, we will examine the correspondence between them using long-term records. Figure 2.7 shows scatter diagram between ΔT_{2m} and $|\theta_e|$ at the 700-hPa level in Mongolia. The daily mean temperature changes were calculated using T_{2m} based on the ERA-40 at the nearest grid of Erenhot corresponding to 43.875°N, 112.50°E. The daily $|\nabla\theta_e|$ in Mongolia were obtained by the daily maximum of $|\nabla\theta_e|$ within analysis area (enclosed by red dashed line in Fig. 2.5) using ECMWF operational data with 0.5° horizontal resolution. Because of the limited period of the ECMWF operational data, comparison between ΔT_{2m} and $|\nabla\theta_e|$ was only examined during the period 1992–2002 spring (1012 days in total).

It is clear that negative correlations between ΔT_{2m} and $|\nabla\theta_e|$ can be seen in Fig. 2.7. In particular, most of strong cooling days ($\Delta T_{2m} < -5$ K) corresponded to large $|\nabla\theta_e|$. Overall, although the threshold value of $\Delta T_{2m} = -5$ K for determining a cooling day is based on synoptic experience, it is sufficient to identify a passage of a cold front.

Table 2.1. Summary of data used in this study

Table 2.1: Summary of data used in this study.

Surface atmospheric observation data			
dataset name	period	variables	source
globalISOD	Jan1994–Dec2004 (11-year)	daily min/max/mean Temp (global, over 10000 stations)	NCDC/NOAA http://www.ncdc.noaa.gov/oa/climate/dataset.html
world surface data	Jan1999–Dec2004 (6-year)	6-hourly, standard surface observation (global, over 10000 stations)	JMA obtained from the Meteorological Business Support Center, Japan
Objectively analyzed atmospheric data			
dataset name	period (# of grids)	spatial coverage and variables	source
ERA40 (23 pressure level)	Sep1957–Aug2002 (144 × 73 grids)	6-hourly, standard meteorological variables (global, 2.5° interval)	ECMWF http://www.ecmwf.int/research/era/
ERA40 (surface)	Sep1957–Aug2002 (320 × 161 grids)	6-hourly, surface variables (global, 1.125° interval)	ECMWF http://www.ecmwf.int/research/era/
ECMWF operational (13 pressure level)	Jan1992–Dec2004 (121 × 101 grids)	6-hourly, standard meteorological variables (100–160° E, 10–60° N, 0.5° interval)	ECMWF (archived by CGER, NIES)
Related meteorological data			
dataset name	period	variables	source
OISST v2	Nov1982–Dec2004 (22-year)	weekly SST, sea ice concentration (1° interval on globe)	CDC/NOAA http://www.cdc.noaa.gov/cdc/data.noaa.oisst.v2.html
NOAA-NESDIS snow cover	Jan1972–Dec2004 (33-year)	weekly snow cover (89 × 89 grids on a polar stereographic projection)	CPC/NOAA http://www.cpc.ncep.noaa.gov/data/snow/
Cyclone track	Jan1948–Jul2003 (55-year)	6-hourly center position, SLP, and related variables (250 km version of the NSIDC EASE-Grid)	CDC/NOAA ftp://ftp.cdc.noaa.gov/Datasets.other/map/storm/
Invariant data			
dataset name	variables	source	
ETOPO2	topography and bathymetry (global, 2-minute interval)	NGDC http://www.ngdc.noaa.gov/mgg/fliers/01magg04.html	

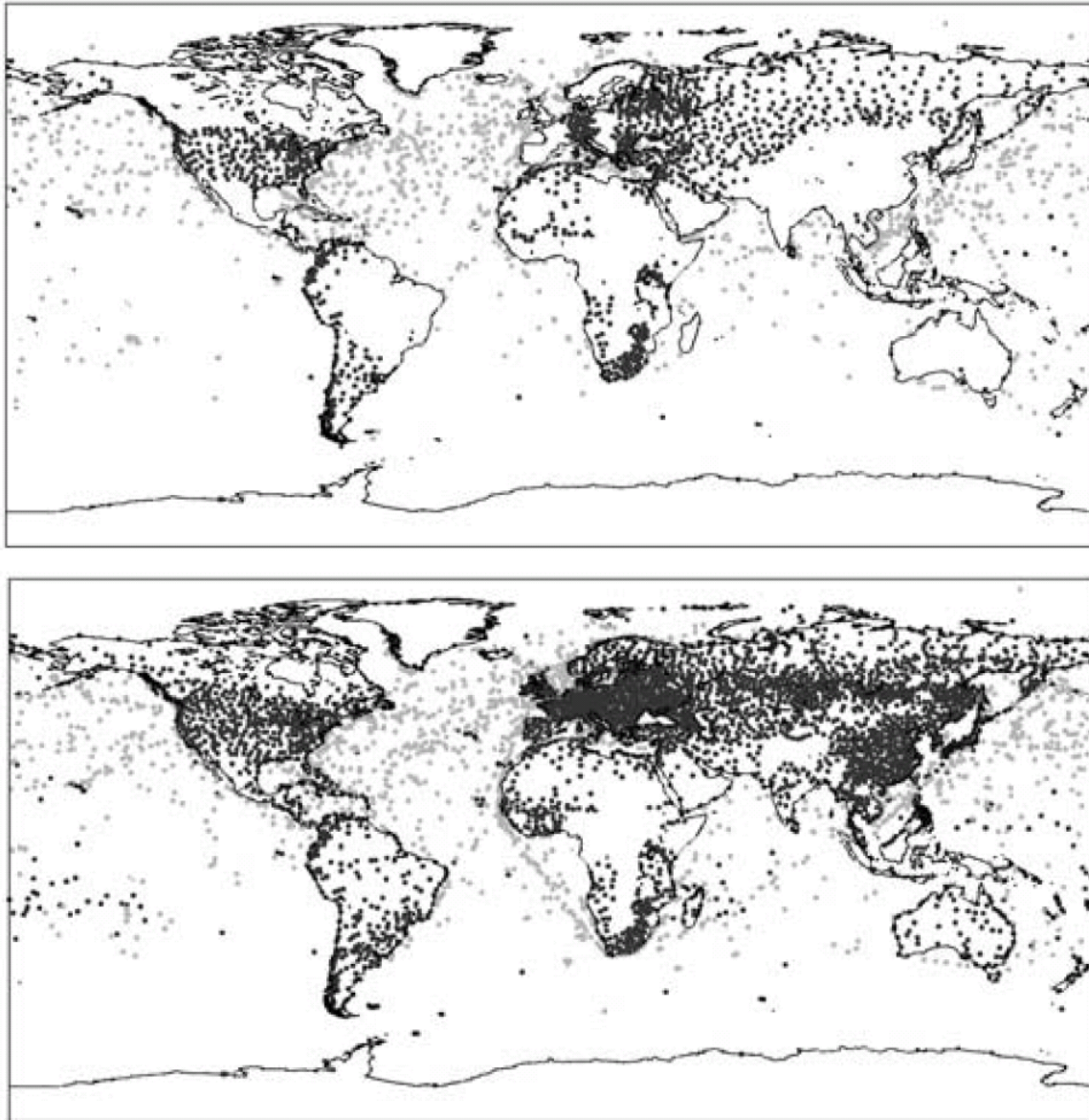


Fig. 2.1. Coverage of surface synoptic observations from land stations (black dots) and ships (gray dots) supplied to the ERA-40 data assimilation for 1200 UTC 1 July 1966 (upper) and 1200 UTC 1 July 1967 (lower) (After Simmons et al. 2004, Fig. 2).

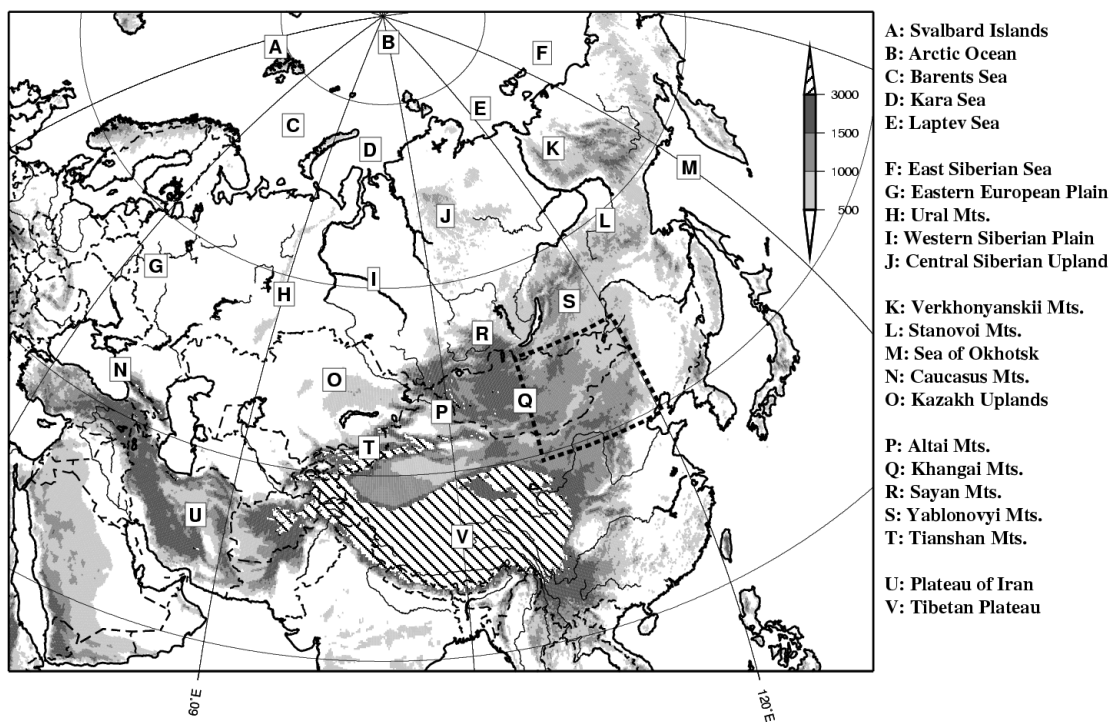


Fig. 2.2. Topography over the Eurasian continent

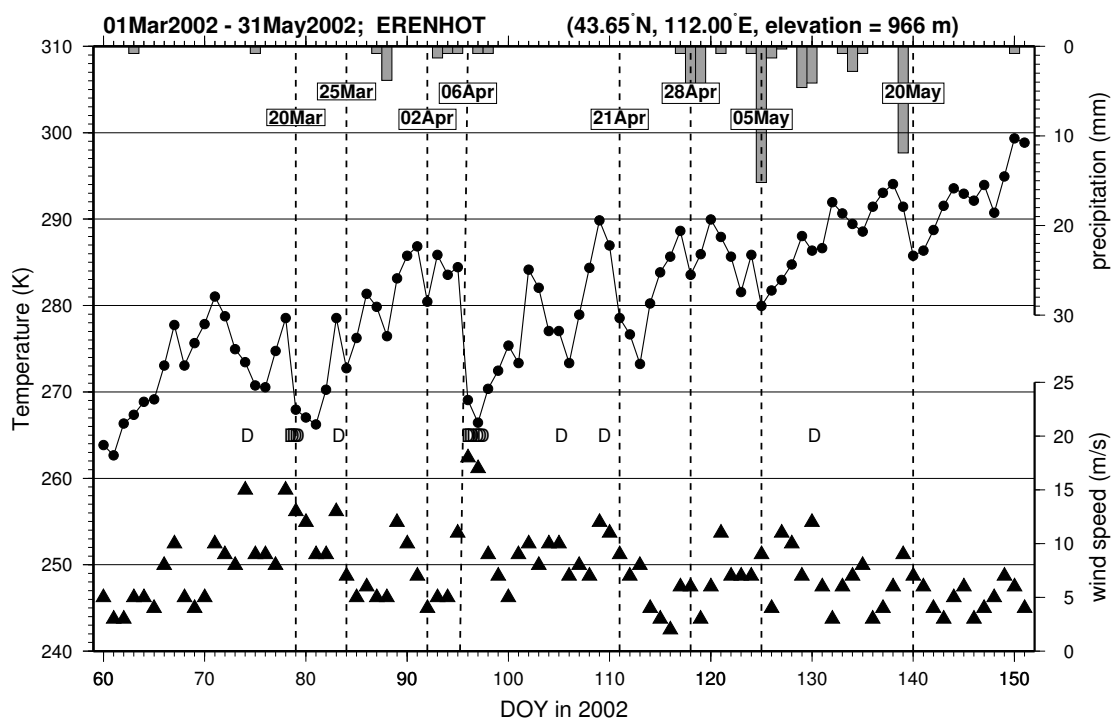


Fig. 2.3. Timeseries of daily mean surface air temperature (solid line with black circle), precipitation (gray shaded downward bar), and daily maximum wind speed (black triangle) at Erenhot, China (43.65°N , 112.00°E , 966 m) for the period 01 March – 31 May 2002. Daily mean temperature and daily maximum wind speed are determined by 3-hourly observations.

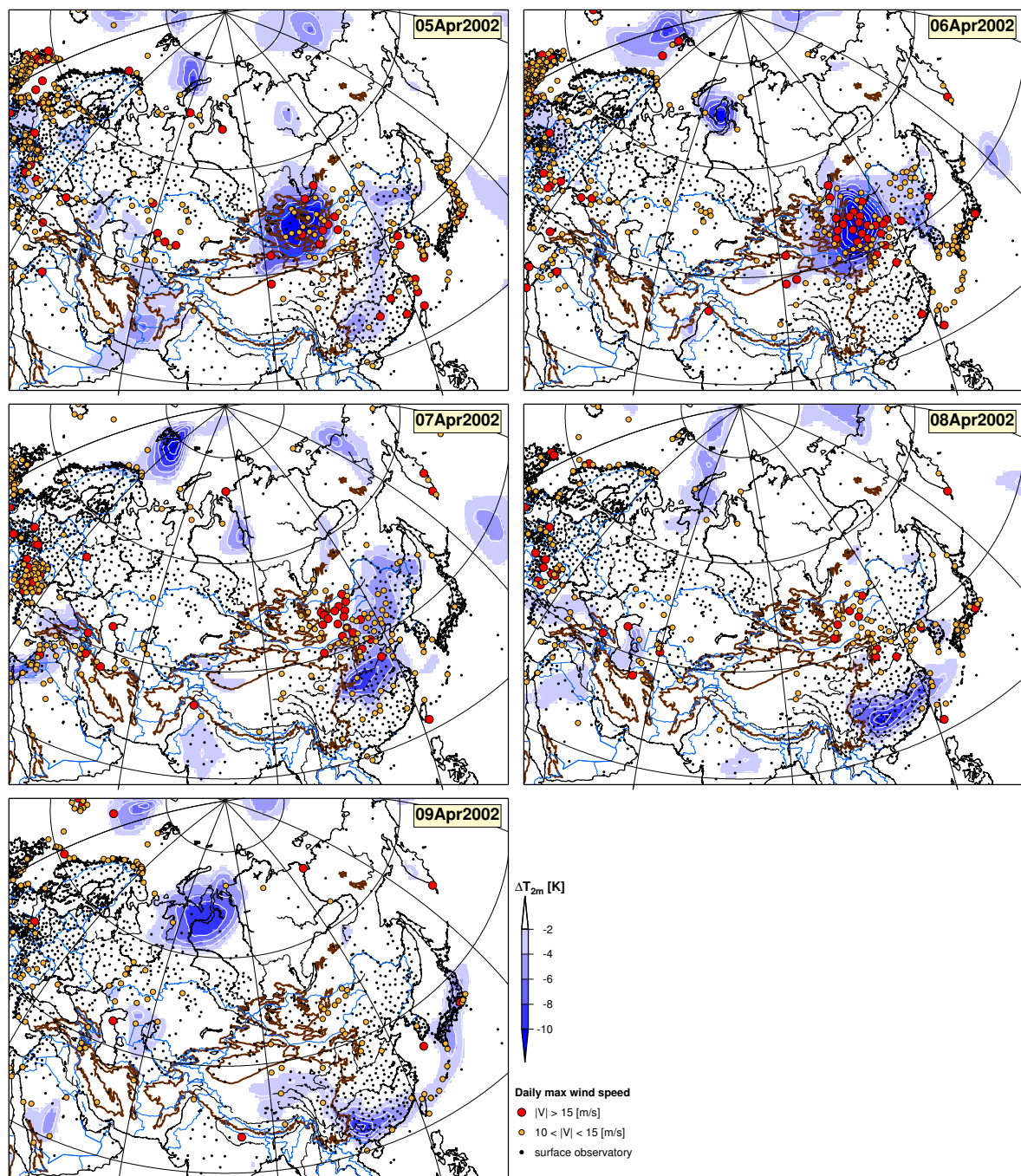


Fig. 2.4. Daily temperature change (cooling only, blue colored) and strong wind speed (colored circles) for the period 5–9 April 2002. Thick brown lines represent 1500-m terrain height contours based on the ETOPO2 obtained from the U.S. National Geophysical Data Center (NGDC).

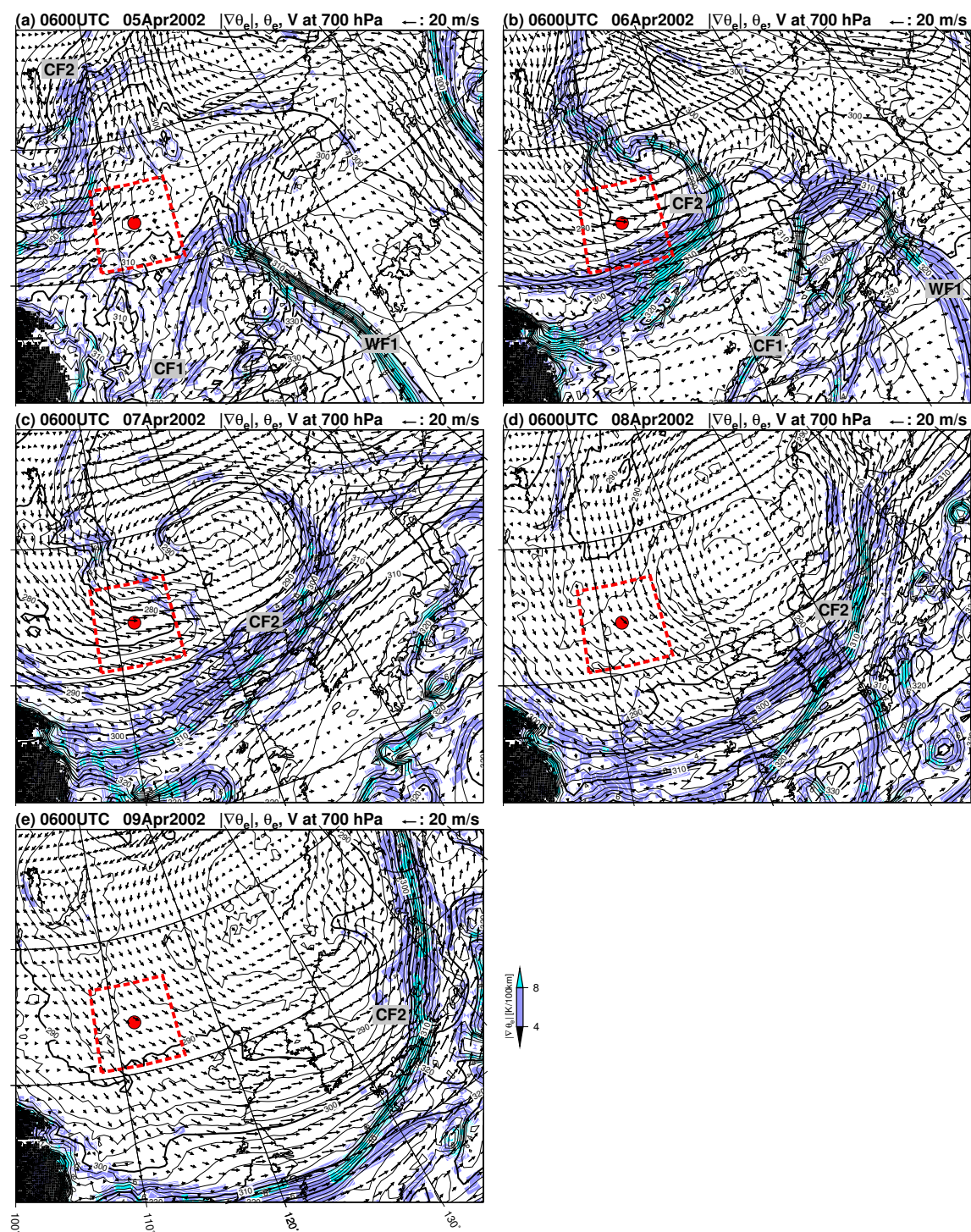


Fig. 2.5. Spatial patterns of potential temperature (θ_e ; contour), absolute value of horizontal gradient of θ_e ($|\nabla\theta_e|$; shade), and horizontal wind (vector) at 700-hPa for the period 5–9 April 2002. Mountain areas (elevation above 3000-m) are masked. Red circle indicate the location of Erenhot, China. Enclosed by red dashed line represents search area for detecting maximum $|\nabla\theta_e|$ in each day.

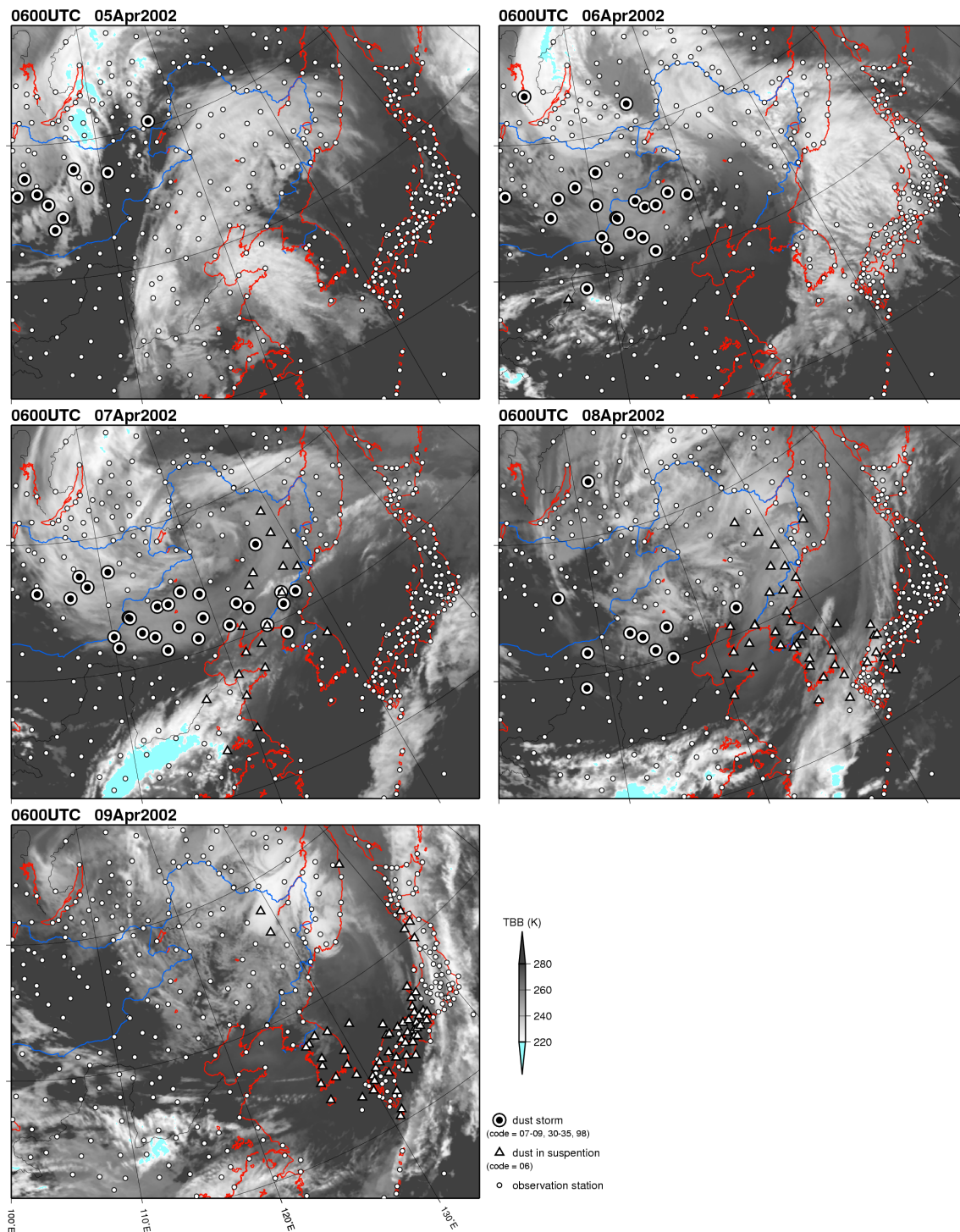


Fig. 2.6. Cloud pattern (shade) and surface observatories with dust episodes (symbol) for the period 5–9 April 2002. Large circles represent dust storm (WMO weather code = 07 – 09, 30 – 35, 98), triangles represent dust in suspension (WMO weather code = 06).

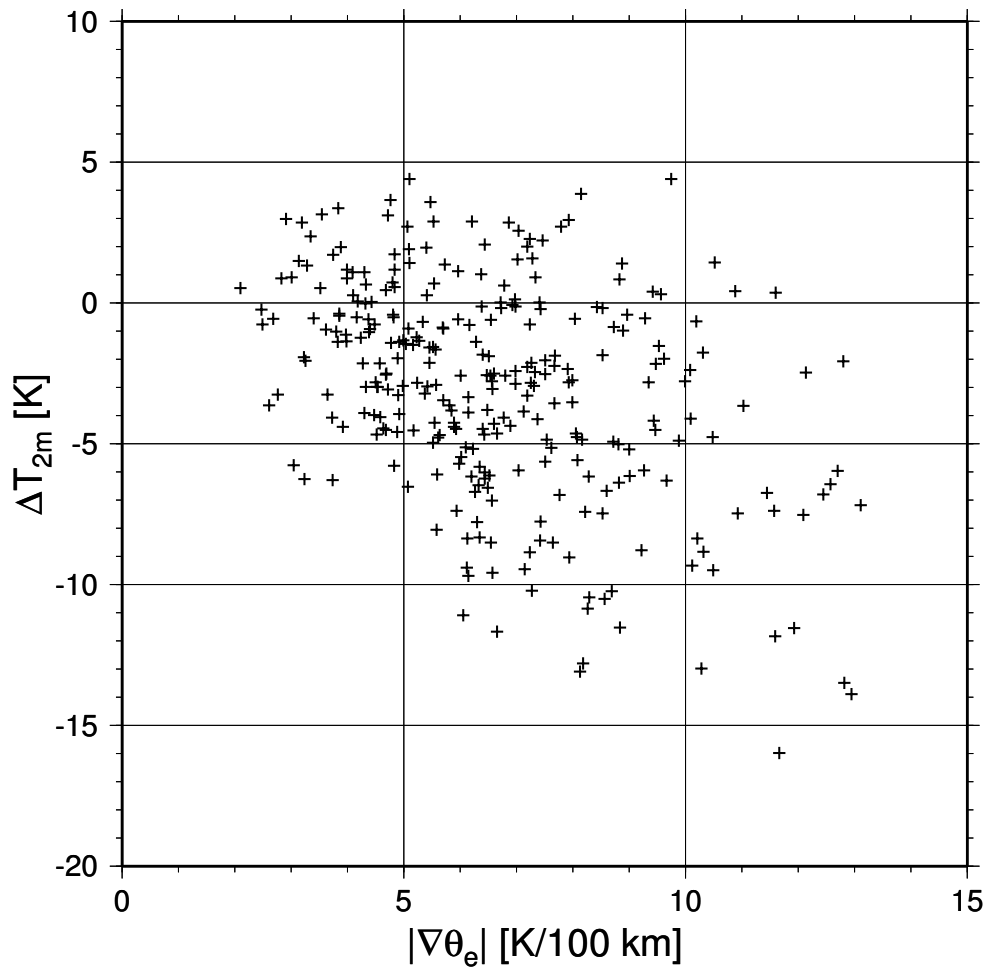


Fig. 2.7. Scatter diagram between ΔT_{2m} and $|\nabla\theta_e|$ for the period 1992–2002 spring.

Chapter 3

Climatological linkages between cold frontal activity and meteorological conditions

3.1 Horizontal distribution and seasonal march in frequencies of cooling days

3.1.1 Seasonal mean climatology in frequencies of cooling days

Figure 3.1 show the seasonal mean horizontal distributions in frequencies of cooling days for 1972 through 2002 over the Eurasia. The cooling day frequency (f_{cd}) in each grid cell is expressed as the ratio of total cooling days to the total number of days in each season. For convenience, we define a cooling region by f_{cd} exceeding 0.03 day^{-1} (approximately one cooling day per month).

In winter (December–February), the cooling region broadly covers the Arctic Ocean and northern Eurasia to the east of 30°E (Fig. 3.1a). The area of highest f_{cd} (0.17 day^{-1}) is found in north of the West Siberian Plain. A well-defined meridional gradient of f_{cd} is located along 45°N to the west of 80°E , the largest gradient zone shifts poleward from 80°E to 120°E . This poleward shift reflects the barrier effect of high mountains (Tianshan, Altai, Sayan, Hangayn, Yablnovy, Stanovoi, and Verkhoyansk) on the transport of cold air.

Other peaks in cooling day frequency are observed around the Svalbard Islands, Mon-

golia, and the seaboard along the Sea of Japan. The Svalbard Islands is placed on the marginal zone of Arctic sea ice in winter; there is a strong temperature gradient, where horizontal and vertical mixing are frequently observed in association with the intrusion of synoptic disturbances from the North Atlantic Ocean (Enomoto et al. 1993).

In spring (March–May), f_{cd} is generally smaller than that in winter except in eastern Mongolia (Fig. 3.1b). Two centers of high f_{cd} are evident. One over the West Siberian Plain (maximum f_{cd} is 0.10 day^{-1} ; about three cooling days per month), the other over eastern Mongolia and Inner Mongolia in China (maximum f_{cd} is 0.12 day^{-1} ; about 3.7 cooling days per month). The area of highest f_{cd} corresponds to the area of most frequent dust storm events (Sun et al. 2001; Shao and Wang 2003; Kurosaki and Mikami 2003) and the highest activity of cyclogenesis (Chen et al. 1991). From Fig. 3.1b, it can be seen that the cooling region extends to low latitudes to the east of Tibetan Plateau. The southward extension of the cooling region suggests the southward or southeastward passages of cold fronts through this area. As shown by Sun et al. (2000), cold fronts accompanied with dust storms are frequently observed in this area.

Summer (June–August) has the lowest frequency of cooling days in Eurasia (Fig. 3.1c). Areas of high f_{cd} are observed in two latitudinal belts, one in the northern part of Eurasia along the coast of the Arctic Ocean, and the other inland along $45^\circ - 50^\circ\text{N}$. Locations of these two belts of high cooling day frequency correspond to the Arctic and polar frontal zones in Eurasia, respectively (Serreze et al. 2001; Fukutomi et al. 2004).

In autumn (September–November), a large area of high f_{cd} covers northeast Asia north of 40°N (Fig. 3.1d). As in spring, there are two frequency peaks, one in eastern Mongolia and the other in western and central Siberia. While the location of the area of highest f_{cd} in Mongolia remains almost stationary throughout the season, the area of highest f_{cd} in Siberia shifts poleward from $45^\circ\text{--}55^\circ\text{N}$ in September to $55^\circ\text{--}65^\circ\text{N}$ in November (not shown). Possible reasons of this displacement are the seasonal transition of atmospheric circulation pattern and the extent of snow cover.

As shown in Figs. 3.1a–d, the region of eastern Mongolia and Inner Mongolia has high f_{cd} throughout the year. This area also corresponds to the primary region of dust outbreaks as shown in previous studies (Kurosaki and Mikami 2003; Shao and Wang 2003; see also Fig. 1.16). For these reasons, the analysis in the following section focuses on the area between $39.375^\circ - 50.625^\circ\text{N}$ and $102.375^\circ - 120.375^\circ\text{E}$ (enclosed by the dashed rectangle in Fig. 3.1). The area-averaged frequency of cooling days ($[f_{cd}]$) is calculated by the sum of cooling days divided by the product of total number of days and total number of grid cells within the analysis area. It should be noted that the calculated $[f_{cd}]$ values represent activity of strong cold frontal system but are not always proportional to the total number of passages of cold fronts. Since the threshold is set to a constant value, strong (weak) cold fronts provide a large (small) number of grid cells within the analysis area. Persistence of cooling day also affect that values. The relationships between $[f_{cd}]$ and statistics of cooling events will be discussed in Chapter 4.

The monthly mean climatology of $[f_{cd}]$ is shown in Fig. 3.2. Two frequency maxima is observed in late autumn (October to November) and late spring (April to May). The double peaks in the annual cycle are consistent with the monthly frequency of cold air outbreaks in East Asia (Zhang et al. 1997).

3.1.2 Monthly mean climatology in frequencies of cooling days

To provide some background for the discussions in the following chapter, this section provides a brief overview of the general climatology of several meteorological fields. It should be noted that the atmospheric circulation fields and surface conditions over continental area vary with seasonal evolution during spring. For example, in the east of 90°E , the distance of the poleward migration of mean snow line exceeds 1,000 km from 1 April to 1 May (Fig. 3.3). Therefore, a higher temporal resolution (e.g., monthly mean) is necessary to examine a seasonal march of the meteorological fields over Eurasia in spring.

Figure 3.4 exhibits monthly mean frequencies of cooling days in spring season. In March (Fig. 3.4a), there are maxima in cooling day frequencies in the Barents Sea, north

of the West Siberian Plain, and Inner Mongolia. The highest frequency maximum in the West Siberian Plain exceeds 0.13 (day)^{-1} near the lower Yenisei River. Although the Barents Sea is located in the Arctic Ocean, the frequency is larger than the maritime region. That may be caused by the sea ice extent over Barents Sea that corresponds to the marginal sea ice zone (see Fig. 3.8). Overall, the frequency maxima of cooling day are generally observed in the high-latitude areas to the north of 60°N except for the west of Pamir highland, south of Yangtze River and Inner Mongolia.

The frequency over Inner Mongolia increases in April (Fig. 3.4b) while the frequency over West Siberian Plain decreases and shifts southward. The frequency larger than 0.09 (day)^{-1} extends over eastern Mongolia through north and northeastern China. The axes of the highest frequencies from West Siberian Plain to Mongolia are generally oriented in a northwest-southeast direction which is similar to the tracks of cold air outbreaks (Ding and Krishnamurti 1987; Zhang et al. 1997).

In May (Fig. 3.4c), frequency maximum in the west of 90°E shifts southward from $60^\circ\text{--}70^\circ\text{N}$ (March, April) to $50^\circ\text{--}60^\circ\text{N}$ (May) while no distinct spatial displacement of frequency maximum occurs over Mongolia.

Thus, the geographical distribution in frequencies of cooling day shows different seasonal evolution between the western and eastern halves of the Eurasia continent. The area with frequency maxima in the west of 90°E slightly shift southward as a seasonal march. In early spring (March and April), the highest frequency area is observed over the Arctic area to the north of 60°N . The largest frequency area migrates to the south of 50°N in May. In contrast, in the east of 90°E , there is little displacement of the largest frequency area that locates over eastern Mongolia and Inner Mongolia in China. Two major maximum frequencies of cooling day extending from Siberia to Mongolia can be identified in March and April: (1) oriented in a north-south direction passing near the Lake Baikal, (2) oriented in a northwest-southeast direction passing over the Altai–Sayan Mountains. As noted earlier, these areas correspond to the tracks of cold anticyclones

associated with cold air outbreaks (Ding and Krishnamurti 1987; Zhang et al. 1997; see also Figs. 1.13 and 1.15).

Overall, the frequency of cooling days represents the activity of traveling cold frontal systems or cold air outbreaks throughout all seasons over Eurasia. In particular, the spatial and temporal characteristics of cooling days also express a cold frontal activity over the Mongolian Plateau, a region which is masked in the results of Serreze et al. (2001). For these reasons, the area-integrated frequency of cooling days [f_{cd}] in Mongolia is used as the indicator of cold frontal activity (CFA hereafter) in the following sections.

3.2 Monthly climatologies of meteorological conditions in spring

Day-to-day changes of surface air temperature are largely controlled by the passage of synoptic-scale disturbances. In addition, as pointed out by Groisman et al. (1994b), existence of snow cover also influences the near-surface temperature field. Before examining the interannual variation of cold frontal activities, it is required to know climatologies of meteorological conditions related to the surface temperature field. In this section, the monthly mean climatologies are described such as the temperature and circulation fields ranging from surface to the upper troposphere, cyclone tracks, activity of synoptic eddies, and snow cover extent.

3.2.1 Temperature and humidity

To investigate the boundary of air-mass, Fig. 3.5 show monthly mean climatology of equivalent potential temperature θ_e and its absolute value of horizontal gradient $|\nabla\theta_e|$ at the 700-hPa level in spring for 1972–2002. In many earlier studies, the representative isobaric level in the lower troposphere is adopted at the 850-hPa. It should be noted that due to the topography over East Asia, where the mean elevation of the Mongolian Plateau is about 1500 m, the influences of surface heating cannot be ignored over the area

when the analyzed level is selected at 850 hPa. The isobaric level used here is set at the 700-hPa level, which represents the free atmosphere.

In March, two areas with distinct maxima for $|\nabla\theta_e|$ (“mean frontal zone(s)” hereafter) are zonally elongated along midlatitude zones (Fig. 3.5a). One of the strongest areas extends from East Asia to central Pacific for $30^\circ\text{--}40^\circ\text{N}$. The other one is found from eastern North America to the just north of 40°N .

It is interesting that seasonal march of the intensity of frontal zones varies with region to region. Over the east coast of North America, the largest intensity of mean frontal zone occur in March ($|\nabla\theta_e| \approx 1.2\text{K (100 km)}^{-1}$ at 40°N , 70°W). As the season evolved, the maximum intensity gradually decreased along east coast of North America and the peak position can be observed in the lee side of Rocky Mountains during spring season. In contrast, there are little displacement for the maximum position of frontal zone and almost the same intensity over east Asia.

On the other hand, intensity of frontal zone over northern part of central Eurasia, which is considerably weaker than that of East Asia and North America, is the largest in April. The interpretation of the interesting seasonal evolution will be discussed at the end of this chapter.

3.2.2 Upper-air circulation and cyclone activity

To describe upper level circulation field, monthly mean geopotential height (contour) and activity of synoptic disturbances at the 500-hPa level (shade) are shown in Fig. 3.6. The activity of synoptic disturbances is defined by root-mean-square (RMS) of geopotential height obtained by filtering the subweekly component. Although the temporal range for representing synoptic-scale component was slightly different from several previous studies (e.g., Blackmon 1976; Nakamura 1992; Lau 1988; Rogers 1997), the upper period of eddy component mainly ranges from 6- to 10- day. In this study, based on the analysis by Rogers (1997), the band-pass filter with half power cut-off period of 2 and 8 days is applied to extract the variation associated with synoptic scale eddies.

The climatological mean height field clearly shows that two troughs can be easily identified over northeast North America and Eurasia, as pointed out by previous studies (e.g., Blackmon 1976; Lau 1988). Corresponding to these two troughs, the maxima of RMS are zonally elongated over the North Pacific and North Atlantic Oceans. While the intensity is rather weak compared to these two storm tracks, the minor maximum is found over northern Eurasia at 60°N. The local maximum of RMS field over northern Eurasia is called as “Eurasia storm track”, as noted by Lau (1988).

In comparison with these three storm tracks, there are distinct differences with regard to the seasonal march. In spring, the activity of the Atlantic and Pacific storm tracks is largest in March and gradually decreased with seasonal evolution. On the other hand, the strength of Eurasia storm track has the largest value in April. This seasonal march is consistent with the results by Whittaker and Horn (1984).

Figure 3.7 shows the mean motion and development rate of cyclones in spring for 1972–2002. The mean moving vector is computed by a simple average of all identified cyclones in each grid cell. The traveling speed and direction of a cyclone are calculated from the 6-hour differences of the spatial position in the EASE-Grid. The development rate of a cyclone is defined by the SLP change in 6-hour. A latitudinal adjustment is performed for the mean SLP change calculation. For clarity of figures, cyclone systems fewer than 10 events are omitted. The major cyclone tracks are seen in the North Pacific and the North Atlantic. Consistent with the results by Lau (1988), cyclones were generated in the entrance region of the jet streams off the east coast of the continents (see Fig. 1.7) and dissipated in just north of the maximum RMS values. In the North Atlantic, most of the cyclones move northeastward to the Arctic Ocean (Fig. 3.7). The intrusion of cyclones into the Arctic Ocean from the North Atlantic is a well-known features (Whittaker and Horn 1984; Rogers and Thompson 1995; Clark et al. 1999). On the northern Eurasia, cyclones develop in the East and West Siberian Plain in April and May (Figs. 3.7b, c) while cyclones dissipate in March (Fig. 3.7a). This result is also identified in the

seasonal evolution for RMS fields (Fig. 3.6). Continental cyclones over East Asia generally form in the leeside of Altai-Sayan Mountains and develop in downstream area (eastern Mongolia and northeastern China), as shown by Whittaker and Horn (1984). These cyclones correspond to “Mongolian cyclones” (Boyle and Chen 1987) or “Baikal cyclones” (Chen et al. 1991) (see also Figs. 1.10, 1.12)

3.2.3 Snow and sea ice

As discussed by Clark et al. (1999), temperature anomalies and cyclone tracks also correlated to the changes of snow-cover extent in Eurasia. To examine the interannual variations of cold frontal activity, it is important to know about climatological mean fields about these cryospheric variables.

Long-term averaged snow cover extent and sea ice concentration (SIC) are displayed in Fig. 3.8. As noted by earlier studies, snow line (southern boundary of snow cover area) tends to rapidly shift poleward in spring (Shinoda et al. 2001; Ueda et al. 2003). To illustrate a climatology of snow cover and SIC fields, a pentad (5-day) mean climatology is computed at each mid-month. Since the pentad climatology of these values is simply averaged by corresponding weekly data, the climatology of snow cover and SIC is represented by an existence ratio in snow cover and mean SIC, respectively. Based on the above mentioned procedure, pentad climatology is calculated by using 22–23 years in each pentad for snow cover data and using 15–16 years in each pentad for SIC data. Following the results by Clark et al. (1999), “variant” region of snow cover or SIC in each month are defined by the probability of snow cover and mean SIC ranging from 10 to 90%. To avoid the uncertainty of snow cover over the Tibetan Plateau (Clark and Serreze 2000), interannual variations of snow cover in that area will not discuss in the following section.

In March (Fig. 3.8a), invariant region of now cover (light blue area) largely covers the north of 45°–55°N in Eurasia. As season evolved, invariant region of snow cover shrinks and mean snow line (boundary of variant/invariant region of snow cover) rapidly shifts poleward from March to May. As expected, the mean snow line nearly corresponds to 0°C

line (red dashed line in Fig. 3.8). In Mongolia, although the variant snow cover area is identified in the mid-March and April, the snow free surface covers entire area in mid-May except the Altai-Sayan mountains (Fig. 3.8c). In mean SIC fields, high SIC areas are maintained on the whole of the Arctic Ocean while the poleward retreat of snow cover extent rapidly progresses in the continental area.

3.3 Climatological relationships between cold frontal activity and meteorological conditions

In this section, long-term averaged spatial distributions and its seasonal changes of the frequency of cooling day and several meteorological variables that relate to the variations for temperature field are explored. Based on these results, there were characteristic seasonal evolutions of the cooling day frequency in springtime Eurasia continent.

One of the most striking features in the seasonal evolution of cooling day frequency is spatial differences in seasonal march between the West Siberian Plain and eastern Mongolia. In the West Siberian Plain, the frequency of cooling day is largest in the north of 60°N. As shown in Figs. 3.8a and b, snow cover is observed over broad area of Eurasia in early spring. The contiguous sea ice area can be seen in the Arctic Ocean for the period. Hence, surface conditions of sea ice and snow cover make an “ice continent” from the mid- and high-latitude area of Eurasia to the Arctic Ocean. The existence of surface snow cover and ice contribute to make a favorable condition for the formation of continental polar air (Curry 1983; Curry 1987). Indeed, strong and deep temperature inversion layer is dominant over northern Siberia (Serreze et al. 1992). As shown in Figs. 3.7a and 3.7b, cyclones frequently travel from north Atlantic Ocean through the Barents Sea into northern coastal Siberia along the Arctic Ocean. Therefore, the highest frequency of cooling days in the north of West Siberian Plain may be caused by synoptic disturbances.

The highest frequency area of f_{cd} in the west of 90°E shifts southward from the coastal

region of the Arctic Ocean to 50° and 60°N in spring (Figs. 3.4a–c). This meridional shift is caused by the poleward shift of snow cover and the low activity of cyclones originated from the North Atlantic Ocean. The snow cover extent and temperature field (Figs. 3.5 and 3.8) suggest that the southward shift of the highest f_{cd} area in the West Siberian Plain relate to the poleward retreat of snow cover and surface heating in snow-free area. As noted in Groisman et al. (1994b), snow covered area tends to form a cold air through snow-albedo feedback compared with snow-free area. As a result, the boundary area between snow-covered and snow-free area have a large temperature gradient (Fig. 3.8c). In addition, as shown in Figs. 3.7a and 3.7b, cyclones originated from North Atlantic move northeastward into the Arctic Ocean in early spring (March and April). This cyclone track is somewhat intermittent over North Atlantic in May. In the meanwhile, cyclones passing through the West Siberian Plain originate from the continental interior near the Black Sea, Caspian Sea, and Aral Sea (Fig. 3.7c). Therefore, the poleward shift of snow line and the seasonal change of cyclone activity also contribute to the southward shift of the largest frequency of cooling days.

In contrast, the spatial displacement in the highest frequency of f_{cd} is not clear over eastern Mongolia. The most appreciable explanation is the effect of topography. The topographic depression zone is oriented from northwest–southeast direction from the West Siberian Plain through the Lake Baikal into the Mongolian Plateau (Figs. 1.11 and 2.2). Because of the geographical condition, near-surface cold air in Siberia moves southeastward passing through the valley (or col). Indeed, this route is the primary pathway of anticyclones associated with monsoonal surges (Figs. 1.15 and 1.13).

The largest frequency of f_{cd} over eastern Mongolia is observed in April or May (Figs. 3.2 and 3.4). In March, cold anticyclone (i.e., Siberian high) is still dominant over the Eurasia and mean snow line is located along 40°N. As the season evolved, snow line shifts poleward to the south of Siberia and surface heating increases in snow-free area in Mongolia. In late spring, cold air frequently intruded to eastern Mongolia passing through

the valley or col (e.g., near the Lake Baikal) from Siberia where snow cover is still observed in April and May. As a result, local heating and cold air advection originated from Siberia will produce the largest frequency of f_{cd} in this period.

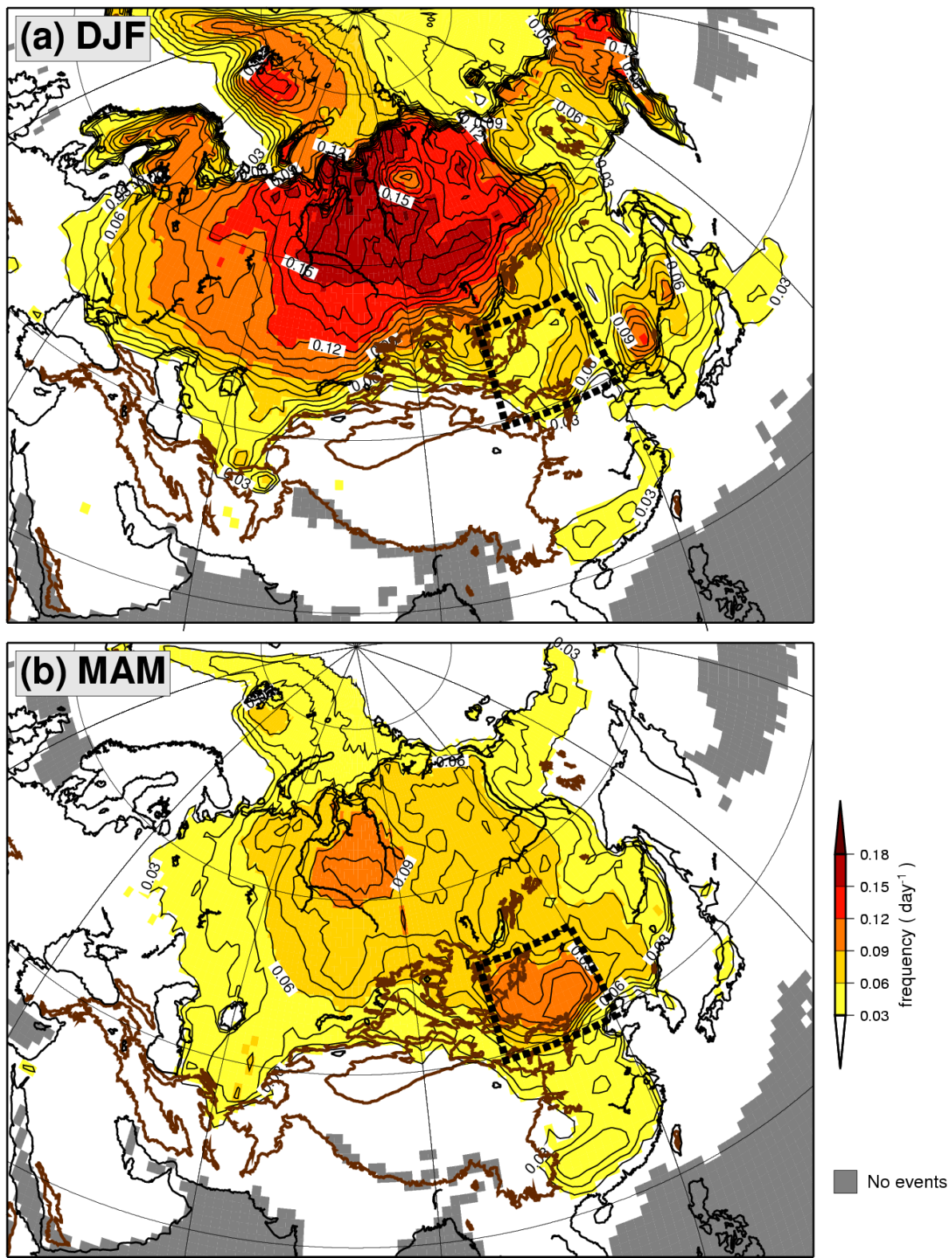
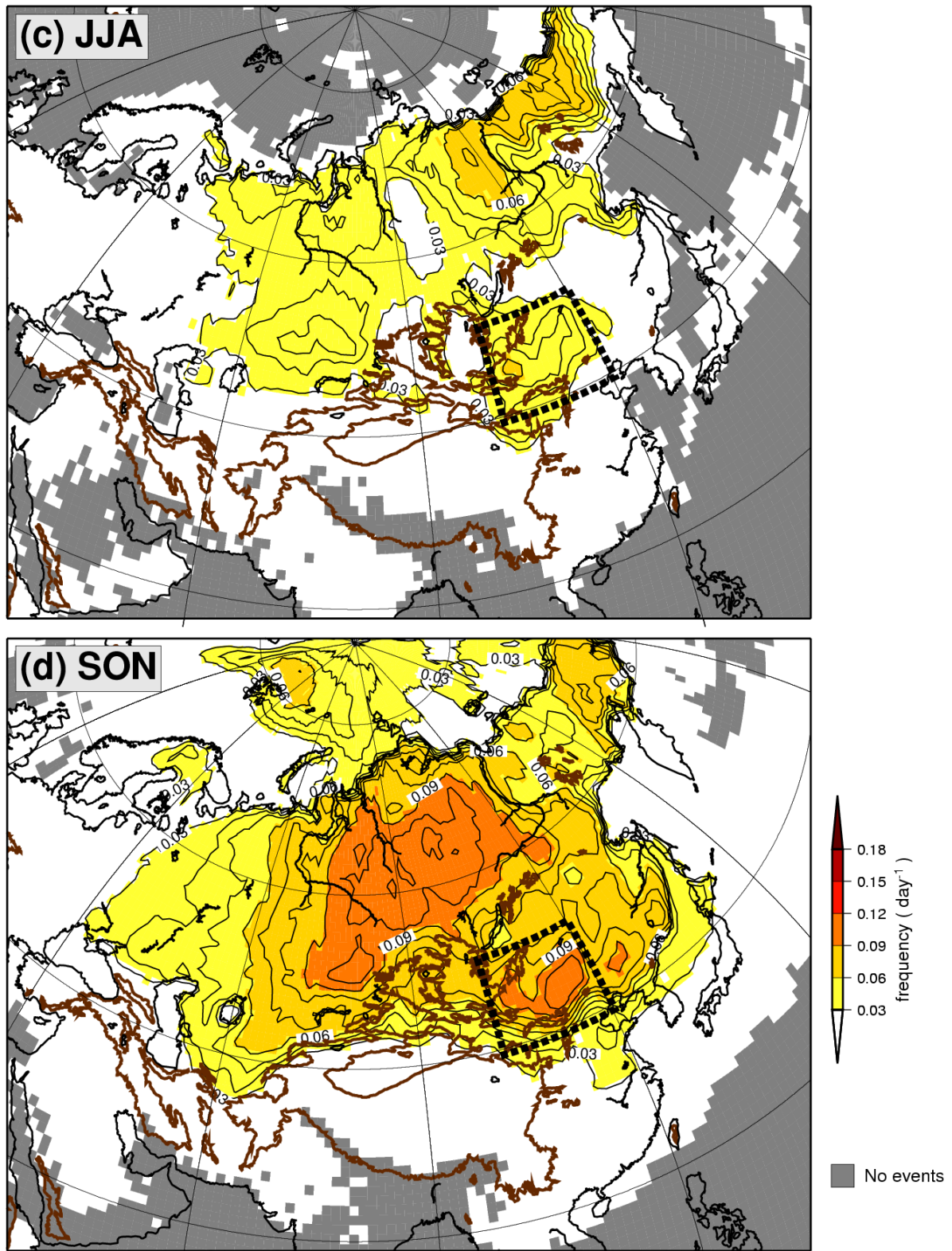


Fig. 3.1. Seasonal mean frequency of cooling days for 1972–2002. (a) December–February (DJF), (b) March–May (MAM), (c) June–August (JJA), and (d) September–November (SON). Shaded area where cooling day frequency exceeds 0.03 day^{-1} regard as cooling region in this study. Thick brown lines represent 1500-m terrain height based on the ETOPO-2. Thick dashed line enclose an analysis area in this study.



(Continued.)

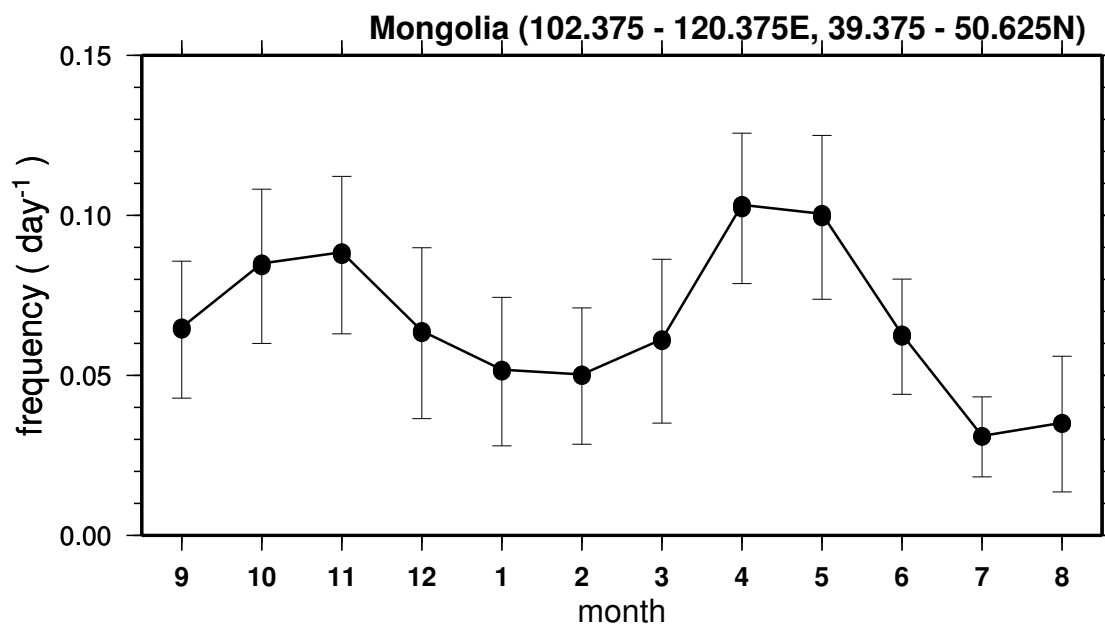


Fig. 3.2. Monthly climatology in frequencies of cooling day in Mongolia (39.375 – 50.625°N, 102.375 – 120.375°E; 187 grids within the area). Interannual variations are represented by ± 1.0 standard deviations (bar) in each month.

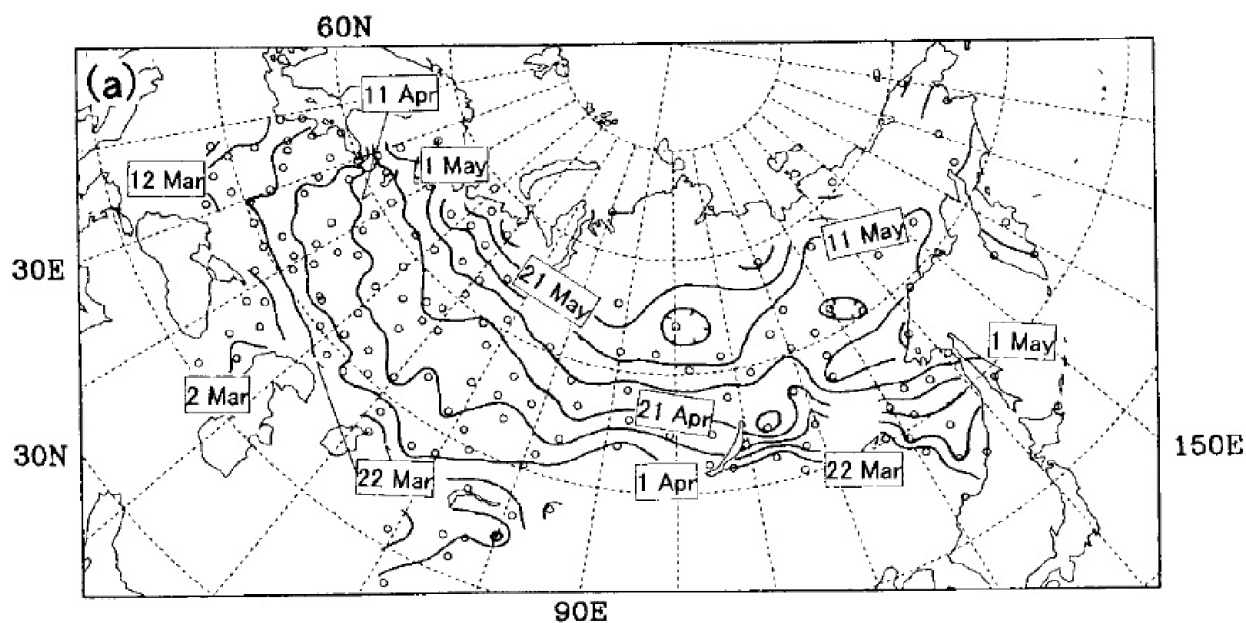


Fig. 3.3. Climatology (1966–1990) of snow-disappearance timing in the Former Soviet Union. The contour interval is two pentads (10-day). (After Shinoda et al. 2001, Fig. 1.)

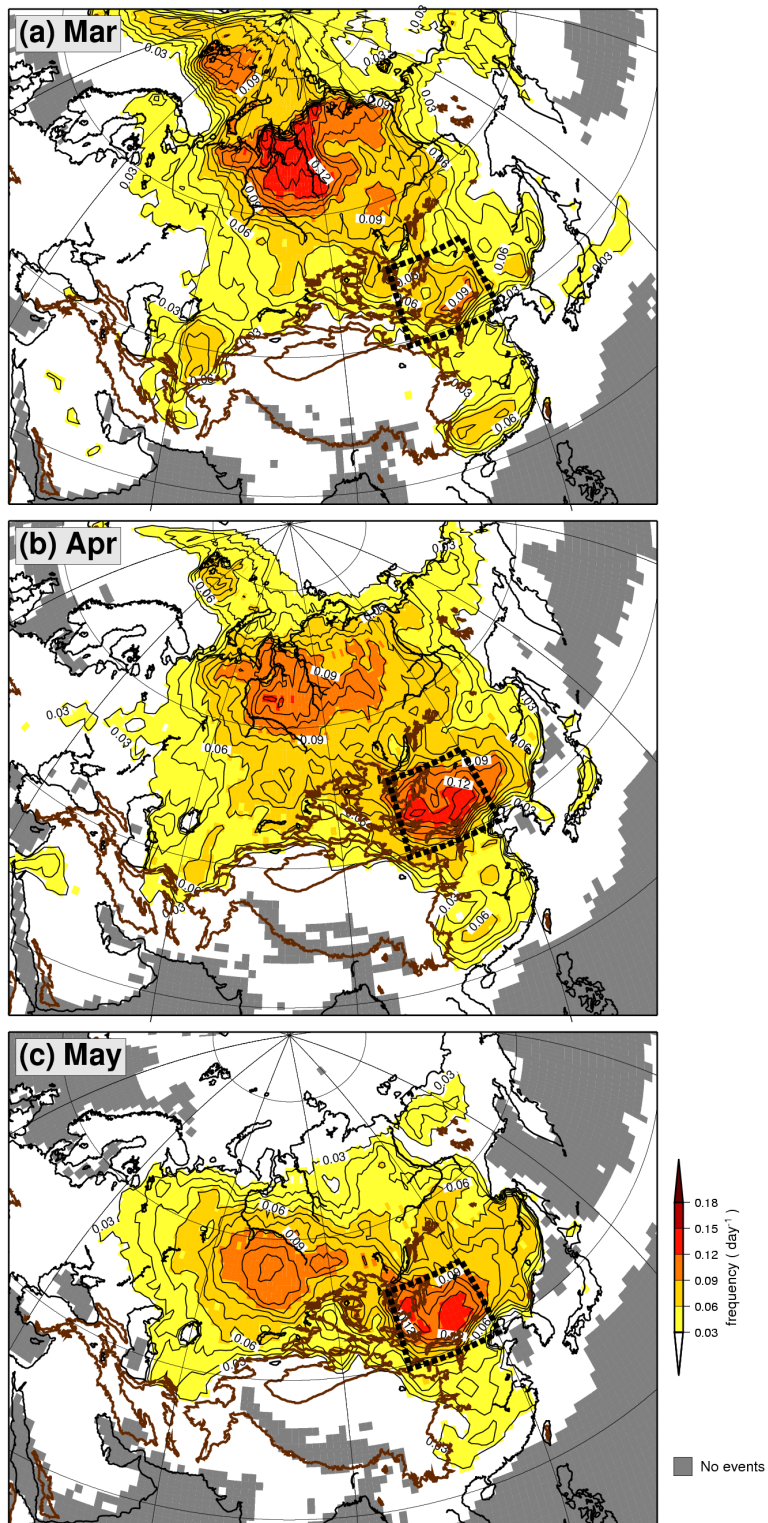


Fig. 3.4. Same as Fig. 3.1, but monthly mean climatologies during 1972–2002 spring. (a) March, (b) April, and (c) May.

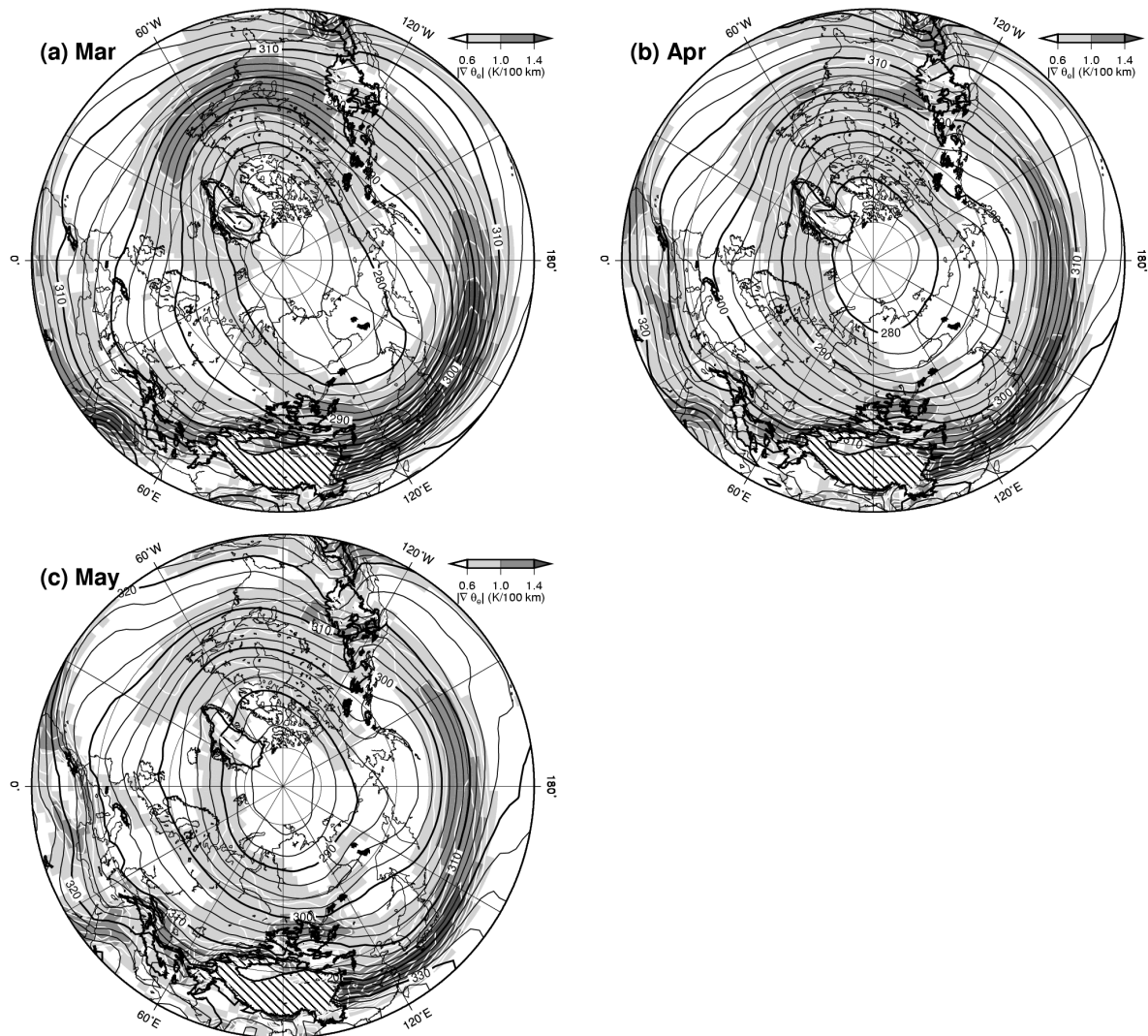


Fig. 3.5. Monthly climatologies of θ_e (contour) and $|\nabla\theta_e|$ (shaded) at the 700-hPa level during 1972–2002 spring. Contour interval for the time averaged θ_e is 2.5 K and for the gradient is 0.2 K (100 km)⁻¹.

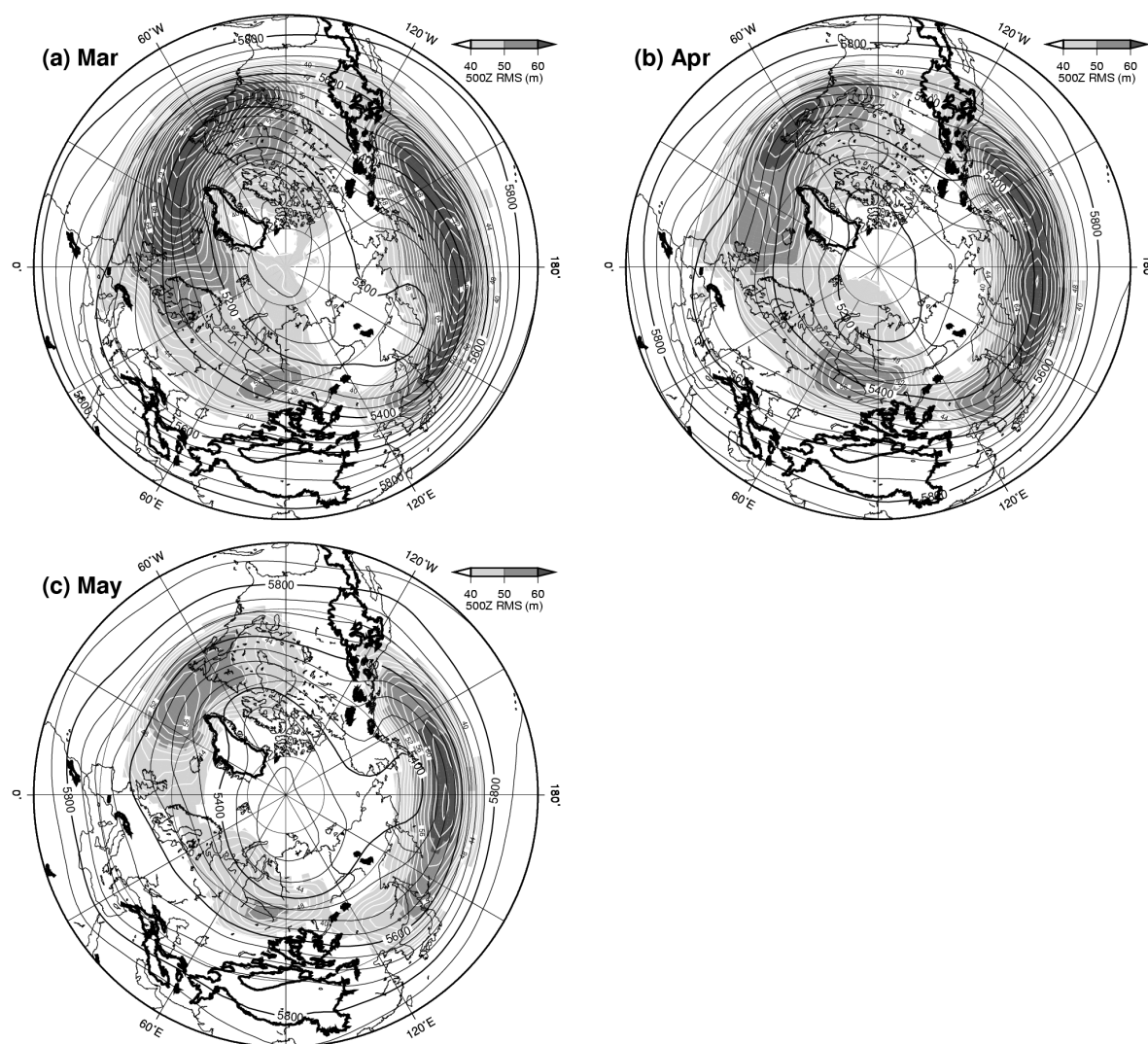


Fig. 3.6. Monthly climatologies of the geopotential height (contours) and activity of synoptic-scale eddies (shaded) at the 500-hPa level. The activity of synoptic-scale eddies is determined by root-mean-squares (RMS) of geopotential height in component of 2–8 day cycle. Contour interval for the time averaged height field is 50-m and for the RMS field is 2.5-m.

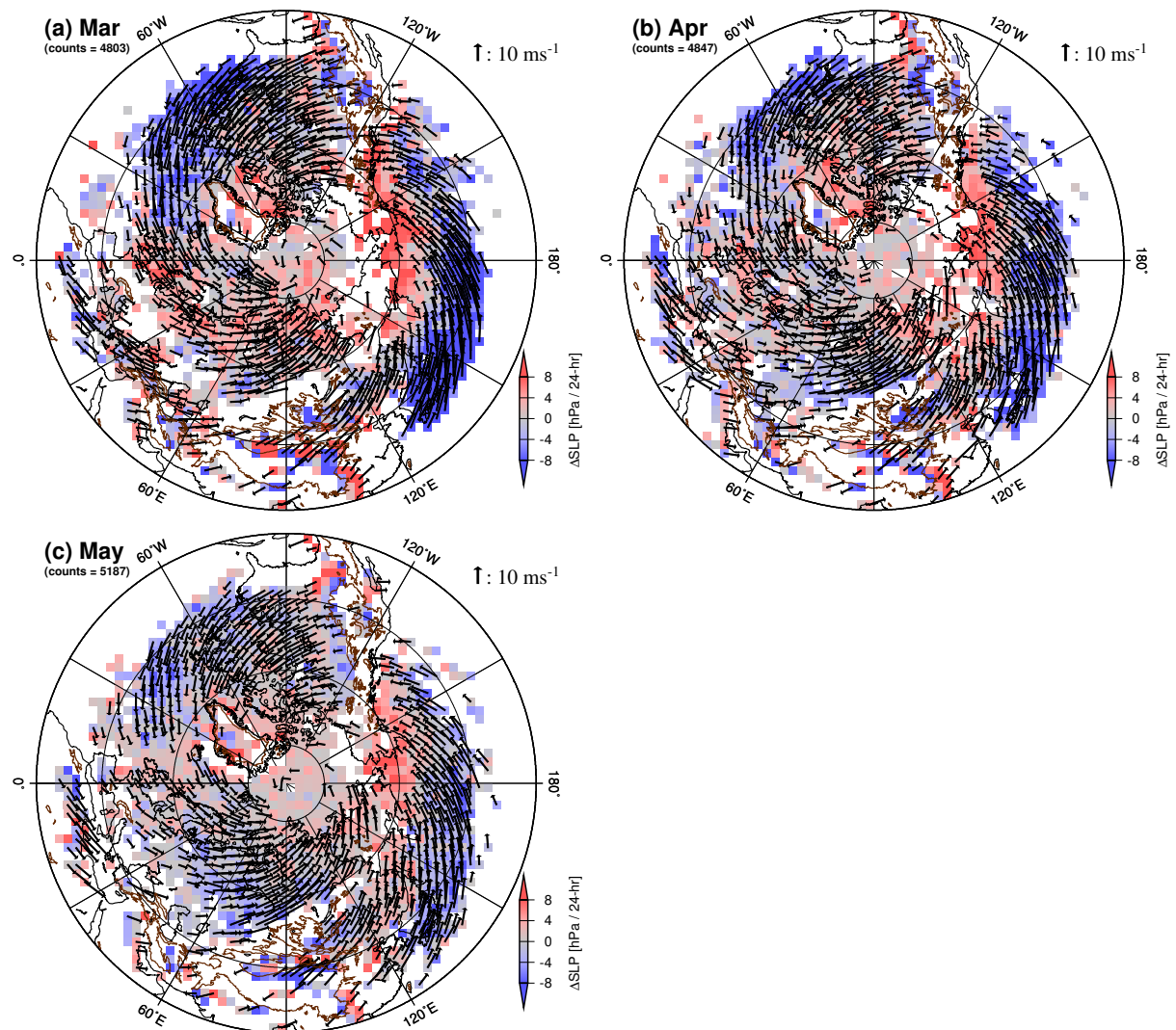


Fig. 3.7. Monthly climatologies of cyclone activities for 1972–2002 spring. Shaded area represent averaged development rate of cyclones. Vectors show mean moving vector of cyclones. The strength and position of cyclones are obtained from SLP field based on the NCEP–NCAR reanalysis data. See Serreze et al. (1997).

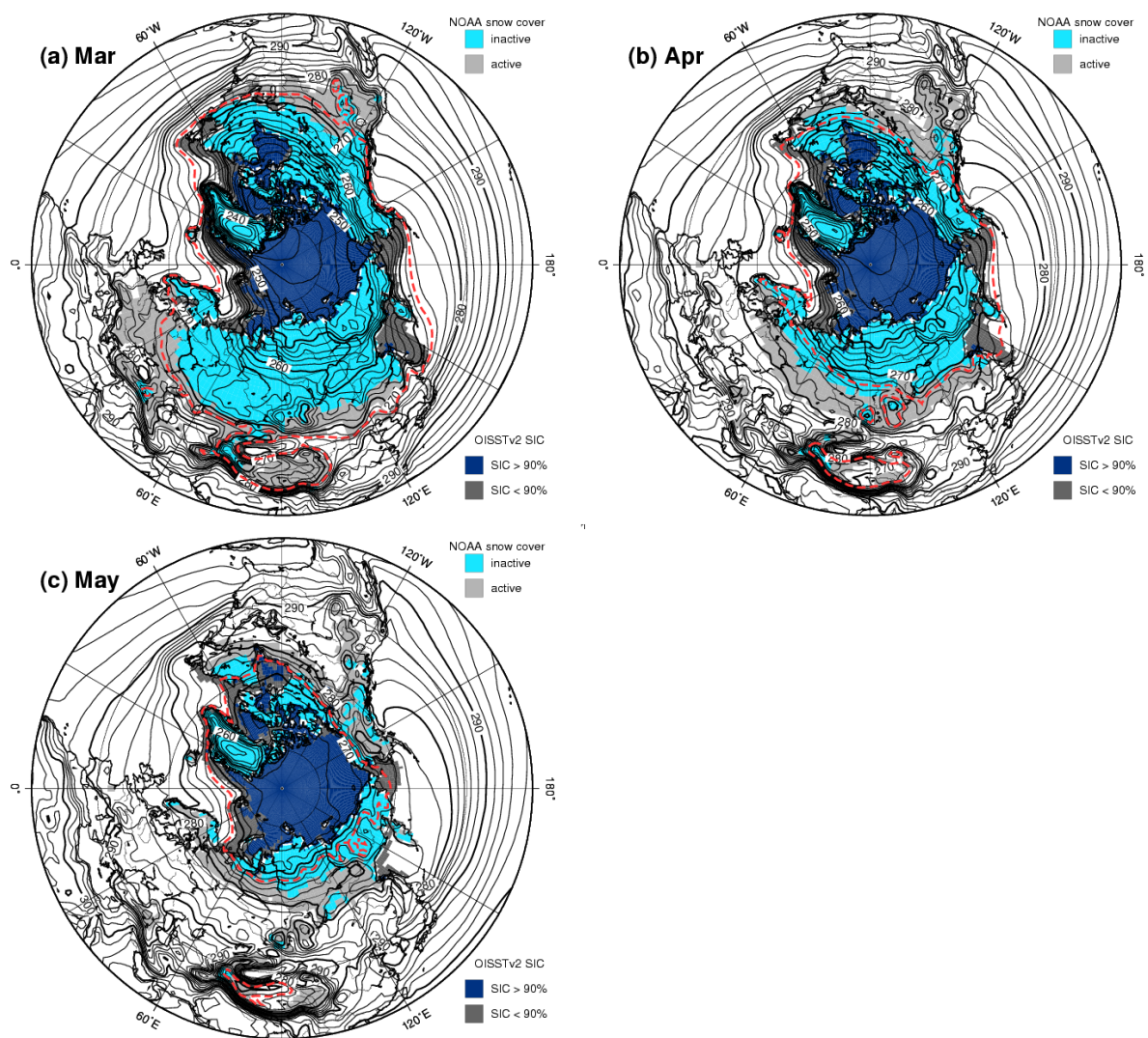


Fig. 3.8. Monthly climatologies of snow cover and sea ice concentration (SIC) for spring season. Light blue show “invariant” snow cover areas defined by the snow cover probability above 90%. Light gray represent “variant” snow cover areas defined by the snow cover probability ranging from 10 to 90%. Dark blue and dark gray also indicate “invariant” and “variant” areas, respectively, for SIC. Solid line show monthly climatologies of surface air temperature. Red dashed lines correspond to 0°C.

Chapter 4

Interannual variation of cold frontal activity in Mongolia

4.1 Seasonal mean analyses of cold frontal activity in Mongolia

As shown in Fig. 3.1, eastern Mongolia and Inner Mongolia in China show high frequency of cooling days f_{cd} throughout the year. This area also corresponds to a region of major dust storm occurrence (Sun et al. 2001; Kurosaki and Mikami 2003; see also Fig. 1.16). For these reasons, the analysis in the following section focuses on eastern Mongolia (between $39.375^\circ - 50.625^\circ\text{N}$ and $102.375^\circ - 120.375^\circ\text{E}$, enclosed by the dashed rectangle in Fig. 3.1). Interannual variations in frequency of cooling days in Mongolia are evaluated by the area-averaged frequency of cooling days $[f_{cd}]$, which is proportional to the sum of the total cooling days within the analysis area.

The seasonal mean $[f_{cd}]$ in Mongolia for 1957 through 2002 in summer, autumn, winter, and spring are shown in Fig. 4.1. Large circles and squares represent the 8 highest and 8 lowest $[f_{cd}]$ values for the period 1972–2002, respectively. Note that for the spring observations, the years with the highest $[f_{cd}]$ values are identified in the first half of the 1972 to 2002 period, whereas the years with the lowest $[f_{cd}]$ values are observed after the mid 1980s. This is consistent with the trend toward decreasing frequency of cold air outbreaks in Mongolia and northern China (Zhai et al. 1999) and the weakening of cyclone activity over Mongolia (Qian et al. 2002). The interannual variation is not as

obvious in summer, autumn, and winter as in spring.

As noted in Section 3.1.1, $[f_{cd}]$ is determined by the total cooling days for all grid points in the analysis area divided by the total number of days. Therefore, any variation in springtime $[f_{cd}]$ is expected to be caused by one or more of the following factors: (1) geographical differences in the cold air pathways, (2) differences in cooling intensity during the cooling period, and (3) temporal changes in the passage of the cold air.

In order to identify the dominant factor(s) in the differences of $[f_{cd}]$, we examined composites of the 8 years with highest $[f_{cd}]$ values for spring of 1972 through 2002 (active years) and the 8 years with lowest values (inactive years). The years used in these composites are marked with circles and squares in Fig. 4.1d and listed in Table 4.1.

4.1.1 Spatial pattern in frequencies of cooling days

Figure 4.2 shows the geographical distributions of f_{cd} based on the composites. The peak frequency of cooling days over Mongolia is distinctly smaller in the inactive years (Fig. 4.2b) (about 0.09 day^{-1}) than that in the active years (Fig. 4.2a) (about 0.14 day^{-1}). Although the difference in frequency of cooling days is remarkable, there is no obvious difference between the composites of active and inactive years with regard to the geographical location of the frequency maxima. This suggests that the difference in $[f_{cd}]$ between the active and inactive years in Mongolia does not depend on the spatial changes in cold front pathways.

4.1.2 Statistics of cold frontal activity

In this section, we examine the cooling intensity and the frequency of cold frontal passages over Mongolia. Recall that the identified cooling days are determined by using constant threshold value ($\Delta T_r = -5 \text{ K}$). Based on this definition, it could fail to detect a weak cold frontal system which has smaller temperature gradient. In order to assess the changes in a temporal cycle of cold frontal passages, it is necessary to count the total number of cold frontal passages, including weak ones, over Mongolia. As shown in Fig. 2.4, the

propagation of cold front provides region-wide strong cooling behind the front. Therefore, a period for a cold frontal passage (cooling period hereafter) is simply determined by a negative value of the area-averaged daily-mean temperature change in the analysis area ($[\Delta T(t)] = [T(t)] - [T(t-1)]$). A single cooling event is identified by the successive cooling period ($[\Delta T] < 0$). The total cooling period in each season is obtained from the sum of the number of cooling period during the season. The key date of a cooling event (Day 0) is defined by the day of the maximum temperature cooling during a cooling period. To evaluate the intensity of cooling event, we examined two indices obtained from area-averaged temperature changes. One is the total temperature change during a cooling period ($[\Delta T_{total}]$), and the other is the temperature change at Day 0 ($[\Delta T_0]$).

On the basis of these definitions, cooling events occurred in an average of about 19 times in spring, which corresponds to once per 4.7 days. The cooling event defined above includes most of the identified cooling days in each grid cell within the analysis area. Indeed, the cooling period defined by $[\Delta T] < 0$ includes 98% of the total number of cooling day that is identified by daily mean temperature differences at each grid.

Table 4.2 shows the results of these statistics for the 8 year composites of active and inactive years. As expected, the mean $[f_{cd}]$ difference between the two composites is quite large, with a ratio of the difference to the climatology reaching about 40%. The differences in $[\Delta T_{total}]$ and $[\Delta T_0]$ are approximately 20%. In contrast, the differences in the mean number of cooling events and the mean cooling period are quite small (smaller than 4% to the climatology). These results suggest that the recent decrease in $[f_{cd}]$ substantially depends on the weakening of cooling intensity in the analysis area.

Furthermore, the mean difference of $[\Delta T_0]$ between the composites of the active and inactive years (0.67 K) amounts to 70% of the mean difference in $[\Delta T_{total}]$ (0.91 K). Since $[\Delta T_0]$ is determined by the maximum temperature drop in each cooling period, $[\Delta T_0]$ corresponds to the horizontal temperature difference across the cold front. Therefore, the weakening of $[f_{cd}]$ in recent years is closely related to the weakening of the horizontal

temperature gradient across the cold front.

However, as noted in Chapter 3, atmospheric circulation pattern and surface conditions over land area have greatly changed with season evolved. For example, the existence of snow cover affects temperature field through a snow-albedo feedback (Groisman et al. 1994b). The location of snow line over Eurasia shifts northward in several thousand kilometers from March to May (Shinoda et al. 2001; Ueda et al. 2003). To consider physical processes in differences of cold frontal activities, it is necessary to evaluate meteorological conditions with a higher temporal resolution than seasonal mean. Following the reasons mentioned above, we examine composite analyses using meteorological variables related to the difference of cold frontal activity (CFA) (e.g., temperature, cyclone activity, and snow cover) based on monthly mean data in spring.

4.2 Monthly mean analyses of cold frontal activity in Mongolia in spring

4.2.1 Interannual variation of cold frontal activity

Table 4.3 shows monthly mean anomalies of $[f_{cd}]$ for the active and inactive years of the seasonal mean $[f_{cd}]$ in spring. Monthly anomalies are derived from deviation from climatological-mean for the period 1972–2002. The averaged $\Delta[f_{cd}]$ in each months for the active and inactive years show same sense of the seasonal mean anomaly of $[f_{cd}]$. However, all of the months in the active and inactive years do not show same sense of the seasonal mean anomaly of $[f_{cd}]$. For example, three of eight years in the inactive years have positive anomalies in April 1984, 1992, and 2002.

Interannual variation of monthly mean anomaly of $[f_{cd}]$ in spring is shown in Fig. 4.3. In May, negative anomalies of $[f_{cd}]$ are frequently observed in recent two decades (Fig. 4.3c). Linear trend of monthly mean $[f_{cd}]$ for the period 1972–2002 indicates that the negative trend in May is statistically significant. On the other hand, the trend is not significant in March and April.

4.2.2 Spatial pattern in frequencies of cooling days

In this section, composite analyses are based on the monthly mean anomalies of $[f_{cd}]$ during the period 1972–2002 (Fig. 4.3). The spatial distribution of cooling day frequency in each month is shown in Figs. 4.4, 4.5, and 4.6.

(a) March

Figure 4.4 shows the spatial distribution for f_{cd} in March. As same as the long-term mean field (Fig. 3.4a), there are two maximum areas of f_{cd} in the West Siberian Plain and eastern Mongolia. In the active years (Fig. 4.4a), the frequency in these two areas shows nearly comparable values. In contrast, cooling day frequency in eastern Mongolia for the inactive years is quite small compared with that in the West Siberian Plain (Fig. 4.4b).

(b) April

In April (Fig. 4.5), the mean frequency for active years is somewhat larger than the frequency of long-term mean (see Fig. 3.4b). The two primary axes of f_{cd} are identified in Fig. 4.5a. One is the east-west elongated area extending from the West Siberian Plain to the west of Lena River in north of 60°N . The other one is the northwest-southeast elongated area originated from the west of Lake Baikal through the leaside of Altai-Sayan Mountains to the eastern Mongolia and Inner Mongolia in China (Fig. 4.5a).

In the composite of inactive years, although the northern part of cold frontal activity slightly shifts poleward, these two primary axes of $[f_{cd}]$ are also identified (Fig. 4.5b). The local maximum of f_{cd} in the north of Tianshan Mountains for the inactive years is easily distinguished from the active areas in high-latitudes. In general, the largest frequency areas for the inactive years tend to separate into two latitudinal zones, one is located along the coast of the Arctic Ocean and the other one elongates in mid-latitude area between 40° and 50°N .

(c) May

In May (Fig. 4.6), it is similar to the long-term mean fields shown in Fig. 3.4c, two areas for the largest frequency of cooling days can be found in the southern part of West Siberian Plain and eastern Mongolia. Although the largest frequency of Fig. 4.6b in eastern Mongolia is quite small compared with Fig. 4.6a, the maximum frequent area still located within the analysis area. However, there are differences in its spatial extent in meridional direction between these two composites. In the active years (Fig. 4.6a), cooling days are rarely observed in the Far East Siberia to the east of the Lena River between 60° and 70°N . In contrast, cooling days for the inactive years are observed to the east of the Lena River and are rarely observed in the southeastern China (east of the Tibetan Plateau in south of 35°N in mainland China) (Fig. 4.6b).

4.2.3 Statistics of cold frontal activity

To examine the activity of cooling events compared between active and inactive years, composite analyses are required with respect to the intensity and temporal cycle of cooling event. Computed variables in this evaluation are completely same as shown in section 4.1.2, but calculated by using monthly data.

Calculated monthly statistics are summarized in Table 4.5. As expected, composite of $[f_{cd}]$ shows that $[f_{cd}]$ for the active years are twice or three times larger than that for the inactive years in each month. As same as Section 4.1.2, it is clear that the mean number of cooling events between active and inactive years is approximately same in March and May. In April, although the mean number of events for the active composite is slightly larger than that for the inactive composite, it is not enough to explain the differences between these two composite.

On the other hand, there are quite large differences in the cooling intensity for all months. For example, the mean cooling intensity for the total cooling period (ΔT_{total}) in the active composite is much larger than that in the inactive composite. The ratio of

ΔT_0 of the active to the inactive composite ranges from 1.3 to 1.8 in spring season. These differences of ΔT_{total} are primary due to the differences in the cooling at Day 0 (ΔT_0). The contribution ratio of ΔT_0 to ΔT_{total} is very large such as the ratio reaches to 64% in March, 69% in April, and 74% in May. As shown in section 2.3, the cooling intensity at Day 0 (ΔT_0) is approximately proportional to the horizontal temperature gradient across a cold front (see Fig. 2.7). These results suggest that the recent decrease in CFA is primarily influenced by the weakening of cold front.

In particular, as shown in Fig. 4.3c, monthly mean CFA during 1972–2002 shows a significant negative trend in May. Additionally, the difference in the cooling intensity between the active and the inactive composite is largest in May. Consequently, to understand the springtime decrease trend in CFA, it is necessary to explore the physical process(es) for decreasing in the cooling intensity in May. In order to clarify this issue, monthly composite analyses will be examined several meteorological conditions related to the changes of cooling intensity.

Table 4.1. List of years for composite analysis over Mongolia in 1972–2002 spring (MAM).

Active		Inactive	
year	$[f_{cd}]$ (day^{-1})	year	$[f_{cd}]$ (day^{-1})
2001	0.1158	1992	0.0620
1977	0.1105	1996	0.0666
1980	0.1020	2002	0.0671
1982	0.1014	1984	0.0686
1985	0.1003	1986	0.0699
1987	0.0990	1993	0.0737
1978	0.0983	1997	0.0760
1983	0.0947	1975	0.0789

Table 4.2. Seasonal mean statistics for cooling activity in the 8-year composites of active and inactive years over Mongolia in spring (MAM).

8-year composites in spring	$[f_{cd}]$ (day^{-1})	Number of cooling events	Period (day)	$[\Delta T_{total}]$ (K)	$[\Delta T_0]$ (K)
Active	0.103	19.8	39.9	−4.44	−2.96
Inactive	0.070	18.8	37.1	−3.61	−2.50
mean	0.088	19.4	38.4	−4.04	−2.76

Table 4.3. Monthly mean anomaly of CFA over Mongolia. Ratio of each anomaly to the monthly climatologies are also depicted in parentheses. Selected years are same as Table 4.2

Active years						
climatology	Mar 0.0633		Apr 0.1040		May 0.1000	
year	$\Delta[f_{cd}]$	(ratio)	$\Delta[f_{cd}]$	(ratio)	$\Delta[f_{cd}]$	(ratio)
2001	0.0428	(+67.7)	0.0338	(+32.5)	0.0042	(+4.2)
1977	0.0433	(+68.5)	0.0167	(+16.0)	0.0046	(+4.6)
1980	-0.0013	(-2.1)	-0.0026	(-2.5)	0.0427	(+42.7)
1982	0.0335	(+53.0)	0.0021	(+2.0)	0.0015	(+1.5)
1985	0.0182	(+28.7)	-0.0167	(-16.0)	0.0318	(+31.8)
1987	0.0485	(+76.7)	-0.0067	(-6.4)	-0.0122	(-12.2)
1978	0.0109	(+17.3)	0.0113	(+10.9)	0.0061	(+6.1)
1983	-0.0229	(-36.2)	0.0518	(+49.8)	-0.0099	(-9.9)
mean	0.0216	(+34.1)	0.0112	(+10.8)	0.0086	(+8.6)

Inactive years						
climatology	Mar 0.0633		Apr 0.1040		May 0.1000	
year	$\Delta[f_{cd}]$	(ratio)	$\Delta[f_{cd}]$	(ratio)	$\Delta[f_{cd}]$	(ratio)
1992	-0.0448	(-70.8)	0.0288	(+27.7)	-0.0629	(-62.9)
1996	-0.0025	(-4.0)	-0.0345	(-33.1)	-0.0305	(-30.5)
2002	-0.0143	(-22.6)	0.0010	(+1.0)	-0.0515	(-51.5)
1984	-0.0436	(-68.9)	0.0242	(+23.2)	-0.0399	(-39.9)
1986	-0.0158	(-25.0)	-0.0161	(-15.5)	-0.0251	(-25.1)
1993	-0.0498	(-78.7)	-0.0199	(-19.1)	0.0239	(+23.9)
1997	-0.0170	(-26.9)	-0.0300	(-28.9)	0.0078	(+7.9)
1975	0.0071	(+11.3)	-0.0170	(-16.4)	-0.0204	(-20.4)
mean	-0.0226	(-35.7)	-0.0079	(-7.6)	-0.0248	(-24.8)

Table 4.4. List of years for the composite analyses based on monthly mean cold frontal activities over Mongolia in spring.

	Active			Inactive		
	March	April	May	March	April	May
1	1977	1977	1974	1976	1974	1975
2	1982	1983	1976	1983	1976	1984
3	1985	1984	1979	1984	1979	1986
4	1987	1988	1980	1988	1991	1988
5	1995	1990	1981	1990	1993	1992
6	1998	1992	1985	1992	1996	1996
7	1999	2000	1993	1993	1997	1999
8	2001	2001	1994	2000	1998	2002

Table 4.5. Monthly mean statistics for CFA in the 8-year composites of active and inactive years over Mongolia. Selected years are listed in Table 4.4.

8-year composites	$[f_{cd}]$ (day^{-1})	Number of cooling events	Period (day)	$[\Delta T_{total}]$ (K)	$[\Delta T_0]$ (K)
March					
Active	0.093	6.5	13.3	-4.43	-2.98
Inactive	0.033	6.8	12.3	-2.46	-1.71
mean	0.061	6.6	13.0	-3.42	-2.29
April					
Active	0.135	6.8	12.8	-5.09	-3.56
Inactive	0.078	5.8	11.5	-3.96	-2.78
mean	0.104	6.4	12.1	-4.40	-3.08
May					
Active	0.130	6.8	14.1	-5.01	-3.42
Inactive	0.065	6.5	13.0	-2.84	-1.81
mean	0.099	6.6	13.7	-4.18	-2.76

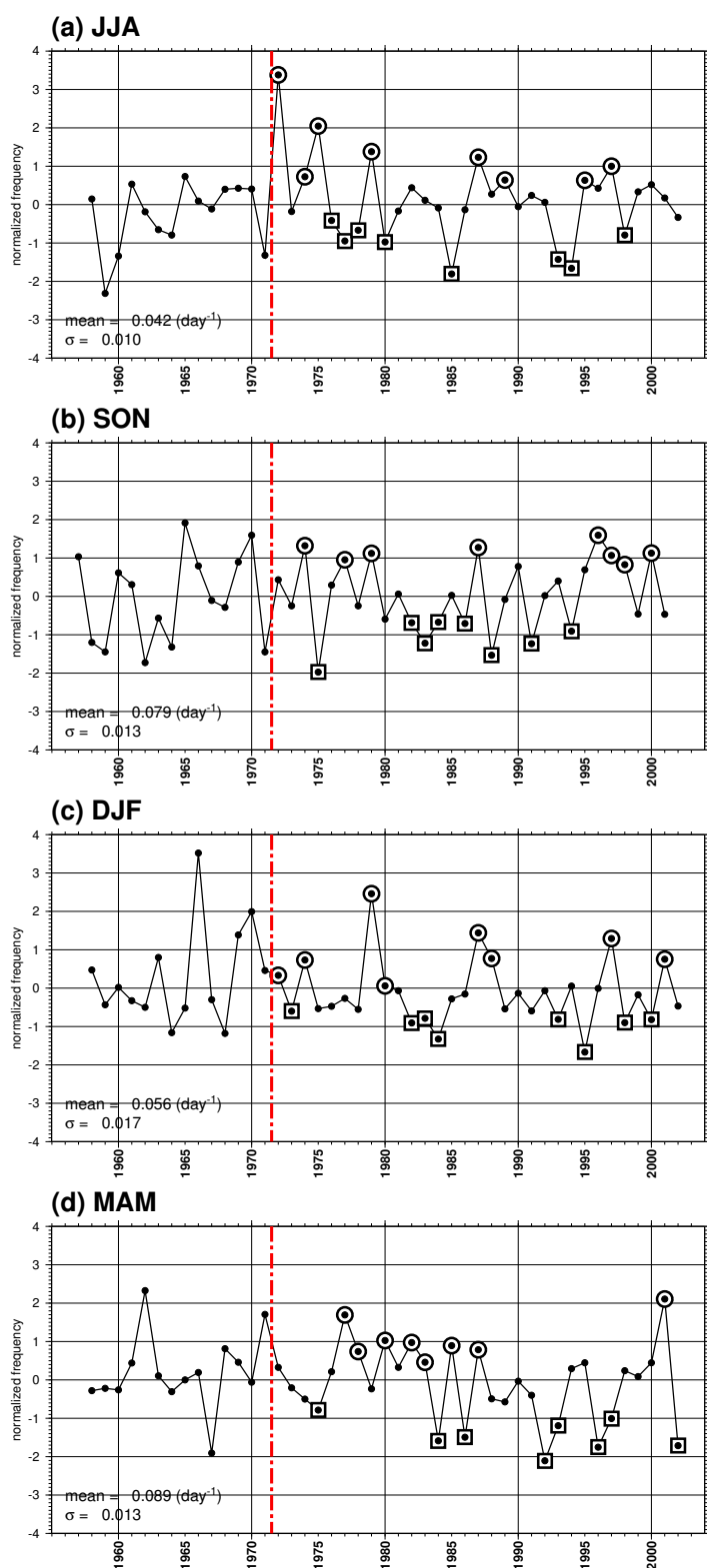


Fig. 4.1. Area-averaged cooling day frequency anomaly for 1957–2002 over Mongolia in each season. The timeseries is normalized by the standard deviation of seasonal mean anomaly of $[f_{cd}]$ during 1957–2002. (a) summer (JJA), (b) autumn (SON), (c) winter (DJF), and (d) spring (MAM), respectively. Large circles and squares represent the highest and lowest 8 years for the period 1972–2002.

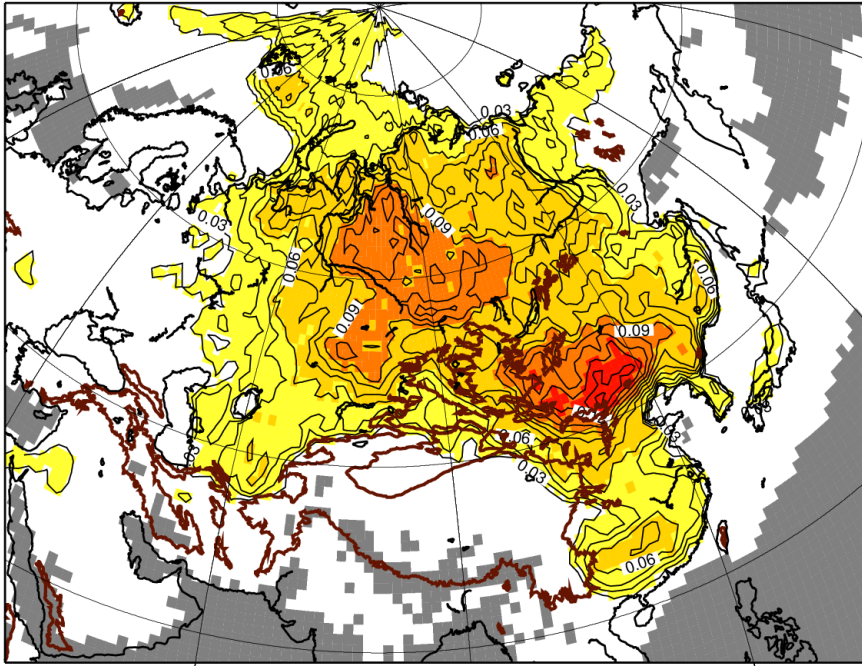
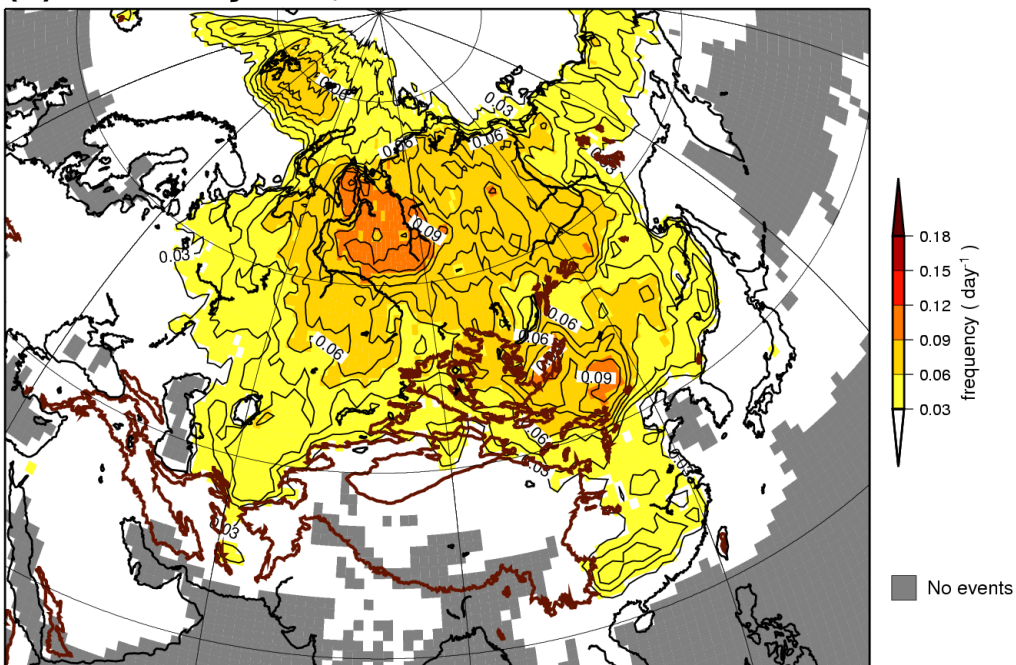
(a) Active years, MAM**(b) Inactive years, MAM**

Fig. 4.2. Spatial distributions in seasonal mean frequencies of cooling day for 8-year composites in spring. (a) active years (marked with circles in Fig. 4.1d) and (b) inactive years (marked with squares in Fig. 4.1d).

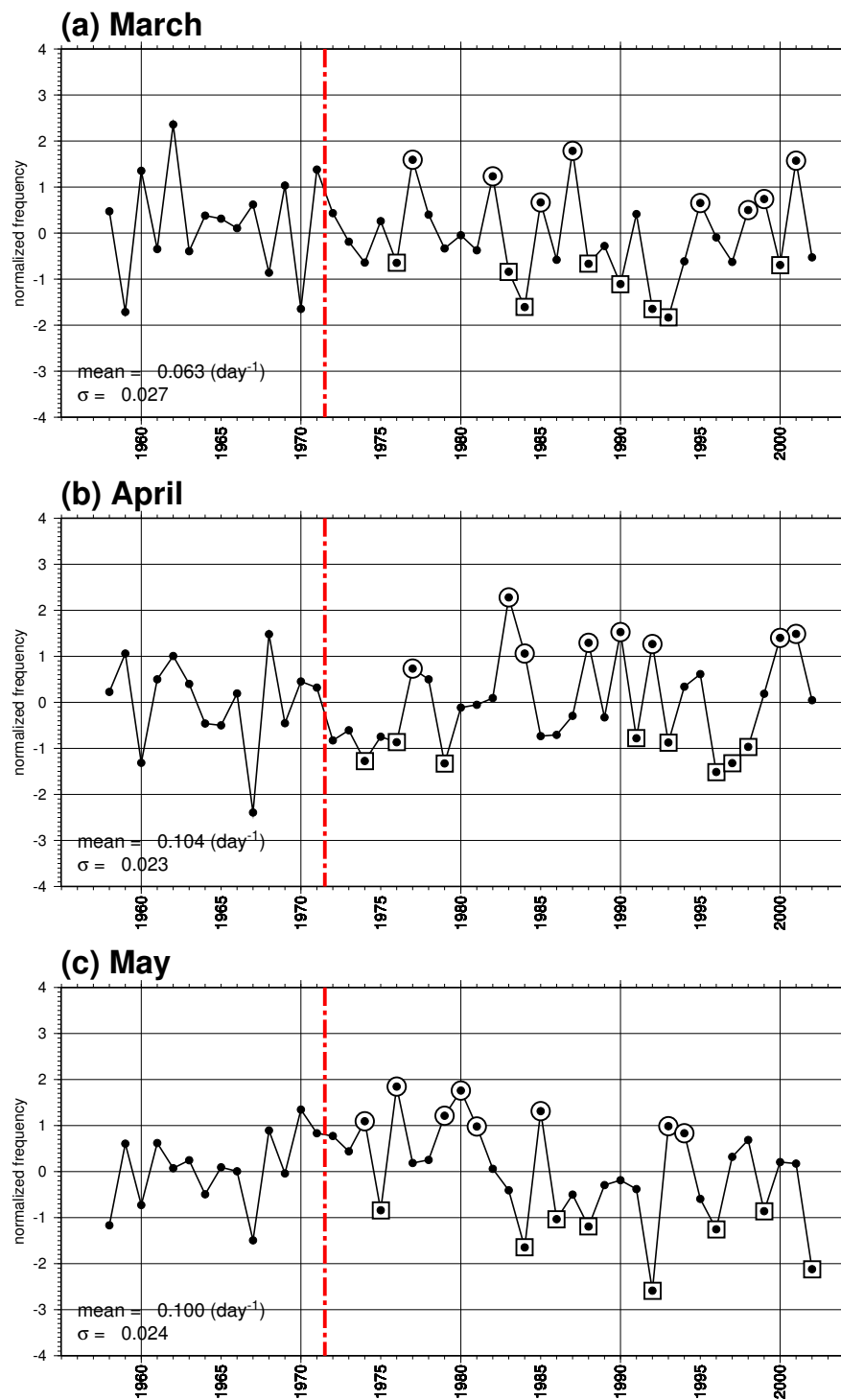


Fig. 4.3. Area-averaged cooling day frequency anomaly for 1958–2002 over Mongolia in spring months. The timeseries is normalized by the standard deviation of monthly mean anomaly of $[f_{cd}]$ during 1958–2002. (a) March, (b) April, and (c) May, respectively. Large circles and squares represent the highest and lowest 8 years for 1972–2002.

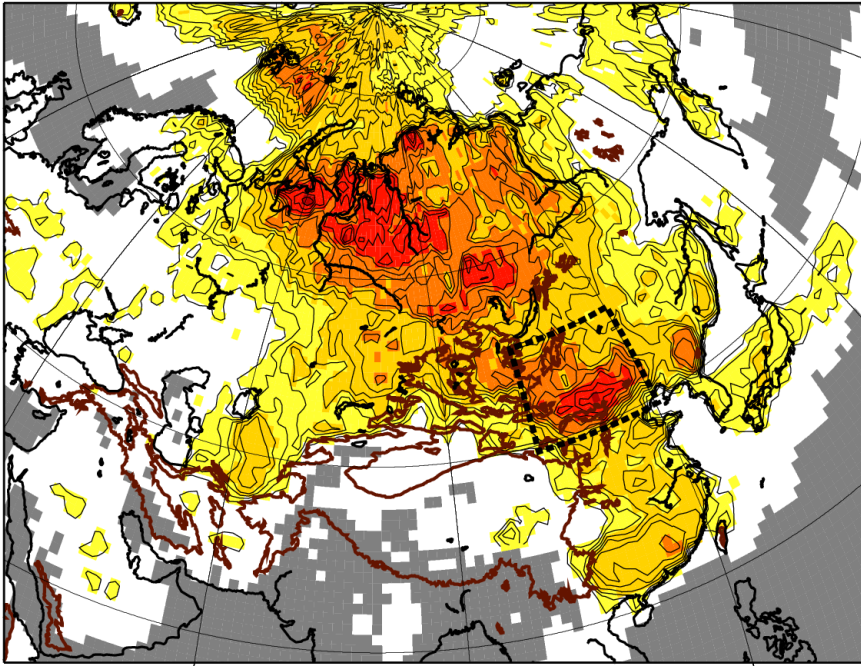
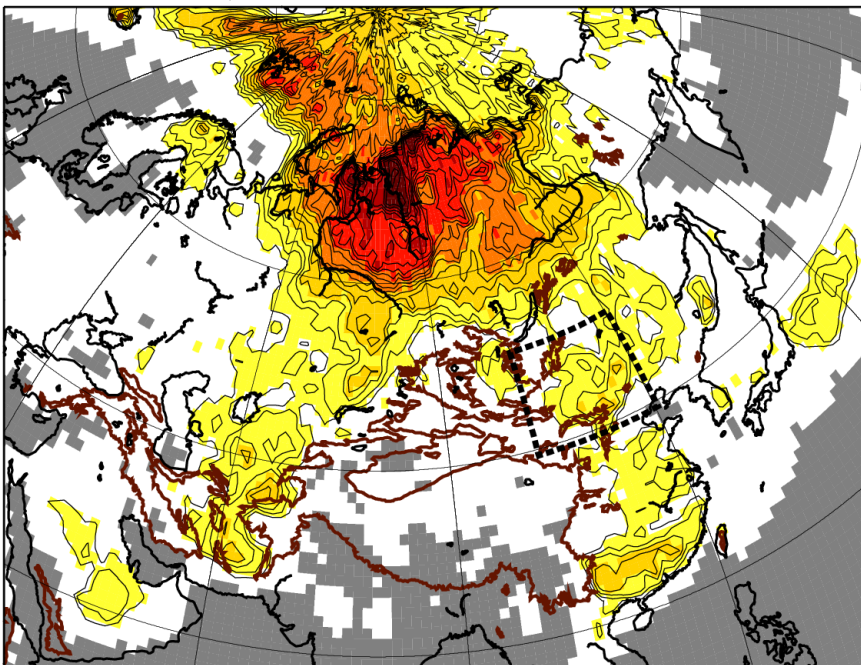
(a) Active years, March**(b) Inactive years, March**

Fig. 4.4. Spatial distributions in frequencies of cooling day for 8-year composites in March. (a) active years (marked with circles in Fig. 4.3a) and (b) inactive years (marked with squares in Fig. 4.3a).

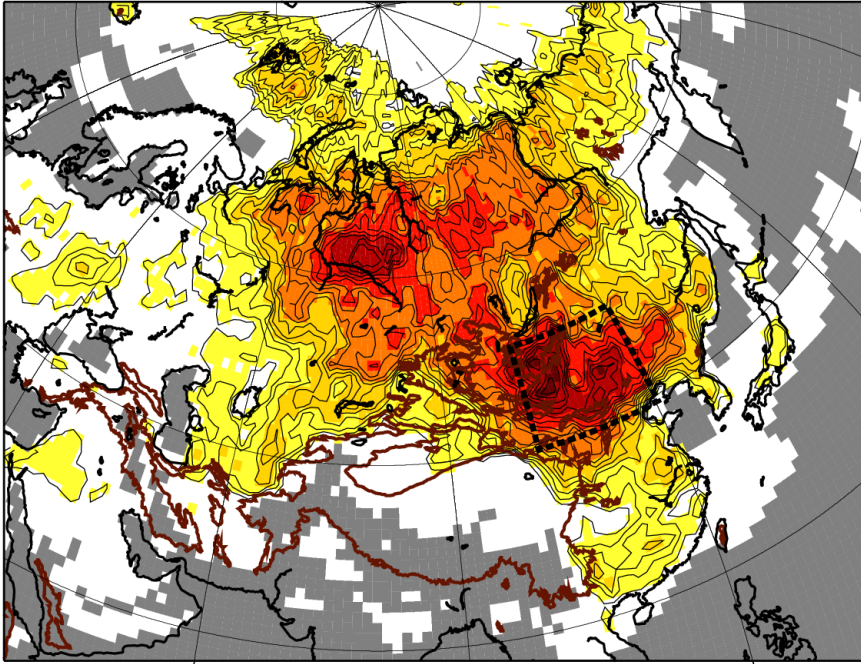
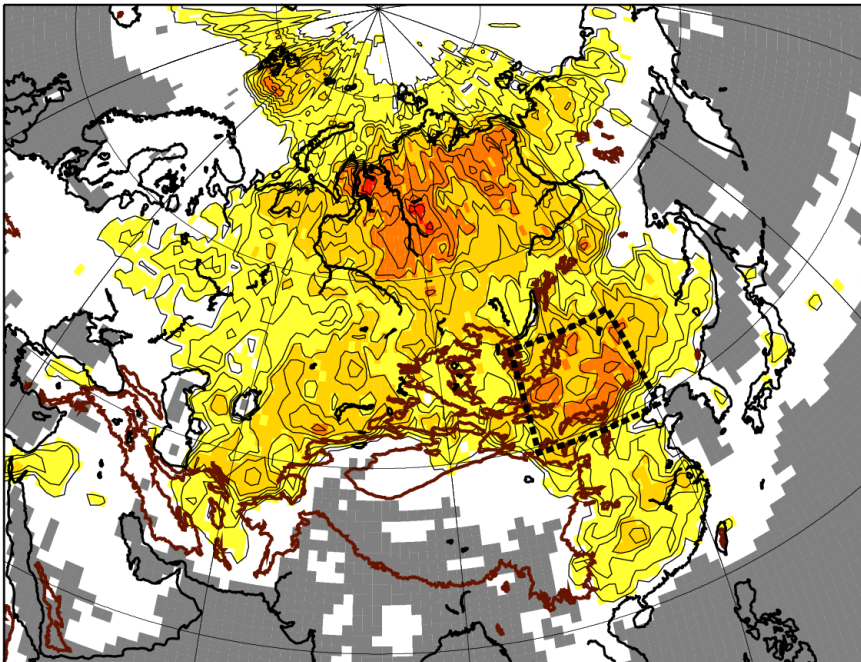
(a) Active years, April**(b) Inactive years, April**

Fig. 4.5. Same as Fig. 4.4 except for April. (a) active years (marked with circles in Fig. 4.3b) and (b) inactive years (marked with squares in Fig. 4.3b).

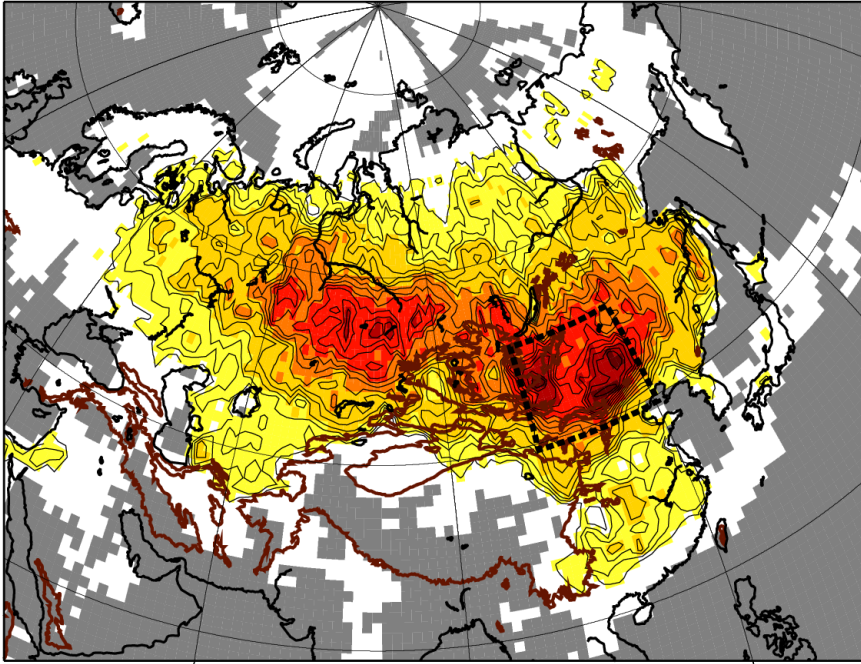
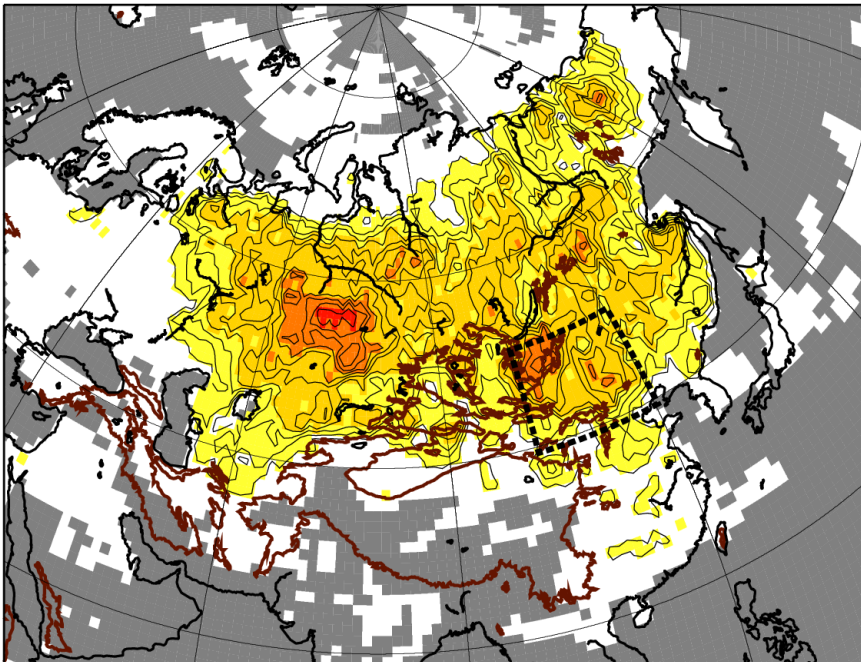
(a) Active years, May**(b) Inactive years, May**

Fig. 4.6. Same as Fig. 4.4 except for May. (a) active years (marked with circles in Fig. 4.3c) and (b) inactive years (marked with squares in Fig. 4.3c).

Chapter 5

Relationships between reduction of cold frontal activity and meteorological conditions

As discussed in the previous chapter, the cold frontal activity (CFA) over Mongolia has been decreasing in spring, particularly in May. The decrease of CFA is closely related to the weakening of a cooling intensity which is assumed to regard the horizontal temperature gradient across cold front. As noted in Chapter 1, a traveling cold frontal system over Mongolia is formed in association with a cold air outbreak originated from Siberia. To show the physical process(es) of the weakening of CFA, it is required to analyze a large-scale temperature field throughout Eurasia. In addition, as discussed by earlier studies, temperature variations are greatly influenced by several atmospheric conditions such as large-scale circulation anomalies (Hurrell 1996; Thompson and Wallace 1998), tracks and/or strength of synoptic-scale eddies (Enomoto et al. 1993; Rogers and Thompson 1995), and existence of snow cover (Groisman et al. 1994b; Brown 2000; Shinoda et al. 2001; Ueda et al. 2003).

In this chapter, composite analyses are also examined in concern with above mentioned meteorological fields to show a relationships between CFA and atmospheric conditions.

5.1 Differences in temperature fields

Figure 5.1 shows the difference of temperature fields obtained by subtracting the active years from the inactive years in May extending from surface up to upper troposphere (300-hPa). Positive anomalies with statistical significance extends southeastward from Barents Sea to northern Mongolia and northeastern China below 500-hPa (Figs. 5.1a–d). Directions of the largest axis of positive anomalies in Figs. 5.1a–d are somewhat different in the axis of the highest frequency of cooling day (see Fig. 3.4c). However, as noted in Section 3.1.1, a cold air observed in eastern Mongolia originate from northern part of the West Siberian Plain or north of Central Siberian Upland in May. Hence, the axis of the largest positive anomalies also corresponds to the pathway of cold air.

Additionally, the spatial pattern of the largest positive anomalies is quite similar to the distribution of the warming trend (see Fig. 1.2). These results suggest that the weakening of cooling intensity in Mongolia is related to the warming in the source area of cold air.

5.2 Differences in snow cover condition and upper-level circulation

As discussed by earlier studies, springtime temperature field is largely influenced by the snow cover anomaly (e.g., Groisman et al. 1994a; Groisman et al. 1994b) or circulation anomalies such as the North Atlantic Oscillation (NAO) (e.g., Hurrell 1996) or the Arctic Oscillation (AO) (e.g., Thompson and Wallace 1998; Thompson et al. 2000).

5.2.1 Snow cover

One of the most important variables in considering the recent warming trend is the snow cover. According to Groisman et al. (1994a), the presence or absence of snow cover affects the local radiation balance through the snow-albedo feedback particularly in April and May.

To describe a relationship between CFA and snow cover, composite analysis of snow

cover for the active and inactive years is shown in Fig. 5.2. The 8-yr composite of snow cover is represented by the probability of snow cover in each grid cell ($0 < SC(i) < 1$, i is a grid indicator) for the active and inactive composites. The difference of the snow cover probability ($\Delta SC(i)$) is obtained by subtracting the probability for the active years ($SC(i)_{active}$) from the probability for the inactive years ($SC(i)_{inactive}$).

In mid-May, as shown in Fig. 3.8c, snow cover is always covered along the northern coastal Eurasia to the north of 65°N . The “variant region” of snow cover, which is defined by the probability of snow cover ranging from 10%–90% during 1972–2002, extend over the north of 60°N in the north-western Eurasia and the north of 55°N in the north-eastern Eurasia. In the active years, the probability of snow cover is larger than that of the inactive years over eastern Eurasia to the east of 90°E (Fig. 5.2). Therefore, the snow cover extent for the active years is larger than that for the inactive years in eastern Eurasia.

Since the snow cover probability ($SC(i)$) in each grid cell is obtained by the 8-yr mean of binary value (0 or 1), the different areas of snow cover probability ($\Delta SC(i)$) may be influenced by the spatial distribution in each year. To provide the reliability in terms of the differences shown in Fig. 5.2, mean timeseries of snow cover extent over eastern Eurasia (enclosed by thick dashed line in Fig. 5.2) is displayed in Fig. 5.3 during the period of mid-February (pentad number 10) through late June (pentad number 36). As expected, the significant larger snow cover extent persisted from 27 to 34 pentad for the active years. These results indicate that the negative anomalies of snow cover extent is dominant over eastern Eurasia for the inactive years of CFA.

In comparison with Figs. 5.1 and 5.2, the center of the highest positive temperature anomalies, which is located to the south of 60°N between 90° and 120°E , approximately correspond to the area of negative snow cover probability. However, it should be noted that the northern part of positive temperature anomalies is located over “invariant” snow cover region in the north of the West Siberian Plain and the Central Siberian Upland. In

the south of the Lena River to the south of 60°N , although the snow cover probability is small, temperature anomalies are not large compared to the west of 120°E . The presence or absence of snow cover largely influenced to the near-surface temperature through the snow-albedo feedback (Groisman et al. 1994b; Groisman et al. 1994a). The composite results in Figs. 5.1 and 5.2 suggest that it is necessary to consider other physical process(es) affecting the temperature field in addition to the local heating anomalies depending on the existence of snow cover. As discussed by earlier studies (Curry 1983; Curry 1987; Groisman et al. 1994b), it is important to contribute for the heat balance in the cryosphere considering not only snow-albedo feedback but horizontal advection. To describe this issue, circulation fields are also analyzed.

5.2.2 Surface and upper level circulations

Figure 5.4 illustrates differences of surface and upper level circulation field between the active and inactive years. Positive differences of sea level pressure (SLP) with statistical significance are extensively observed extending from eastern Eurasia to northwestern Pacific (Fig. 5.4a). The center of the positive SLP difference is found in the east of 100°E , southern Central Siberian Upland, northeastern China, and Sea of Okhotsk. As illustrated in Fig. 3.7, southern portion of positive SLP differences correspond to the primary cyclone tracks originated from eastern Mongolia, i.e., Mongolian cyclones. In contrast, negative SLP differences without statistical significance are dominant over the Arctic Ocean. The minimum SLP difference is located near the East Siberian Sea.

Figure 5.4b shows that the composite difference of monthly mean geopotential height at the 500-hPa level. The significant positive differences is identified from north of the West Siberian Plain (70°N , 85°E) to the eastern Mongolia and over the Sea of Okhotsk. The former positive difference area is reflected to lower tropospheric temperature anomalies below 500-hPa (Fig. 5.1).

As noted by Lau (1988), mean circulation anomaly in the middle troposphere is closely related to storm track activity. Additionally, southern portion of positive SLP differences

also correspond to the major route of the Mongolian cyclone (Fig. 3.7). The linkage between the reduction of CFA and cyclone activity will be examined in the next section.

5.3 Differences in the activity of synoptic eddies

5.3.1 Synoptic-scale eddy activity at 500-hPa level

To describe a relationship between a cold frontal activity and synoptic-eddy activity, composite of transient eddy activity computed from 2–8 day bandpass-filtered geopotential height at 500-hPa is presented in Fig. 5.5.

In the active years (Fig. 5.5a), transient eddy activity are evidently enhanced along the climatological storm track axis from northwestern Russia to northwestern Pacific, particularly over central Eurasia and over northeastern China. The highest anomalies of transient eddy activity can be found over northeastern China, corresponding to the entrance region of the Pacific storm track. In contrast, in the inactive years (Fig. 5.5b), negative anomalies can be found over north of Altai–Sayan Mountains and from the northeastern China to the Sea of Okhotsk.

Figure 5.5c shows the difference between Figs. 5.5a and 5.5b (inactive minus active). The negative differences indicate that the transient eddy activity for the inactive years is less than that for the active years. As expected from Figs. 5.5a and 5.5b, significant negative differences are dominant over central Eurasia and from northeastern China to the Sea of Okhotsk. In the center of the negative difference areas, these differences reach to approximately 50% compared to the climatological values. These results are consistent with the results by Clark and Serreze (2000).

5.3.2 Cyclone activity

As shown by Whittaker and Horn (1984), cyclones over continental Asia are frequently formed in eastern Mongolia and called as “Mongolian cyclones”. The Mongolian cyclones develop over eastern Mongolia and northeastern China and move northeastward to the

Sea of Okhotsk (see Fig. 3.7). As pointed out by Boyle and Chen (1987), the Mongolian cyclones are considered as secondary cyclones on the trailing cold fronts of occluded lows in western Siberia. Therefore, the recent weakening of cold front intensity may affect the cyclogenesis in this area. To examine the difference of cyclone activity in this area, histograms of maximum intensity for all cyclones are presented in Fig. 5.6. The maximum intensity in each cyclone is determined by the minimum SLP observed within the analysis area.

In comparison with the active and inactive years, strong cyclones are frequently observed for the active years. Focused on the strong cyclones (minimum SLP < 992-hPa), the occurrence probability of strong cyclones is 40% and 13% for the active and inactive years, respectively. These results suggest that the recent weakening of cold front intensity also produce the weak cyclones over east Asia.

5.4 Summary of the changes of meteorological conditions in association with the reduction of cold frontal activity

The results obtained from the previous sections are summarized as follows: (1) CFA [f_{cd}] in Mongolia shows a significant decreasing trend in May for the recent three decades, (2) the reduction of CFA reflects the weakening of a temperature difference across a cold front, (3) in comparison with the active and inactive years of CFA, the weaker CFA corresponds to the smaller snow cover extent in eastern Eurasia, (4) strength of cyclones generated in eastern Mongolia and northeastern China are weak for the inactive years.

Based on these results, we discuss the possible explanations of the recent decreases of CFA in May in the next chapter.

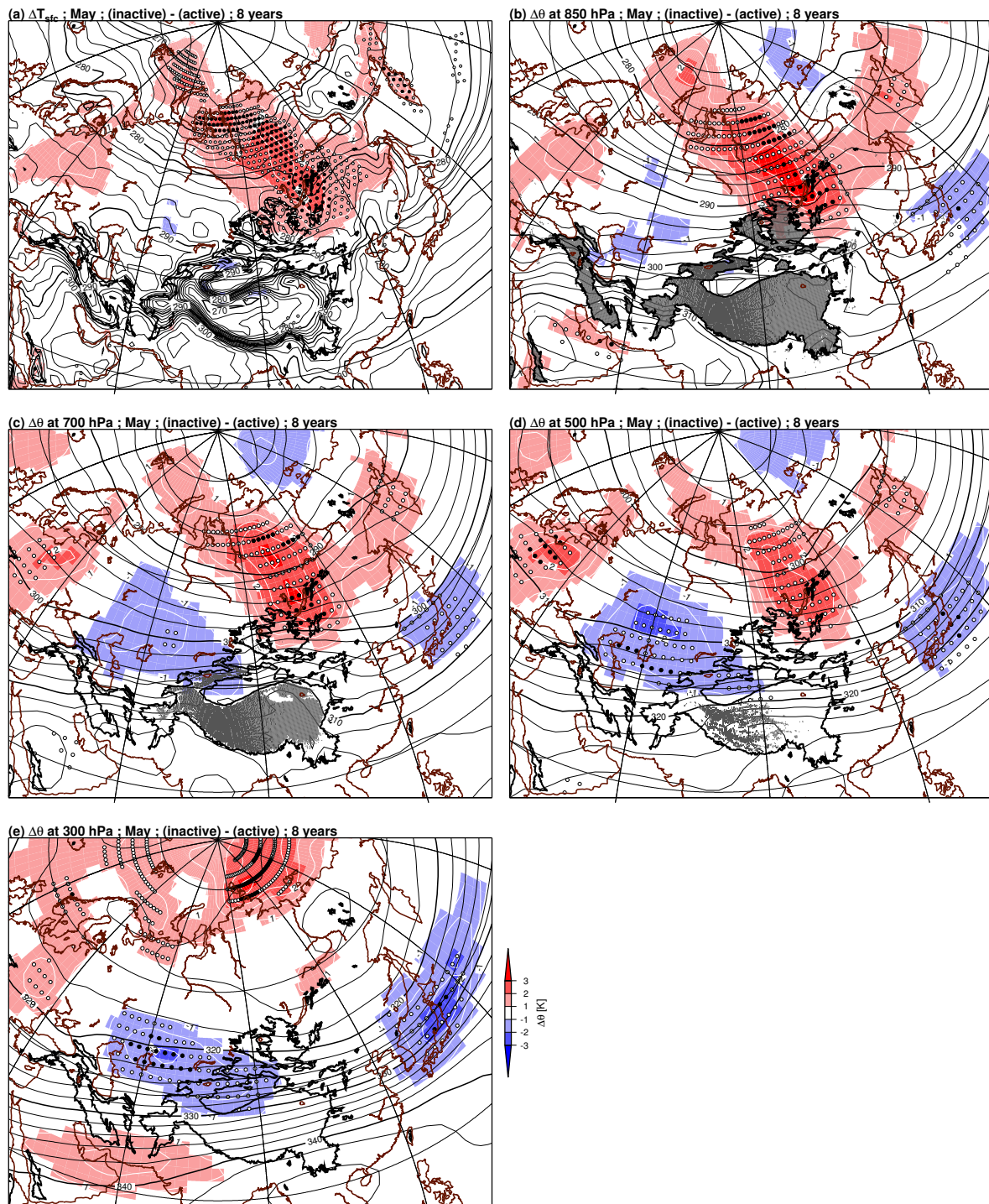


Fig. 5.1. Spatial distribution of temperature differences between the composite of active and inactive years in May. (a) ΔT_{2m} , θ at (b) 850-hPa, (c) 700-hPa, (d) 500-hPa, and (e) 300-hPa. Contour interval of temperature differences (white solid line within shaded area) is 0.5 K. Black contour (2 K interval) represent climatological-mean field for the period 1972–2002. Statistically significant differences are denoted in white and black circles at 0.05 and 0.01 significance level, respectively.

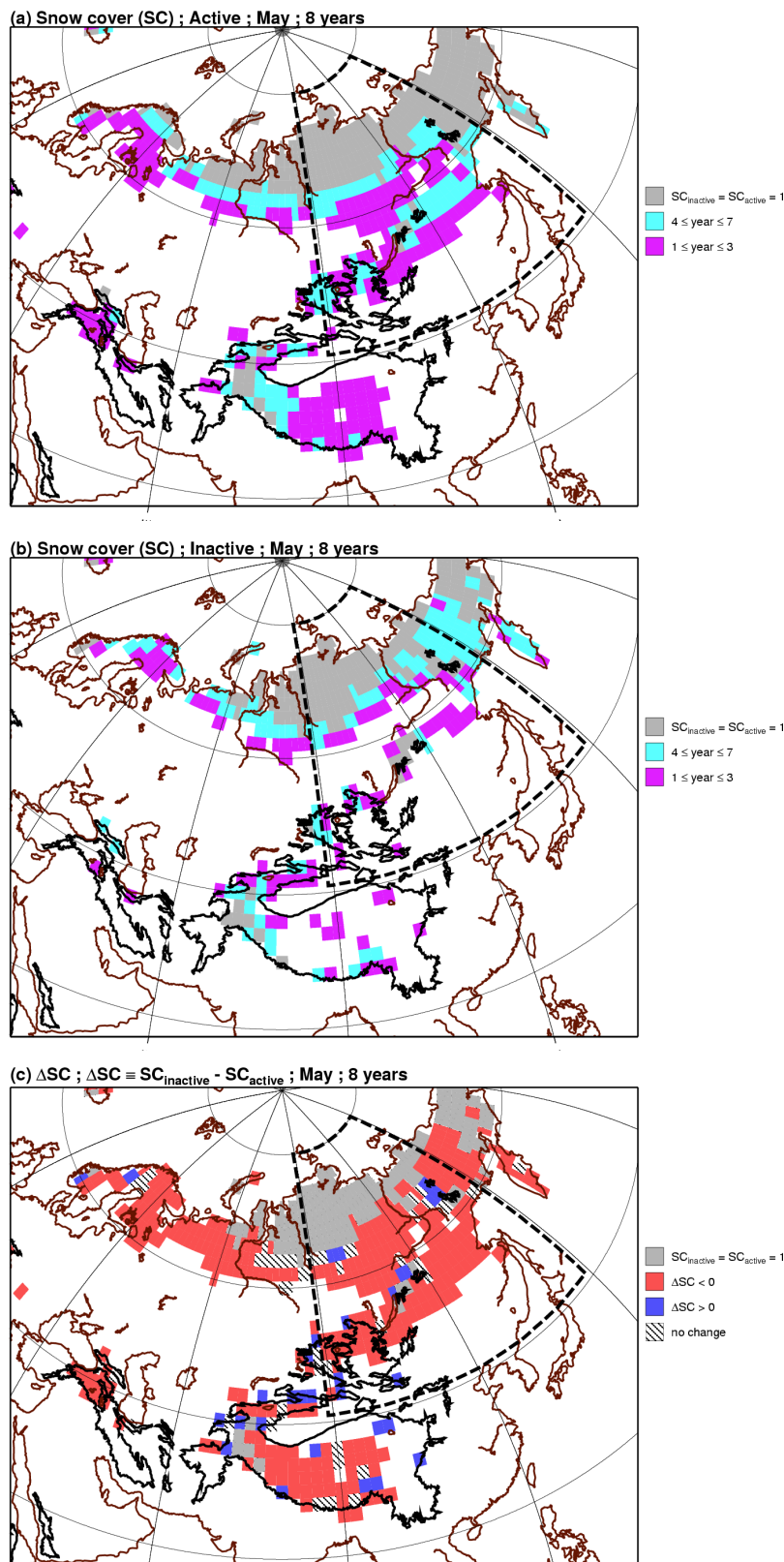


Fig. 5.2. Spatial distribution of snow cover existence in mid-May. (a) active years, (b) inactive years, and (c) b minus a. Light blue and purple area represents snow cover is observed equal or less than 3 years and larger than 3 years, respectively. Gray shaded area show that snow cover is always observed. The area for calculating total snow cover (see Fig. 5.3) is enclosed by dashed line.

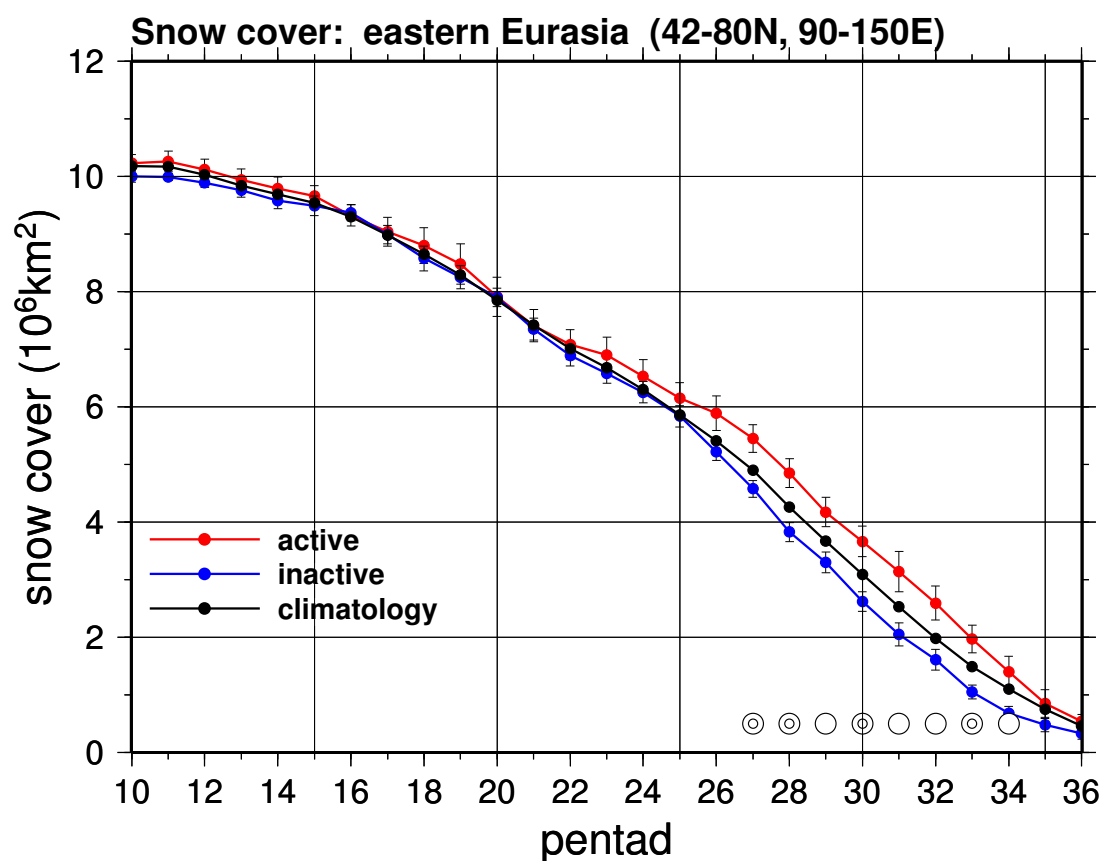


Fig. 5.3. Composite timeseries of snow cover area in eastern Eurasia (42° – 80° N, 90° – 150° E) for the pentad number 10–36 (corresponds to the period from mid February to late June). Composited years are same as Fig. 5.1. Black line show climatological-mean of snow cover area for the period 1972–2002. Red and blue line show mean snow cover area for active and inactive years, respectively. Bars with each composite indicate standard error (SE) in each pentad. Statistically significant differences are denoted in single and double circles at 0.05 and 0.01 significance level, respectively.

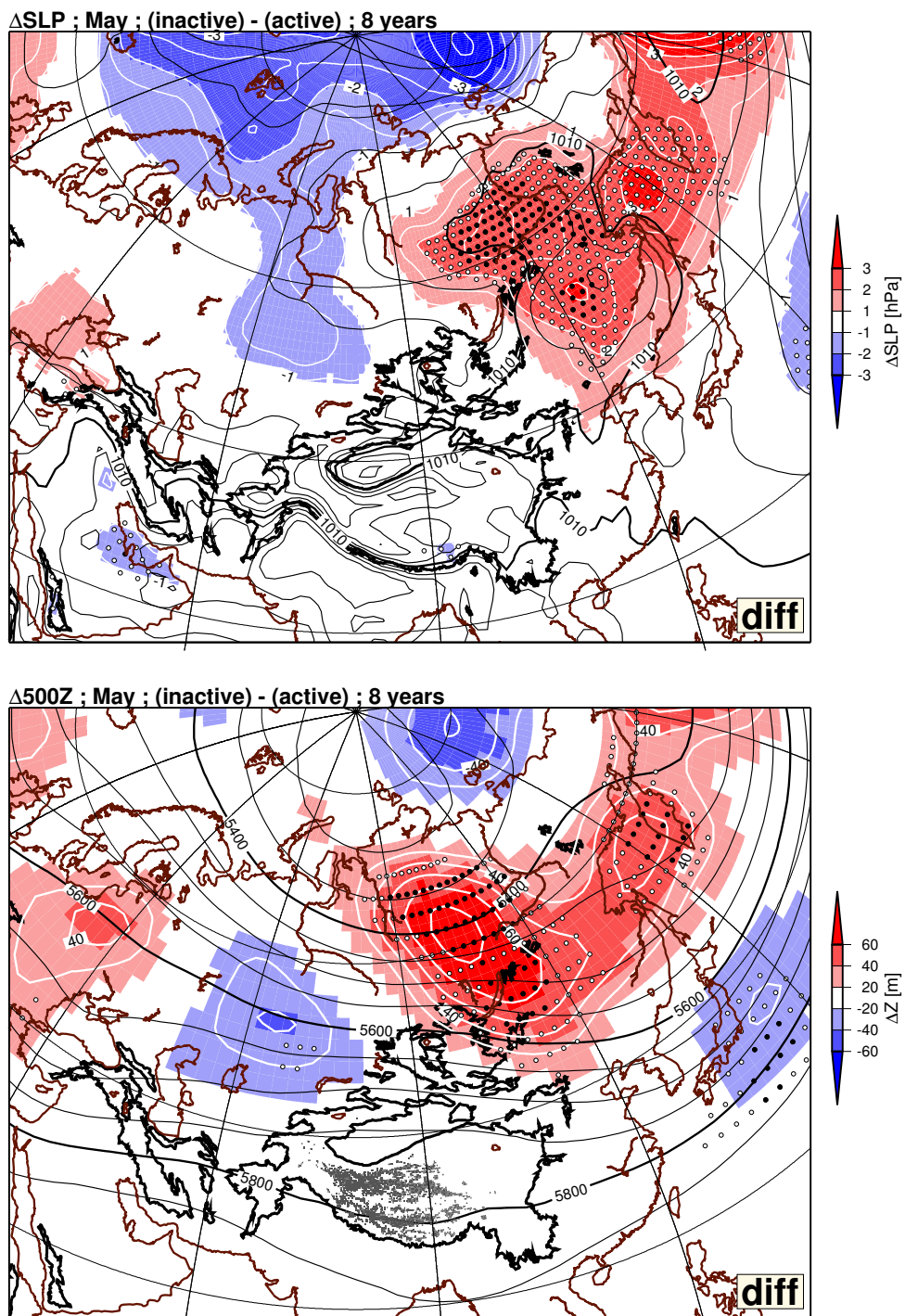


Fig. 5.4. Composite differences of meteorological fields between active and inactive years in May. (a) Δ SLP (1-hPa interval) and (b) Δ Z500 (10 m interval). Black contour represent climatological-mean field for the period 1972–2002. Statistically significant differences are denoted in white and black circles at 0.05 and 0.01 significance level, respectively.

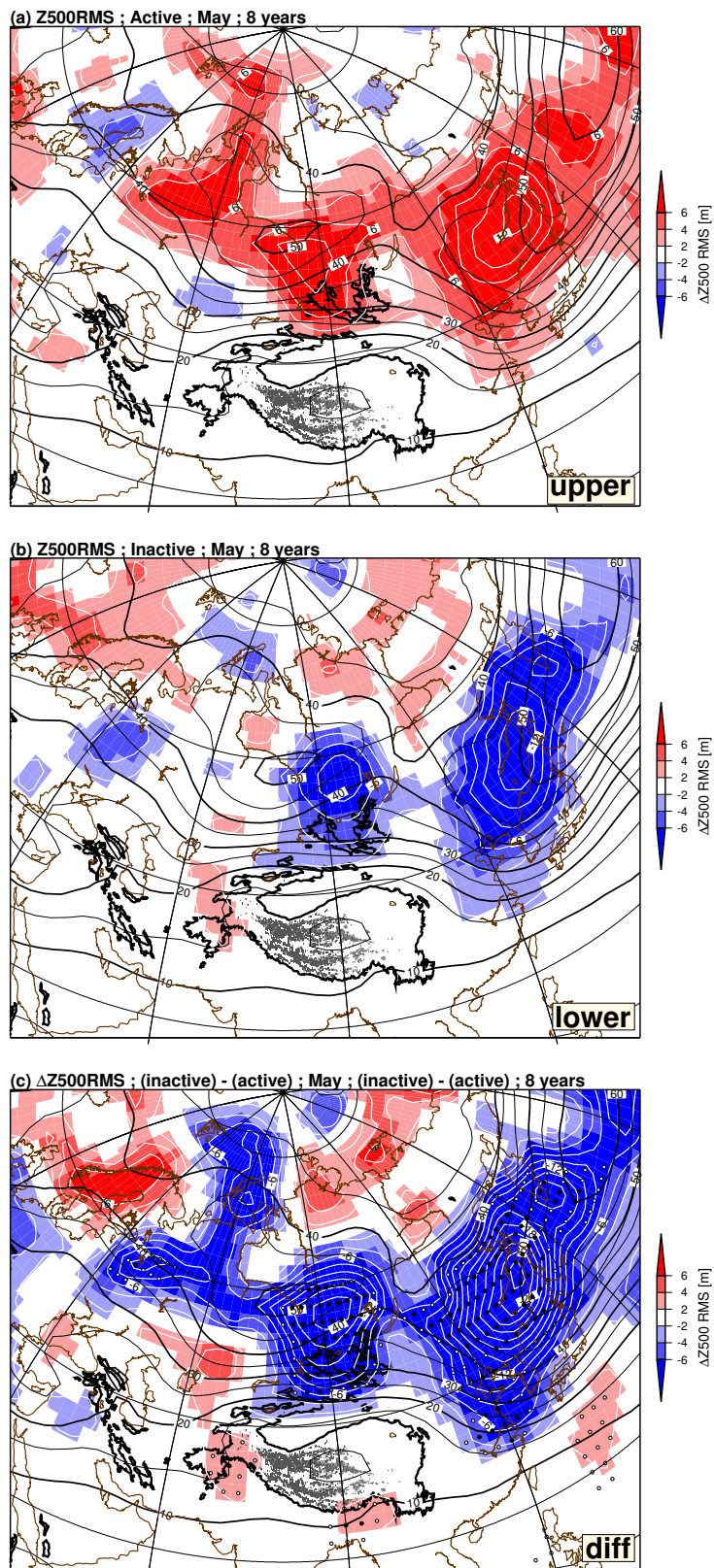


Fig. 5.5. Spatial distribution of synoptic eddy activities in May. (a) active, (b) inactive, and (c) differences between b and a (b minus a). Black contours represent climatological-mean values (5 m interval). Contour interval in anomaly and difference field is 1 m. Statistically significant differences are denoted in single and double circles at 0.05 and 0.01 significance level, respectively.

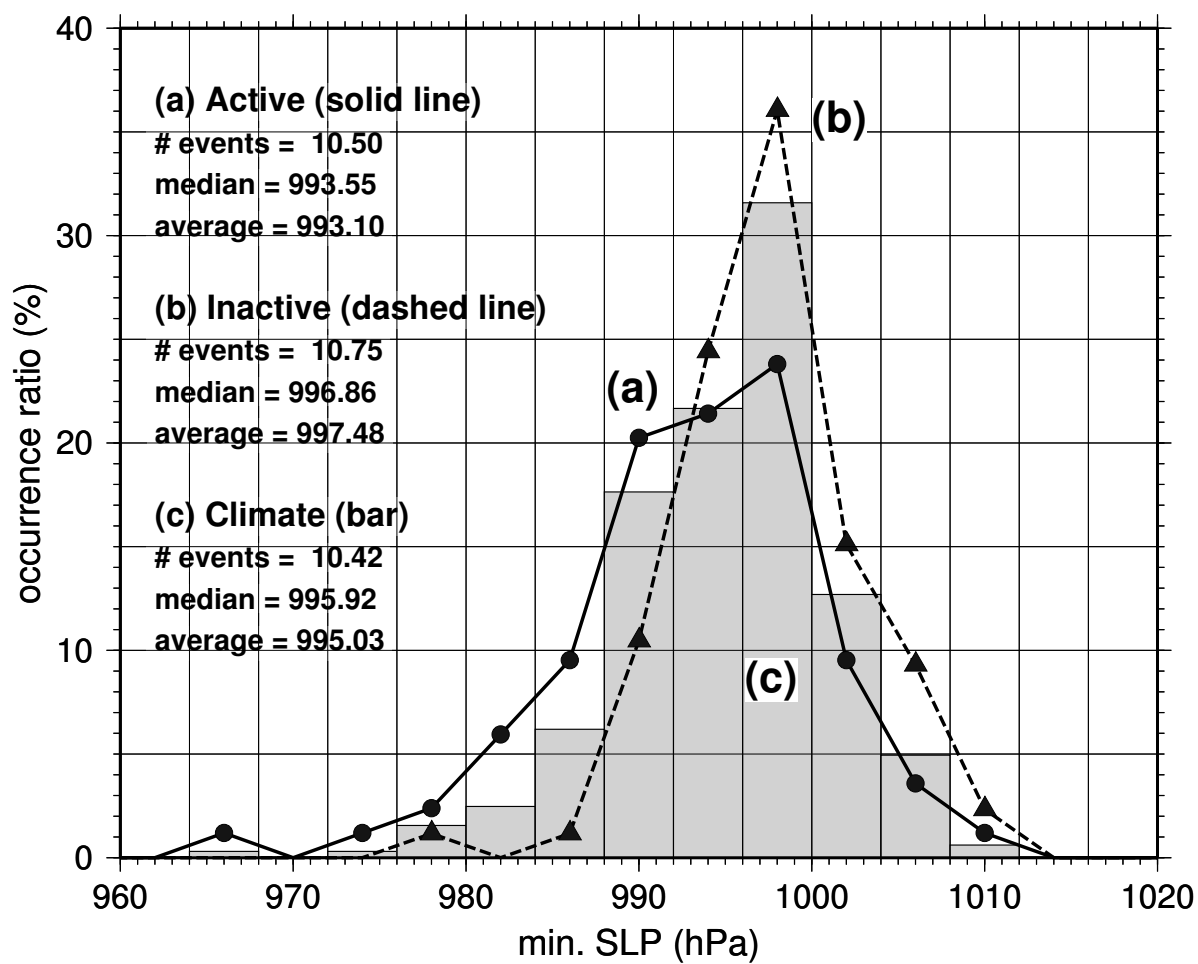


Fig. 5.6. Composite frequency of minimum SLP at cyclone center in Mongolia. Compositing years are same as Fig. 5.1.

Chapter 6

Discussion

6.1 Robustness of spatial distributions of cooling day frequency in eastern Mongolia

Composites of spatial distribution of cooling day frequency show several interesting characteristics (Figs. 4.4–4.6). For example, although spatial distribution of cooling day frequency shows various characteristics in each month, a location of the largest area of f_{cd} in East Asia can always be found within the analysis area. As shown in Section 3.1.1, the geographical location of f_{cd} in eastern Mongolia is probably influenced by topography in the upstream of eastern Mongolia. In other words, since the pathways of cold air are constrained by the surrounded topography, it seems that spatial position for the largest frequency of cooling day was located over similar area whether a cold frontal activity is active or inactive.

6.2 Considerations of physical processes in the weakening of cold frontal activity

6.2.1 Linkage between the reduction of cold frontal activity and the recent warming trend in Eurasia

Decreasing trend of cold frontal activity (CFA) in eastern Mongolia in spring will also help to consider a reason why the area of the strong warming trend of surface temperature is distributed from Siberia to China. As noted by Folland et al. (2001), the strong

warming trend in spring can be observed in the mid- and high-latitude continental interior originated from the West Siberian Plain to east China (Fig. 1.2b). Based on the results mentioned in previous studies, the recent warming trend in spring over northern Eurasia was usually interpreted by the following two reasons:

1. the increases of surface heating arising from the earlier snow disappearance of snow cover (e.g., Groisman et al. 1994a; Groisman et al. 1994b)
2. the increases of warm air advection from North Atlantic Ocean into continental Eurasia associated with the positive anomalies of westerly wind (e.g., Thompson and Wallace 1998; Thompson et al. 2000)

The first reason seems to be plausible explanation, however, it has a discrepancy in the spatial relationship between earlier snow-melt area and dominant area of largest warming trend. As illustrated in Fig. 1.2b, the region observed strong warming trend in spring is clearly identified in the West Siberian Plain and oriented southeastward to northern China. On the other hand, according to Bamzai (2003), the significant positive trend of snow free days is observed in 50° – 60° N from west of the Lake Baikal to northeastern China. Therefore, the spatial distribution of the recent warming trend, particularly in the south of 50° N, is not simply explained by an increased surface heating in the snow-free area.

The second reason, increased warm air advection associated with the intensified westerly wind, it also seems to be insufficient to produce the spatial distribution of the recent warming over Eurasia in spring. Positive temperature anomalies associated with the intensified westerly wind is largest in the northwestern Eurasia and generally oriented in a west–east direction in the high-latitudes (Thompson et al. 2000). Although the horizontal warm advection is probably suitable for explaining the spatial pattern of the warming trend in winter (see Fig. 1.2a), the strong warming region oriented in the northwest–southeast (NW–SE) direction in spring can not be interpreted enough. Thus, as same as

the effect of earlier snow melt, the warm air advection do not give a reasonable explanation in the spatial pattern of the recent warming trend over Eurasia in spring.

In contrast, the results mentioned in this study would provide an additional perspective for explaining the spatial pattern of the recent warming trend in spring. Comparing with Figs. 1.13 and 5.1, the area with positive temperature differences in May looks like a primary route of cold air outbreaks (Ding and Krishnamurti 1987; Zhang et al. 1997). Also, the overall pattern of positive temperature differences in Fig. 5.1 resembles the spatial distribution of the dominant warming trend in spring (Folland et al. 2001; see also Fig. 1.2b).

Based on the results in the previous chapter and discussions mentioned above, the linkage between the reduction of CFA in eastern Mongolia and spatial distribution of strong warming trend is explained by following processes: (1) warm temperature anomalies in the West Siberian Plain may be induced by intensified westerly wind, (2) earlier snow disappearance in eastern Eurasia also appear for the recent two decades, (3) because of the shrink of snow-covered areas, near-surface cold air in the high-latitudes tends to be weak, (4) since the air temperature in the cold-air source region has warm anomalies, the intensity of cold front (defined by a horizontal temperature difference across a cold front) becomes weak during a cold surge period.

6.2.2 Effect of the reduction of cold frontal activity in the downstream areas

As noted in Section 5.3, cyclone intensity and storm track activity is apparently reduced in the inactive years of CFA. The linkage between CFA and cyclonic eddy activity is probably explained as follows: (1) associated with the decreases of frontal intensity, baroclinicity across a cold front is weak, (2) cyclones generated in leeward of Altai-Sayan Mountains (Mongolian cyclones) have less intensity, (3) as a northeastward migration of the weakened cyclones, weakening of storm track activity extends from northeast China through the Sea of Okhotsk to northwestern Pacific.

Consequently, the weakening of cold front intensity may also produce a circulation change in the downstream areas through a synoptic eddy activity associated with a passage of cold frontal systems.

6.3 Application of the definition of cooling day

The cooling day defined in this study is used as an indicator for examining a cold frontal activity for the past climate. Furthermore, applicational use of this index provide useful information as follows.

One of the ways for application is used as an indicator for assessing performance of a general circulation models (GCMs). The statistics of cooling day can be obtained from a daily mean surface temperature based on the hindcast experiment of the twentieth century by using GCMs. If the mean statistics of cooling day estimated from the GCM output shows good agreement with the one estimated from observational data, the GCM is assumed to have good ability reproducing a day-to-day temperature variation.

The other ways for application is possibly used as an index of atmospheric potential of dust loading into the air, i.e., index of dust storm occurrences in East Asia. As discussed in Section 1.5 and 2.3.1, dust storms observed in Mongolia and northern China are frequently occurred in association with a traveling cold frontal systems. Since this study mainly focus on the interannual variation of cold frontal activity, it is not examined a qualitative/quantitative relationship between an activity of cold frontal systems and dust storm occurrences or its intensity. These are the focus of future research.

Chapter 7

Summary and conclusions

7.1 Assessment of cold frontal activity using “cooling day”

The interannual variability in the activity of cold frontal systems, which provides great influences to the socio-economic activity, was not examined enough in previous studies. Since definitions detecting frontal systems had generally determined by spatial discontinuity for thermodynamic variable at a standard pressure level (e.g., at the 850-hPa level), it was difficult to apply the definition in East Asia that includes much highly elevated areas (e.g., Tianshan Mountains, Altai–Sayan Mountains, Mongolian Plateau).

In this study, “cooling day”, which is defined as a day with decrease of daily mean surface air temperature exceeding a given threshold from the previous day, is proposed to detect a passage of a cold front. A passage of a cold front is investigated in East Asia by using cooling days obtained from the ERA-40 data for the period 1972–2002. The threshold is set 5 K in this study, which is referred from previous studies and empirically determined by synoptic experience. Strong cooling days are confirmed to correspond to a passage of cold front by sequential synoptic chart.

Geographical distributions of cooling day frequency show two dominant areas in every spring months. One area is found in eastern Mongolia and the Inner Mongolia in China, and is almost stationary in the geographical location throughout a year. The other area locate in the West Siberian Plain (March, April) or Kazakhstan (May). The spatial

pattern of the largest frequency area nearly corresponds to the primary track of cold air outbreaks (Ding and Krishnamurti 1987; Zhang et al. 1997). Therefore, although the definition of cooling day is very simple, the cooling day is a good indicator detecting a propagation of a cold frontal system. In addition, the biggest advantage for using this index is that a cold frontal activity can be examined in highly elevated areas.

7.2 Interannual variation of cold frontal activity in Mongolia

The interannual variations of cold frontal activity (CFA) in eastern Mongolia, which is obtained from area-integrated frequency of cooling days within an analysis area, show significant negative trend in spring for the recent two decades. There were no significant trends in any other seasons.

Comparisons of composited statistics of CFA between the active and inactive years show that the recent reduction of CFA is closely related to the weakening of a cooling intensity for each cooling event. The composite difference of cooling intensity at Day 0, which is defined by a day of the largest cooling for a cooling period, reach 60%–70% of the weakening of cooling intensity for the total cooling period. Based on the definition of the cooling intensity at Day 0, it is considered as a horizontal temperature difference across a cold front. As pointed out by Zhai et al. (1999), the occurrence frequency of strong cold surges has been decreasing in China. Therefore, it seems that the recent reduction of CFA in eastern Mongolia is closely related to the weakening of a cold front.

7.3 Relationships between reduction of cold frontal activity and meteorological conditions

The reduction of CFA in Mongolia is not influenced by the changes of tracks or temporal cycles for a passage of cold front but depended on the weakening of cooling intensity in each cooling event. The weakening of cooling intensity is significant in May. The tem-

perature difference between the active and inactive years indicates that positive (warm) temperature in the inactive years are dominant in the West Siberian Plain where a source region of cold air exists. The spatial distribution of the positive temperature difference is quite similar to the largest warming trend area. The composite analysis of snow cover extent in May shows that smaller extent of snow cover in the inactive years is found in eastern Eurasia. The negative anomaly of snow cover extent in the inactive years continues to mid-June. These results are consistent with the previous studies (Groisman et al. 1994b; Brown 2000; Bamzai 2003).

The leeside cyclones in eastern Mongolia and northeastern China, called as “Mongolian cyclone”, are frequently formed on the trailing cold fronts of occluded lows in western Siberia (Boyle and Chen 1987; see also Fig. 1.12). The activity of Mongolian cyclones shows largest frequency in spring (Chen et al. 1991). The composite analysis of cyclone activity indicates that the weakening of cyclone intensity is dominant for the inactive years of CFA in Mongolia. It is well known that a development rate of cyclones is proportional to a baroclinicity such as meridional temperature gradient (Holton 2004). Hence, the weakening of cold frontal intensity for the inactive years would also produce weak cyclones.

Although the results mentioned in this study give a new perspective considering the long-term change of the day-to-day weather conditions in association with climate change, there are a number of factors that have not been confirmed in this study. Investigation of atmosphere–snow interaction during a passage of cold front would provide a useful evidence to understand the physical processes of the changes of the cold frontal activity over East Asia in spring.

Acknowledgments

The author would like to express special thanks to Prof. Hiroshi Tanaka, Center for Computational Sciences, University of Tsukuba, for his valuable comments and encouragements. The discussion on the transient eddy activities with him was very helpful in improving the presentation of this study. His suggestions would also provide more reliable results in concern with detecting cold frontal systems. The author also thanks to Prof. Fujio Kimura and Yousei Hayashi, Graduate School of Life and Environment Sciences, University of Tsukuba, whose comments greatly improved this manuscript. Thanks also go to Prof. Ken'ichi Ueno and Hiroaki Ueda, Graduate School of Life and Environment Sciences, University of Tsukuba. Their studies and comments were valuable for this study.

The author would like to acknowledge Dr. Seiji Sugata, the Urban Air Quality Research Team, PM2.5/DEP Research Project, National Institute for Environmental Studies, Japan, for his kind supports, valuable discussions and encouragements. Special thanks go to Dr. Shinji Wakamatsu and Toshimasa Ohara, the Urban Air Quality Research Team, PM2.5/DEP Research Project, National Institute for Environmental Studies, Japan, for their helpful comments and advice. The author's thanks also go to all members of the Urban Air Quality Research Team, PM2.5/DEP Research Project, National Institute for Environmental Studies, Japan. The author thanks all members of Atmospheric Environmental Division, National Institute for Environmental Studies, Japan.

The author would like to acknowledge Prof. Itsushi Uno, Research Institute for Applied Mechanics, Kyushu University, for his helpful comments and advice. His studies and comments were valuable for this study.

The author wishes to thank all staff and student members of Climatology and Meteorology Laboratory, University of Tsukuba, for providing helpful comments.

The author would like to acknowledge Dr. Yasunori Kurosaki, Center for Environmental Remote Sensing (CEReS), Chiba University, for a lot of comments and advice. His studies and comments were valuable for this study.

This study is dedicated to my family, especially my wife, Kazumi, and my parents, Shoji and Mineko.

All the figures in this paper were created with the Generic Mapping Tools (GMT) (Wessel and Smith 1998).

REFERENCES

- Bamzai, A. S., 2003: Relationship between snow cover variability and Arctic Oscillation index on a hierarchy of time scales. *Int. J. Climatol.*, **23**, 131–142.
- Blackmon, M. L., 1976: A climatological spectral study of the 500mb geopotential height of the Northern Hemisphere. *J. Atmos. Sci.*, **33**, 1607–1623.
- Bluestein, H. B., 1993: *Synoptic-Dynamic Meteorology in Midlatitudes*. Vol. II Observations and Theory of Weather Systems, Oxford University Press, New York, 594pp.
- Boyle, J. S. and T.-J. Chen, 1987: Synoptic aspects of the wintertime east Asian monsoon. *Monsoon Meteorology*, Oxford Univ. Press, New York, 125–160.
- Brown, R. D., 2000: Northern Hemisphere snow cover variability and change, 1915–97. *J. Climate*, **13**, 2339–2355.
- Chen, S.-J., Y.-H. Kuo, P.-Z. Zhang and Q.-F. Bai, 1991: Synoptic climatology of cyclogenesis over East Asia, 1958 – 1987. *Mon. Wea. Rev.*, **119**, 1407–1418.
- Chen, T.-C., W.-R. Huang and J.-H. Yoon, 2004: Interannual variation of the East Asian cold surge activity. *J. Climate*, **17**, 401–413.
- Chung, Y.-S., H.-S. Kim, J. Dulam and J. Harris, 2003: On heavy dustfall observed with explosive sandstorms in Chongwon-Chongju, Korea in 2002. *Atmos. Environ.*, **37**, 3425–3433.
- Clark, M. P. and M. C. Serreze, 2000: Effects of variations in east Asian snow cover on modulating atmospheric circulation over the north Pacific. *J. Climate*, **13**, 3700–3710.
- Clark, M. P., M. C. Serreze and D. A. Robinson, 1999: Atmospheric controls on Eurasian snow extent. *Int. J. Climatol.*, **19**, 27–40.
- Compo, G. P., G. N. Kiladis and P. J. Webster, 1999: The horizontal and vertical structure of east Asian winter monsoon pressure surges. *Quart. J. Roy. Meteor. Soc.*, **125**, 29–54.
- Conaty, A. L., J. C. Jusem, L. Takacs, D. Keyser and R. Atlas, 2001: The structure and evolution of extratropical cyclones, fronts, jet streams, and the tropopause in the GEOS general circulation model. *Bull. Amer. Meteor. Soc.*, **82**, 1853–1867.
- Curry, J., 1983: On the formation of continental polar air. *J. Atmos. Sci.*, **40**, 2278–2292.
- Curry, J., 1987: The contribution of radiative cooling to the formation of cold-core anticyclone. *J. Atmos. Sci.*, **44**, 2575–2592.

- Ding, Y., 1994: *Monsoons over China*. Kluwer Academic Publishers, Dordrecht, Netherlands, 432pp.
- Ding, Y. and T. N. Krishnamurti, 1987: Heat budget of the Siberian high and the winter monsoon. *Mon. Wea. Rev.*, **115**, 2428–2449.
- Enomoto, H., S. Takahashi, S. Kobayashi, K. Goto-Azuma and O. Watanabe, 1993: Large temperature variations in winter around Svalbard. *Bulletin of Glacier Research*, **11**, 17–22.
- Folland, C. K., C. Miller, D. Bader, M. Crowe, P. D. Jones, N. Plummer, M. Richman, D. E. Parker, J. Rogers and P. Scholefield, 1999: Breakout group C; Temperature Indices for Climate Extremes. *Clim. Change*, **42**, 31–43, Workshop on Indices and Indicators for Climate Extremes, Asheville, NC, USA, 3-6 June 1997.
- Folland, C. K., T. R. Karl, J. R. Christy, R. A. Clarke, G. V. Gruza, J. Jouzel, M. E. Mann, J. Oerlemans, M. J. Salinger and S.-W. Wang, 2001: Observed climate variability and change. *Climate Change 2001: The Scientific Basis. Contribution of Working Group I to the Third Assessment Report of the Intergovernmental Panel on Climate Change*, Cambridge Univ. Press, 99–181.
- Fukutomi, Y., K. Masuda and T. Yasunari, 2004: Role of storm track activity in the interannual seesaw of summer precipitation over northern Eurasia. *J. Geophys. Res.*, **109**, D02109, doi: 10.1029/2003JD003912.
- Groisman, P. Y., T. R. Karl and R. W. Knight, 1994a: Observed impact of snow cover on the heat balance and the rise of continental spring temperatures. *Science*, **263**, 198–200.
- Groisman, P. Y., T. R. Karl, R. W. Knight and G. L. Stenchikov, 1994b: Changes of snow cover, temperature, and radiative heat balance over the Northern Hemisphere. *J. Climate*, **7**, 1633–1656.
- Hayasaki, M. and H. L. Tanaka, 1999: A study of drastic warming in the troposphere: A case for the winter of 1989 in Alaska. *Tenki*, **46**, 123–135 (in Japanese).
- Hayasaki, M. and H. L. Tanaka, 2004: Climatological study of abrupt surface air temperature changes in the Northern Hemisphere. *Geographical Review of Japan*, **77**, 609–627 (in Japanese).
- Holton, J. R., 2004: *An Introduction to Dynamic Meteorology 4th edition*. Academic Press, 550pp.
- Hoskins, B. J. and P. J. Valdes, 1990: On the existence of storm-tracks. *J. Atmos. Sci.*, **47**, 1854–1864.
- Houghton, J. T., Y. Ding, D. J. Griggs, M. Noguer, P. van der Linden, X. Dai, K. Maskell and C. A. Johnson, Eds., 2001: *Climate Change 2001: The Scientific Basis*. Cambridge Univ. Press, 881pp.
- Hurrell, J. W., 1996: Influence of variations in extratropical wintertime teleconnections on Northern Hemisphere temperature. *Geophys. Res. Lett.*, **23**, 665–668.

- Husar, R. B., D. M. Tratt, B. A. Schichtel, S. R. Falke, F. Li, D. Jaffe, S. Gassó, T. Gill, N. S. Laulainen, F. Lu, M. C. Reheis, Y. Chun, D. Westphael, B. N. Holben, C. Gueymard, I. McKendry, N. Kuring, G. C. Feldman, C. McClain, R. J. Frouin, J. Merrill, D. DuBois, F. Vignola, T. Murayama, S. Nickovic, W. E. Wilson, K. Sassen, N. Sugimoto and W. C. Malm, 2001: Asian dust events of April 1998. *J. Geophys. Res.*, **106**, 18317–18330.
- In, H.-J. and S.-U. Park, 2003: The soil particle size dependent emission parameterization for an Asian dust (Yellow Sand) observed in Korea in April 2002. *Atmos. Environ.*, **37**, 4625–4636.
- Jones, P. D., T. J. Olson, K. R. Briffa, C. K. Folland, E. B. Horton, L. V. Alexander, D. E. Parker and N. A. Rayner, 2001: Adjusting for sampling density in grid box land and ocean surface temperature time series. *J. Geophys. Res.*, **106**, 3371–3380.
- Joung, C. H. and M. H. Hitchman, 1982: On the role of successive downstream development in East Asian polar air outbreaks. *Mon. Wea. Rev.*, **110**, 1224–1237.
- Karl, T. R. and D. R. Easterling, 1999: Climate extremes: Selected review and future research directions. *Clim. Change*, **42**, 309–325.
- Karl, T. R., P. D. Jones, R. W. Knight, G. Kukla, N. Plummer, V. Razuvayev, K. P. Gallo, J. Lindseay, R. Charlson and T. C. Peterson, 1993: A new perspective on recent global warming: Asymmetric trends of daily maximum and minimum temperature. *Bull. Amer. Meteor. Soc.*, **74**, 1007–1023.
- Karl, T. R., R. W. Knight and N. Plummer, 1995: Trends in high-frequency climate variability in the twentieth century. *Nature*, **377**, 217–220.
- Kimoto, M., 2005: Simulated change of the east Asian circulation under global warming scenario. *Geophys. Res. Lett.*, **32**, L16701, doi: 10.1029/2005GL023383.
- Kurosaki, Y. and M. Mikami, 2003: Recent frequent dust events and their relation to surface wind in East Asia. *Geophys. Res. Lett.*, **30**, 1736, doi:10.1029/2003GL017261.
- Lau, N.-C., 1988: Variability of the observed midlatitude storm tracks in relation to low-frequency changes in the circulation pattern. *J. Atmos. Sci.*, **45**, 2718–2743.
- Lau, N.-C. and K.-M. Lau, 1984: The structure and energetics of midlatitude disturbances accompanying cold-air outbreaks over East Asia. *Mon. Wea. Rev.*, **112**, 1309–1327.
- Limpasuvan, V. and D. L. Hartmann, 1999: Eddies and the annular modes of climate variability. *Geophys. Res. Lett.*, **26**, 3133–3136.
- Limpasuvan, V. and D. L. Hartmann, 2000: Wave-maintained annular modes of climate variability. *J. Climate*, **13**, 4414–4429.
- Mullen, S. L., 1987: Transient eddy forcing of blocking flows. *J. Atmos. Sci.*, **44**, 3–22.
- Nakamura, H., 1992: Midwinter suppression of baroclinic wave activity in the Pacific. *J. Atmos. Sci.*, **49**, 1629–1642.
- Nakamura, H. and T. Sampe, 2002: Trapping of synoptic-scale disturbances into the North-Pacific subtropical jet core in midwinter. *Geophys. Res. Lett.*, **29**, 1761, 10.1029/2002GL015535.

- Park, S.-U. and H.-J. In, 2003: Parameterization of dust emission for the simulation of the yellow sand (Asian dust) event observed in March 2002 in Korea. *J. Geophys. Res.*, **108**, 4618, doi: 10.1029/2003JD003484.
- Qian, W., L. Quan and S. Shi, 2002: Variations of the dust storm in China and its climatic control. *J. Climate*, **15**, 1216–1229.
- Rayner, N. A., D. E. Parker, E. B. Horton, C. K. Folland, L. V. Alexander, D. P. Rowell, E. C. Kent and A. Kaplan, 2003: Global analyses of sea surface temperature, sea ice, and night marine air temperature since the late nineteenth century. *J. Geophys. Res.*, **108**, 4407, doi: 10.1029/2002JD002670.
- Reynolds, R. W., N. A. Rayner, T. M. Smith, D. C. Stokes and W. Wang, 2002: An improved in situ and satellite SST analysis for climate. *J. Climate*, **15**, 1609–1625.
- Rogers, J. C., 1997: North Atlantic storm track variability and its association to the North Atlantic Oscillation and climate variability of northern Europe. *J. Climate*, **10**, 1635–1647.
- Rogers, J. C. and E. M. Thompson, 1995: Atlantic Arctic cyclones and the mild Siberian winters of the 1980s. *Geophys. Res. Lett.*, **22**, 799–802.
- Serreze, M. C., 1995: Climatological aspects of cyclone development and decay in the Arctic. *Atmos.-Ocean*, **33**, 1–23.
- Serreze, M. C., J. D. Kahl and R. C. Schnell, 1992: Low-level temperature inversions of the Eurasian Arctic and comparisons with Soviet drifting station data. *J. Climate*, **5**, 615–629.
- Serreze, M. C., F. Carse, R. G. Barry and J. C. Roggers, 1997: Icelandic low cyclone activity: Climatological features, linkages with the NAO, and relationships with recent changes in the Northern Hemisphere circulation. *J. Climate*, **10**, 453–464.
- Serreze, M. C., A. H. Lynch and M. P. Clark, 2001: The Arctic frontal zone as seen in the NCEP–NCAR reanalysis. *J. Climate*, **14**, 1550–1567.
- Shao, Y. and J. Wang, 2003: A climatology of Northeast Asian dust events. *Meteorol. Zeits.*, **12**, 187–196.
- Shinoda, M., H. Utsugi and W. Morishima, 2001: Spring snow-disappearance timing and its possible influence on temperature fields over central Eurasia. *J. Meteor. Soc. Japan*, **79**, 37–59.
- Simmons, A. J., P. D. Jones, V. da Costa Bechtold, A. C. M. Beljaars, P. W. Kållberg, S. Saari-
nen, S. M. Uppala, P. Viterbo and N. Wedi, 2004: Comparison of trends and low-frequency
variability in CRU, ERA-40, and NCEP/NCAR analyses of surface air temperature. *J.
Geophys. Res.*, **109**, D24115, 10.1029/2004JD005306.
- Sugimoto, N., I. Uno, M. Nishikawa, A. Shimizu, I. Matsui, X. Dong, Y. Chen and H. Quan,
2003: Record heavy Asian dust in Beijing in 2002: Observations and model analysis of
recent events. *Geophys. Res. Lett.*, **30**, 1640, 10.1029/2002GL016349.
- Sun, J., T. Liu and Z. Lei, 2000: Sources of heavy dust fall in Beijing, China on April 16, 1998.
Geophys. Res. Lett., **27**, 2105–2108.

- Sun, J., M. Zhang and T. Liu, 2001: Spatial and temporal characteristics of dust storms in China and its surrounding regions, 1960 – 1999: Relations to source area and climate. *J. Geophys. Res.*, **106**, 10325–10333.
- Sun, L., X. Zhou, J. Lu, Y.-P. Kim and Y.-S. Chung, 2003: Climatology, trend analysis and prediction of sandstorms and their associated dustfall in China. *Water, Air, and Soil Pollution: Focus*, **3**, 41–50.
- Thompson, D. W. J. and J. M. Wallace, 1998: The Arctic Oscillation signature in the wintertime geopotential height and temperature fields. *Geophys. Res. Lett.*, **25**, 1297–1300.
- Thompson, D. W. J., J. M. Wallace and G. C. Hegerl, 2000: Annular modes in the extratropical circulation. part II: Trends. *J. Climate*, **13**, 1018–1036.
- Tsumura, T. and K. Yamazaki, 2005: A case study on a Shapiro-type extratropical cyclone developed around Japan from a viewpoint of frontogenesis. *Tenki*, **52**, 105–118 (in Japanese).
- Ueda, H., M. Shinoda and H. Kamahori, 2003: Spring northward retreat of Eurasian snow cover relevant to seasonal and interannual variations of atmospheric circulation. *Int. J. Climatol.*, **23**, 615–629.
- Wallace, J. M. and D. S. Gutzler, 1981: Teleconnections in the geopotential height field during the Northern Hemisphere winter. *Mon. Wea. Rev.*, **109**, 784–812.
- Wallace, J. M., G.-H. Lim and M. L. Blackmon, 1988: Relationship between cyclone tracks, anticyclone tracks and baroclinic waveguides. *J. Atmos. Sci.*, **45**, 439–462.
- Wallace, J. M., Y. Zhang and K.-H. Lau, 1993: Structure and seasonality of interannual and interdecadal variability of the geopotential height and temperature fields in the Northern Hemisphere troposphere. *J. Climate*, **6**, 2063–2082.
- Wessel, P. and W. H. F. Smith, 1998: New, improved version of Generic Mapping Tools released. *EOS Trans. Amer. Geophys. Union*, **79**, 579.
- Whittaker, L. M. and L. H. Horn, 1984: Northern Hemisphere extratropical cyclone activity for four mid-season months. *J. Climatology*, **4**, 297–310.
- Zhai, P., A. Sun, F. Ren, X. Liu, B. Gao and Q. Zhang, 1999: Changes of climate extremes in China. *Clim. Change*, **42**, 203–218.
- Zhang, Y., K. R. Sperber and J. S. Boyle, 1997: Climatology and interdecadal variation of the East Asian winter monsoon: Results from the 1979-95 NCEP/NCAR reanalysis. *Mon. Wea. Rev.*, **125**, 2605–2619.
- Zhang, X. Y., S. L. Gong, T. L. Zhao, R. Arimoto, Y. Q. Wang and Z. J. Zhou, 2003: Sources of Asian dust and role of climate change versus desertification in Asian dust emission. *Geophys. Res. Lett.*, **30**, 2272, doi: 10.1029/2003GL018206.